

Fluid-structure interaction of composite propeller blades involving large deformations

Dissertation

Zur

Erlangung des akademischen Grades

Doktor-Ingenieur (Dr.-Ing.)

der Fakultät für Maschinenbau und Schiffstechnik

der Universität Rostock

Rostock, 2016

Submitted by: Jitendra Kumar

Date of Birth: 10th March 1986

Birth Place: Ranchi, India

Gutachter:

1. Prof. Dr.-Ing. Frank-Hendrik Wurm
Lehrstuhl Strömungsmaschinen, Universität Rostock
2. Prof. em. Dr.-Ing. habil. Alfred Leder
Lehrstuhl Strömungsmechanik, Universität Rostock

Datum der Einreichung: 03.02.2016

Datum der Verteidigung: 20.07.2016

Acknowledgment

It is my great pleasure to present the doctoral thesis on “**Fluid-structure interaction of composite propeller blades involving large deformations**”. I would like to acknowledge a number of people for their support during the research work for this thesis.

With great pleasure, I express my deep sense of gratitude to Professor Dr.-Ing. Frank-Hendrik Wurm for offering me this challenging research topic and the opportunity to write the thesis under his supervision. Prof. Wurm gave me logical suggestions and constructive criticisms time to time in friendly manner. His comments added great strength to this dissertation.

I am extremely thankful to Mr. Hendrik Sura and company WILO SE. They provided me all required CAD data, blade material information for a comprehensive numerical modelling and simulation of the mixer blade. Additionally, they provided related experimental data for the validation of numerical simulations.

My special thanks belongs to Danilo Webersinke. His accurate and critical review of my work kept me on right track. I would like to thank Dr. Günther Steffen for sharing knowledge about high quality block meshing and CFD simulation setups. Without his initial support, it was hard to reach the objectives of the project. Also, I want to acknowledge Dr. Witte, Dr. Benz, Mr. Lass, Mr. Hallier, Mr. Juckelandt and all other colleagues at Institute of Turbomachines. They provided comfortable and friendly environment to present my thoughts and work. Many thanks to Mrs. Bettina Merian-Sieblist for her enthusiastic help in non-scientific matters.

Finally, I am especially grateful to my wife Sunita Kumari and my family for their love, encouragement and incredible support. They taught me to balance work and personal life together.

Rostock, February 2016

Jitendra Kumar

Abstract

Flowing fluid over or inside of the structures exerts pressure loads which cause structures to deform. The large flow-induced deformation inherits new boundary for the flow domain. An efficient numerical modelling technique is required to enumerate flow-induced deformation and its consequence. Propeller blades experience significant flow-induced deformation, so coupled simulations of fluid and structure are needed for design optimization and failure prognostics. Moreover, composite propeller blades need more focus as they experience even larger deformations in real applications. A comprehensive modelling of the mixer propeller and tidal-turbine blades are discussed within this research work. An extensive computational fluid dynamics (CFD), finite element modelling (FEM), failure prognostic modelling and fluid-structure interaction (FSI) simulations of layered composite blade are performed.

Numerous CFD simulations are performed by using different turbulence model to find correct numerical setup and results are compared to experimental data. The thrust and torque data obtained from the numerical simulations using SST turbulence model with Gamma-Theta transition model, have least deviation from the experimentally obtained thrust and torque values. Thus, only SST turbulence model with Gamma-Theta transition model is selected for the FSI simulations. Moreover, the selected numerical model is able to find the flow transition from laminar to turbulent on the suction side of the blade. Plenty of simulations are performed to create thrust and torque curves versus inlet velocities. The flow behind the blades (mixer propeller and tidal-turbine) are analyzed in detail to visualize the hub delay and, the velocity profiles over axial and radial distance.

The mixer propeller and tidal-turbine blades are made of layered glass-fiber reinforced composites and random-oriented carbon-fiber reinforced composites respectively. A microscopic study is performed using a high resolution microscope to obtain the thickness and the fiber orientation for each single layer of the composite. For FEM analysis, each layer of the laminate is modelled as a solid hex-element with the anisotropic material properties. The material data is verified by a Vic-3D experimental

technique. A process to create and validate material data for the layered composite blade is compiled in the current thesis.

For the fluid-structure interaction analysis, initially uni-directional FSI is performed and it is observed that the blade experiences large deformation because of the heavy thrust. Thus, bi-directional FSI becomes important because fluid forces deforming the geometry of the structural domain significantly. Moreover, bi-directional FSI simulations are important to calculate the final thrust, torque and deformation of the blade accurately. The large deformation in the domain causes a numerical convergence problem during simulations, which is solved by mesh smoothing, re-meshing and a time discrete iterative solver algorithm using commercial ANSYS-CFD and ANSYS-APDL code. A detailed modelling technique and control parameters are shown to achieve bi-directional FSI for the large deformations.

A comparative study is presented between uni-directional and bi-directional FSI simulations. The differences in pressure distributions, stress distributions, thrusts and torques of the blade for both type of the FSI simulations are displayed. Moreover, for the failure prognostic, in house code for Tsai-Wu, Puck and LaRC criteria are written and these criteria are implemented for the failure prognostics in ANSYS-APDL using customization tool. Furthermore, these criteria are validated using tensile and bending destructive tests of the composite probes. It is observed that the LaRC failure criteria are better than other two criteria for failure prognostic.

In the last section of the thesis, a novel application of FSI simulation technique involving large deformations and anisotropic property of composite materials are presented briefly. They are used together as a tool to design a composite connector between the blade and hub. This connector undergo twist and changes the pitch of the blade based on pressure distribution onto the blade surface. As a result, thrust at high inlet velocity is reduced up to 12 percent, which further causes reduction in the blade deformation. This phenomena goes on till a convergence is not reached for the deformation. By this innovative composite connector, the chances of early permanent failure during high inflow conditions can be delayed.

Nomenclature

Roman Symbols

<u>Symbol</u>	<u>Unit</u>	<u>Description</u>
\vec{v}	[m/s]	Velocity vector
t	[s]	Time
$u_i(t)$	[m/s]	Instantaneous velocity
u, v, w	[m/s]	Velocity components in Cartesian co-ordinate system
u_x, u_r, u_ϕ	[m/s]	Velocity components in Cylindrical co-ordinate system
p	[N/m ²],[Pa]	Pressure
F_b	[N]	Body force
M	[Kg]	Mass of the body
C	[Ns/m]	Damping coefficient of the body
K	[N/m]	Stiffness coefficient of the body
u_s	[m]	Structural displacement
Y_\perp	[N/m ²],[Pa]	Young's modulus in transverse direction
Y_\parallel	[N/m ²],[Pa]	Young's modulus in longitudinal direction
$S_{\perp\perp}$	[N/m ²],[Pa]	Shear modulus on transverse plane
$S_{\perp\parallel}$	[N/m ²],[Pa]	Shear modulus on longitudinal-transverse plane

N_b	[-]	Number of blades
Tu	[-]	Turbulent intensity
r	[m]	Radius of blade rotor
D	[m]	Diameter of blade rotor
y^+	[-]	Dimensionless wall distance
Re	[-]	Reynolds number
$Re_{\theta t}$	[-]	Transition momentum thickness Reynolds number
P_k	[m ² /s]	Turbulent production rate
D_k	[m ² /s]	Turbulent destruction rate
f_i	[N/m ²],[Pa]	Ultimate material strength in i direction
C_{PR}	[-]	Coefficient of Power
C_{MR}	[-]	Coefficient of Moment
F_x, F_y, F_z	[N]	Fluid forces on the blade in x, y and z directions
G_I	[m ² /s ³]	Energy release rates for mode I loading

Greek Symbols

<u>Symbol</u>	<u>Unit</u>	<u>Description</u>
Ω_s	[-]	Solid domain
Ω_f	[-]	Fluid domain

ρ	[Kg/m ³]	Density of fluid
$\tau_{\perp\parallel}$	[N/m ²]	Shear stress in transverse-longitudinal plane
$\tau_{\perp\perp}$	[N/m ²]	Shear stress in transverse-transverse plane
μ	[Pa*s]	Normal viscosity
μ_t	[Pa*s]	Turbulent viscosity
ε	[m ² /s ³]	Turbulent energy dissipation rate
ω	[1/s]	Turbulent frequency
k	[m ² /s ²]	Turbulent kinetic energy
σ_n	[N/m ²]	Normal stress on fracture plane
σ_m	[N/m ²]	Normal stress on misalignment plane
σ_{\parallel}	[N/m ²]	Normal stress in longitudinal direction
σ_{\perp}	[N/m ²]	Normal stress in transverse direction
γ	[-]	Intermittency
α	[°]	Flow divergence angle
φ	[°]	Misalignment angle
ψ	[°]	Kink plane angle
π	[-]	Constant; $\pi = 3.14159$
λ	[-]	Tip-speed ratio
ω_o	[rad/s]	Rotational speed

δ_n	[m]	Normal debonding gap
η	[-]	Artificial damping coefficient
θ_{fp}	[°]	Fracture plane

Abbreviations

ALE	Arbitrary Lagrangian Eulerian
APDL	ANSYS Parametric Design Language
BEM	Blade Element Method
CAD	Computer Aided Design
CFD	Computational Fluid Dynamics
CFRP	Carbon Fiber Reinforced Plastic
DCZM	Discrete Cohesive Zone Model
DES	Detached Eddy Simulation
DNS	Direct Numerical Simulation
FEM	Finite Element Method
FF	Fiber Failure
FSI	Fluid-Structure Interaction
GFRP	Glass Fiber Reinforced Plastic
IFF	Inter-Fiber Failure

LDV	Laser Doppler Velocimetry
LES	Large Eddy Simulation
LaRC	Langley Research Center
NURBS	Non-Uniform Rational B-Spline
OpenFOAM	Opensource Field Operation and Manipulation
PDE	Partial Differential Equation
RANS	Reynolds-Averaged-Navier-Stokes
RPM	Rotation per Minute
RMS	Root Mean Square
SST	Shear Stress Transport
UDC	Uni-Directional Composite
URANS	Unsteady Reynolds-Averaged-Navier-Stokes
VLM	Vortex Lattice Method

Contents

Acknowledgement	I
Abstract	II
Nomenclature	IV
Contents	IX
1 Introduction	1
1.1 Motivation.....	1
1.1.1 Submersible mixer propeller	4
1.1.2 Tidal-turbine	5
2 State of the Art	6
2.1 Mixer propeller and tidal-turbine simulations	6
2.2 Modelling of composites material and failure prognostic	7
2.3 Handling of fluid-structure interaction problems	9
2.4 Objective.....	11
3 Mathematical modelling	13
3.1 Computational fluid dynamics	13
3.1.1 Governing equations.....	13
3.1.2 Reynolds-averaged Navier-Stokes equations (RANS).....	14
3.1.3 Turbulence models: Two equation models	15
3.2 Finite element analysis.....	18
3.2.1 Governing equations.....	18
3.2.2 Element type.....	19
3.2.3 Glue modelling	19

3.3	Failure prognostic modelling of composite	21
3.3.1	Main failure modes in fiber reinforced laminated composites.....	21
3.3.2	Theories for failure prognostics	22
3.4	Multi-physics solver coupling.....	30
3.4.1	Governing equations.....	31
3.4.2	Mapping.....	31
3.4.3	Smoothing	32
3.4.4	Re-meshing.....	32
4	Flow simulation	34
4.1	Domain and grid modelling	34
4.2	Boundary conditions	37
4.3	Simulation results.....	39
4.3.1	Turbulence model: Comparison and selection	39
4.3.2	Torque and thrust characteristics.....	42
4.3.3	Velocity profile: Jet turbulent flow	45
4.3.4	Flow, thrust and power characteristic of the tidal-turbine.....	47
5	Structural simulation	51
5.1	Microscopic study of the blade	51
5.2	Grid modelling	52
5.3	Glue modelling.....	53
5.4	Material modelling for mixer blade	53
5.5	Experimental validation of material model.....	55
5.6	Fracture code modelling	57
5.6.1	Probes: Microscopic study	57

5.6.2	Probes: Grid modelling	58
5.6.3	Probes: Experimental study	59
5.6.4	Probes: Material modelling and simulation.....	59
5.6.5	Probes: Simulation results	61
5.7	Material model for the tidal-turbine blade	64
6	Fluid-structure interaction	65
6.1	Uni-directional fluid-structure interaction	65
6.1.1	Mapping.....	65
6.1.2	Simulation results	67
6.2	Bi-directional fluid-structure interaction	69
6.2.1	Mapping.....	69
6.2.2	Mesh deformation and Re-meshing	70
6.3	Comparison between Uni-directional and Bi-directional FSI.....	70
6.4	Fracture analysis	74
7	Application of FSI: Blade pitch control	77
8	Conclusion	83
9	Outlook	86
	Bibliography	88
	Appendices	97
	Declaration in lieu of oath	111

1 Introduction

A comprehensive modelling, coupled simulation and simultaneous solutions of various physical domains for numerous applications have become essential in computational mechanics for optimization with the significant increase of the computer power. Flowing fluid over or inside of the structures exerts pressure load which causes structures to deform. The flow-induced deformations inherit new boundaries for the flow domain. The exchange of energy between a moving fluid and a flexible structure is generalized as fluid-structure interaction (FSI).

It is an important branch of multi-physics problems. FSI simulations for coupled interaction of fluid and structure are important to capture and interpret various phenomena for different engineering applications such as marine application, helicopter blade design application, submersible mixer and pump applications.

1.1 Motivation

In various industrial applications, challenges to enumerate flow-induced deformation and its consequences are being faced, for example propeller manufacturing industries. The propeller are used to push the liquid and it experiences heavy thrust backward. Traditionally, propellers are made of metal for their higher strength and reliability to push the fluids. On the other hand, metallic propellers undergo cavitation erosion [1], corrosion damage and fatigue-induced cracking [2]. Moreover, a relatively poor acoustic damping properties of the metallic propellers lead to noise due to structural vibration [3]. To overcome the problems of metallic propellers, composite materials are getting more and more attention of industries as an alternative material. The composite materials have a higher strength to weight ratio. Weight reduction of composite blades is about 50 to 70 percent point than metallic blades. Composites have higher cavitation erosion resistance [4] and lesser corrosion property as advantages but unfortunately these materials come at the expense of their limited toughness.

Moreover, its flexibility improves fatigue performance, hydrodynamic efficiency by diminishing fluttering and reduces noise because of improved damping properties. The high grade of design freedom for the shape of the blade by using composite material is one of the best advantage to improve the performance of the blade. The anisotropic material properties of composites allow the hydro-elastic tailoring of the blade, which can be used to improve blade's reliability. The first use of composite marine propellers was on fishing boats in 1960s [5]. In 1974, the performance of 0.25 m to 3 m diameter composite and metal propellers were compared on the commercial ships [6]. The performance of both type of propellers were same in term of engine workload and operating life, but engine and shaft vibration of composite propeller was reduced to 1/4th than conventional one. Various experimental studies are performed to compare hydrodynamic performance of composite and metallic propellers which are explained in the literature [7] and [8].

Wind and tidal-turbine industries encounter similar challenges to enumerate flow-induced deformations. The turbine blades are rotated by the lift forces generated over the blade surface [9]. Maximum wind turbine blades are made of layered composite [10] because of their high stiffness to weight ratio. Titanium and an alloy steels are ruled out for reasons of higher cost and higher specific density. Similarly, tidal-turbine industries are investigating the use of the fiber reinforced composite for underwater turbine applications.

Even multiple advantages of composites over metal and its applicability in various applications, the scope of hydro-elastic tailoring for large composite blade is not much investigated using strongly coupled CFD and FEM simulations. 3D passive control of blade deformation can be exploited by using anisotropic characteristic of laminated fiber reinforced composites [11], [12]. At higher thrust and torque, composite blade undergo automatic pitch, which can be used to reduce the load and stress concentration. The turning in the angle of attack of the blade is called as pitch change. This automatic pitch behavior because of pressure load is insignificant in metallic propellers. Still composite blades are not widely used in many applications under rough conditions because of their inadequate reliable and cost-effective manufacturing techniques [13]. Additionally, the lack of design rules, design tools and reliable simulations are major constraints for the

use of composites for industrial applications. Simulation techniques are needed to estimate accurate blade deformations in the fluid domain and its impact on fluid flow. Moreover, these simulation results will provide opportunity to tailor the composite materials regarding the fiber orientation, number of layers and thickness of each single layer etc.

In recent years, computational fluid dynamic (CFD) and finite element method (FEM) have become most popular techniques to realize the products for various applications at lower cost. But to exploit the benefits of composites, and to apprehend the interaction of fluid and structural domains strong coupling of solver is still needed. In case of large composite propellers neither structural deformations nor change in fluid boundary can be neglected. So, these cases require the coupled solution of fluid dynamics and structure dynamics. The interaction between the flow and the structure takes place only at the interface (the surface of blade and hub). Forces appear on the structural domain boundary because of fluid pressure and shear stresses. These forces deform the structure which leads to a change in the flow field. Therefore, the solution of each solver has to be considered as a boundary condition on the interface for the other solver. FSI simulation results can be used to design and tailor composite blades for higher reliability. Moreover, the flow developed by the propeller and its deformation in real application can be predicted by using FSI simulation results.

The accurate failure prognostics of composite is also another challenge for the reliability of composite products. Numerous theories are given on fracture mechanics to predict behavior of composite during static and dynamic load. Still authentic codes for these criteria are not freely available. So, in house implementation of failure criteria in FEM are needed for 3D tailoring and shape optimization of composite blades.

To focus all the stated issues in the previous paragraphs, a comprehensive study of composite blade is required. For the extensive research two type of turbomachines are selected, former one is submersible mixer and other one is tidal-turbine. Mixer propeller and tidal-turbine blades are made of glass reinforced fiber laminates and random-oriented carbon-fiber reinforced composites respectively. Mixer propeller has large blade deformation opposite to the flow direction and tidal-turbine has large blade deformation in the flow direction. Both are appropriate selection for FSI simulations as they have large

deformations in fluid domain. Additionally, mixer propeller blade is selected because the experimental results were available for the blades and these results are used to validate the numerical setup and simulations results. Tidal-turbine blade is selected to show the application of validated FSI simulation technique, composite material model and failure prognostic code together to tailor the automatic blade pitch behavior in order to reduce the thrust at high inlet velocities.

1.1.1 Submersible mixer propeller

Submersible mixers are highly efficient driving equipment in mixing and plug flow of the media in sewage applications. They are used for homogenization of media and the suspension flow of particles in the sewage tank (Figure 1.1) to avoid sedimentation. Mixers are designed to generate a turbulent flow field behind the blade, which is essential for mixing. By principal, it produces fluid velocity and fluid shear, which imparts kinetic energy to fluid and keeps solid in suspension through frictional forces. During real time operations, these mixers experience heavy thrust and torque at low inlet velocity of fluid which cause blade deformation opposite to the flow direction as depicted in Figure 1.3.



Figure 1.1: Installation of multiple mixers in the mixing tank [14]



Figure 1.2: Permanent failure of the mixer blade while application [14]

Moreover, the thrust on the mixer blades increases even with the increase in density of the propelled fluid. Large deformation and fracture of composite propellers are common issue for mixer industries as shown in Figure 1.2. So, FSI simulation and failure prognostics are needed for the mixer blade design and optimization.

1.1.2 Tidal-turbine

Tidal-turbine is a turbomachine which extract energy from the tides of the sea and ocean. In this application blade deforms in the direction of flow as depicted in Figure 1.4. Similar to mixer propeller, some of the tidal-turbine propellers are made of composite to get all design freedom and advantages of composite. Water is an incompressible high density fluid and it deforms the blade by a large amount at high velocities, which lead to fracture of the blade. To predict final deformation accurately, accurate FSI simulations are needed. The chances of fracture can be reduced by pitching the blades, which is generally used in wind turbine applications at high pressure load. But producing pitch using electronic components is critical for tidal-turbines as it is used inside water. Thus, the tailoring of anisotropic property of the composite material using validated FSI technique can be used to generate controlled blade pitch.

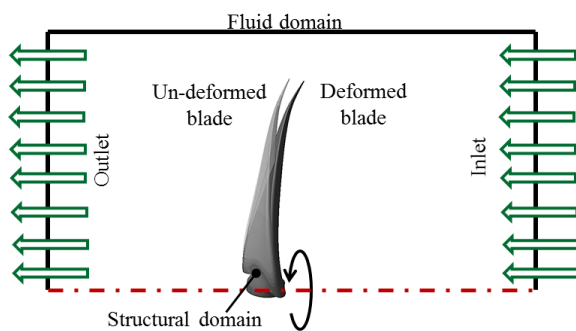


Figure 1.3: Schematic view of the blade deformation in the mixer propeller applications

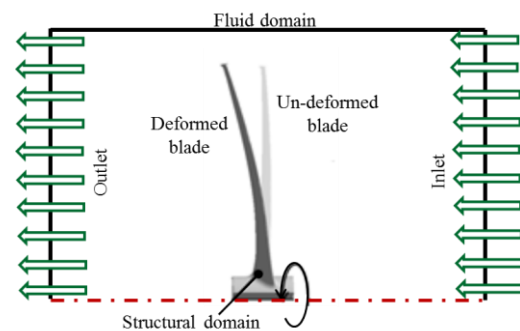


Figure 1.4: Schematic view of the blade deformation in the tidal-turbine application

The motivation of the project is to find stable and efficient fluid-structure interaction technique for the composite blades involving large deformations. Correct CFD and FEA numerical models with failure prognostic code are prerequisite for reliable FSI results of composite blades. The results based on FSI can be used to optimize mixer and tidal-turbine blade design for industrial applications.

2 State of the Art

A detailed literature studies on numerical simulations including experimental analysis are performed for the mixer propellers and tidal-turbines in this chapter. An enriched survey on the failure criteria for the composites and handling of FSI problems are carried out to draw the clear objectives for the research.

2.1 Mixer propeller and tidal-turbine simulations

A propeller generates turbulent jet flow behind its blade as depicted in Figure 2.1. The expanding flow behind the propeller has axial, circumferential and radial velocities. Petersson et al. [15] investigated experimentally the development of the turbulent jet generated by a propeller by Laser Doppler Velocimetry (LDV). Sieg et al. [16], [17] presented characteristics of submerged unconfined swirling jets behavior behind the various size of propellers experimentally using LDV. They proposed generalized formulae based on similarity approach for the velocity distribution versus axial distance behind the propellers. Hörsten et al. [18], [19] extended Sieg's work and simulated various type of propellers considering as a black box model in OpenFOAM [20]. Coefficient of thrust and torque were needed as main input for simulation setup. But finding correct value of thrust and torque coefficients are itself challenging task.

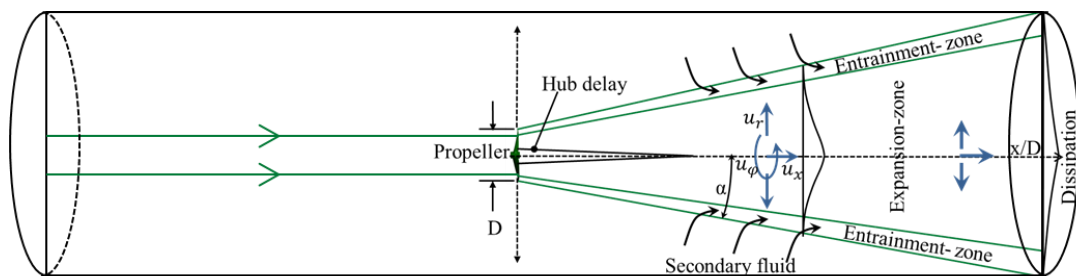


Figure 2.1: Schematic representation of the swirl flow behind a propeller in the style of [16]

Frequently, CFD numerical methods are used to calculate these coefficients. Tian et al. [21] performed numerical simulations of a submersible mixer with two blades using

Fluent with tetrahedral mesh and just they presented the development of swirl jet flow. Weixing and Jianping [22] investigated the flow behind mixer propeller using $k-\varepsilon$ turbulence model and stated that the smaller hub diameter of mixer blade increases the advancing speed of fluid. But the reason for the selection of $k-\varepsilon$ turbulence model is not discussed. Kumar et al. [23] studied the effect of mixer blade geometry and deformation on the jet flow shape. Moreover, they presented the effect of change in size or speed of blade on the power, thrust and torque of the propeller blades.

Estimating correct value of thrust and torque at very low inlet velocity of fluid is very important for the mixer blade design and applications. But, these values depend significantly on turbulence model, mesh quality and boundary conditions [24]. Literatures regarding effect of turbulence models on thrust and torque values are scarce. Moreover, published study on the simulation results of mixer blade using CFD method at inlet velocity lesser than 0.2 m/s is very limited.

Similar to mixer propellers, tidal-turbines are also subjected to large thrust loading in inflow direction and torsional bending because of the higher density of seawater. Lee et al. [25] used blade element method (BEM) and CFD for performance analysis of a horizontal axis tidal stream turbine. They used SST model for CFD analysis but the reason for selection is not mentioned. Lloyd et al. [26] used large eddy simulation for assessing the influence of inflow turbulence on noise and performance of tidal-turbine using Open FOAM. Still, validated efficient turbulence model and correct numerical setting are needed for thrust and torque estimation for tidal-turbine too.

2.2 Modelling of composites material and failure prognostic

The fiber-reinforced composites have been used in propeller and turbine manufacturing because of its greater advantages over metals such as high strength-to-weight ratio, fatigue strength, damping and better cavitation erosion resistance. An efficient computation of layered composites requires correct and robust mesh element formulation. Grogan et al. [27] used glass fiber-reinforced polymer (GFRP) and carbon fiber-reinforced polymer (CFRP) to compare the structural performance of tidal-turbine blades using 3D shell element for the FE analysis. CFRP exhibited more sustainability than GFRP under similar loading condition. Klinkel et al. [28] proposed 3D shell elements

for a nonlinear analysis of laminated shell structures. Moreira et al. [29] formulated 8-node hexahedral solid-shell elements based on Enhanced Assumed Strain method (EAS). Naceur et al. [30] formulated a composite 8-node solid shell element including anisotropic material behavior of layer. Still solid shell elements are more prone to shear and thickness locking than solid elements. Delamination cannot be modelled using shell elements. Modelling each layer of composite using solid elements will be more logical than using shell elements. Literature studies on reliable numerical model to predict the structural behavior of layered composites are scarce.

Beside selection of correct element type, fracture modelling and failure prognostic are still a complicated challenge. In general one ply is glued over another ply while manufacturing layered type of composites. Delamination of these plies is general problem. Cohesive zone model (CZM) method is used to describe glue behavior and inter laminar failure. Pereira and Morais [31] proposed the CZM model for delamination of double cantilever beam. Further, Morais [32] demonstrated that shear foundation can be discarded for mode I delamination analysis.

Various theories are given for fracture modelling of composites. Hinton et al. [33] tested 12 leading theories for predicting failure in composite laminates against experimental evidence. The proposed theory of Zinoviev and Puck scored highest compared to all other theories. In 2002, Kaddour et al. [34] compared 14 international recognized failure theories for FRPs where Cuntze criteria [35] was observed as the best theory for failure prediction. In 2005, Pinho et al. [36] proposed advanced three-dimensional failure criteria for laminated FRP denoted as LaRC, based on a physical model for each failure mode and non-linear matrix shear behavior. Implementing in house code for LaRC was needed for failure prognostics in this project and it must be compared with well know criteria to justify its advantages.

An extensive literature studies about flow simulations and modelling technique for composite propellers are compiled in the section 2.1 and section 2.2. In next section an detailed literature study is performed for various available FSI techniques and algorithms used for predicting flow-induced deformation and its consequence on the fluid domain. Moreover, the state of the art for handling FSI of composite propeller is discussed.

2.3 Handling of fluid-structure interaction problems

The strong nonlinearity and multi-physics analysis brings a challenge for a comprehensive study of FSI problems [37]. Moreover, the scope of laboratory experiments for rotating blade FSI is limited. Thus an extensive investigation of numerical techniques is involved for the coupled interaction of fluids and structures. An approach used to handle FSI problem can be divided into *monolithic approach* or *partitioned approach* based on the numerical coupling of field solver equations [38].

In the monolithic approach (Figure 2.2), a unified algorithm is used to solve simultaneously fluid and structural dynamics system equations by converting them into single system equation [39], [40]. This approach is fully coupled and more accurate for multi-physics problem but it needs an efficient computer code and huge computational power.

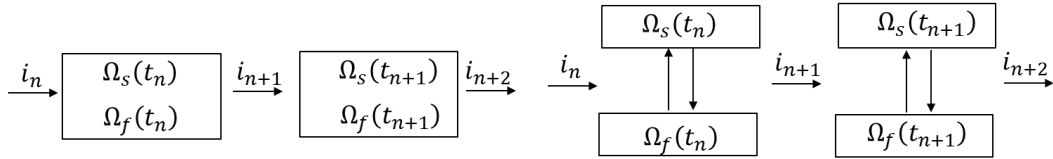


Figure 2.2: Monolithic approach for FSI

Figure 2.3: Partitioned approach for FSI

In the partitioned approach, fluid and structural fields are solved separately using mesh discretization and numerical algorithms (control volume method and finite element method) as shown in Figure 2.3. This approach is easier to implement because an efficient, robust and fast CFD and FEM commercial codes are already available for industrial applications.

The shape of interface in the fluid and structural domain changes with time which must be updated while simulation. So the treatment of mesh deformations inside domain becomes essential constraint. Based on treatment of mesh, FSI handling method can be divided into *conforming mesh method* (Figure 2.4) and *non-conforming mesh method* (Figure 2.5). Former method need mesh smoothing and re-meshing algorithm during simulation while the latter method doesn't.

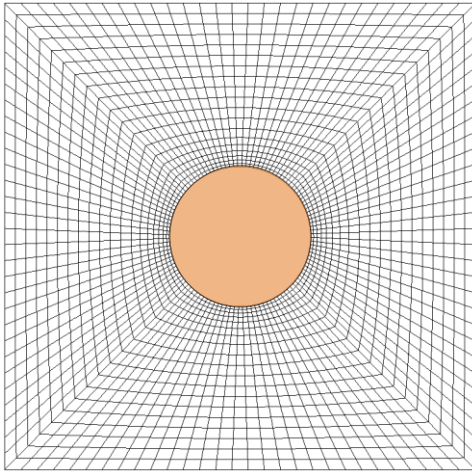


Figure 2.4: Grid for conforming mesh method where nodes of fluid domain lying on structural domain interface surface

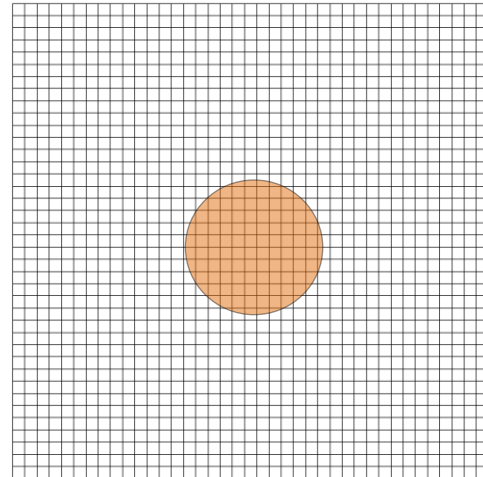


Figure 2.5: Grid for non-conforming mesh method where nodes at interface for both domains are not conformed

Most researchers are focusing on *partitioned conforming mesh approach* for the investigation of FSI because data communication on interface is more accurate than other one. The *partitioned conforming mesh approach* can be further divided into *an implicit* and *an explicit approach* based on the data exchange. Park and Fellipa introduced partitioned for coupled systems [41]–[43]. Sieber developed an explicit and an implicit loose coupling algorithm using finite volume code FASTEST-3D and the finite element program FEAP. But FSI was done for small deformation of the isotropic elastic structures. Further, Xingyuan et al. [44] applied implicit partitioned coupling algorithm for FSI using FASTEST-3D and FEAP codes to investigate viscoelastic Oldroyd-B fluid and elastic structure. Morand and Ohayon presented applied numerical methods for FSI to calculate flow induced linear vibration of elastic structures [45]. Coupled 3-D FEM/VLM (PSF-2) method was presented by Lin and Lin [46] for a propeller where geometrical nonlinearity of structures was included and in 1997 they applied same procedure for a layered composite propeller [47].

Taltec and Mouro [48], simulated the fluid-structure interaction with large displacements, where the structure is examined using a Lagrangian description and an Arbitrary Lagrangian Eulerian (ALE) formulation for the fluid. Later, Taltec et.al [49] analyzed fluid-structure problems in large deformations of the flexible body. They introduced nonlinear time integration energy conserving scheme for compressible

stiffness, fluid convection etc. Flow induced oscillation of a single bladed sewage water pump was investigated by Benra [50] using one way coupling method in commercial software. Data exchanged was performed via output file at interface surfaces.

In 2008 Young [51] exploited the advantages of composite propellers by using a coupled 3-D BEM/FEM computational model to study the fluid-structure interaction for flexible propeller in sub-cavitation and cavitation flow. In 2011 Campbell and Peterson [52] developed and validated FSI of expandable impeller pump using OpenFOAM. Moreover, they developed structural solver in house for FEM simulation. Hsu and Bazilevs [53] performed strongly coupled FSI of wind turbine where the aerodynamics were computed using low-order finite element based ALE-VMS technique. The blades were modelled as thin composite shell discretized using NURBS-based isogeometric analysis. Nayer and Breuer [54] investigated experimentally and numerically the FSI of a flexible blade behind the cylinder using partitioned coupling scheme with LES.

Very limited literature studies are published regarding implicit partitioned conforming mesh approach based FSI of layered composite blade involving large deformation by using commercially available CFD and FEM codes. In next section objectives of current research are compiled based on extensive literature studies.

2.4 Objective

The objective of this research work was to perform efficient and correct fluid-structure interaction of composite blade involving large deformation. This objective needs some prerequisite studies regarding correct numerical setup for the fluid and structural domains.

The first target of the project was to find appropriate turbulence model in commercially available CFD solver codes for correct estimation of thrust and torque based on experimental evidence. Moreover, thrust and torque values are sensitive to inlet velocity of fluid and other boundary conditions. Extensive CFD study was required to figure out a correct numerical model to create benchmark for fluid-structure interaction (FSI) analysis.

The second target was to create a numerical model for layered composites using finite element method (FEM) in order to understand the interaction of each layer and location of stress concentration. Anisotropic material data was created for composite blade and validation of material model was performed using an optical measurement method. Failure prognostic codes were developed in house based on latest theories of Tsai-Wu, Puck and LaRC criteria to predict the position of fracture on the blade at heavy load condition.

The main motive of this study was to perform strongly coupled FSI simulations for composite blades. The mesh deformation and domain re-meshing methods are used to handle large deformations. These techniques facilitate researchers to perform 3D tailoring of composite blades based on the results obtained from strong coupling of the fluid and the structural domain.

The stable FSI simulation technique and anisotropic material property are used together as a tool to design a composite connector between the hub and blade of the tidal-turbine. Connector pitches the blade to prevent fracture under rough conditions (large deformation at high thrust). A complete process followed in this research work is schematically shown in Figure 2.6.

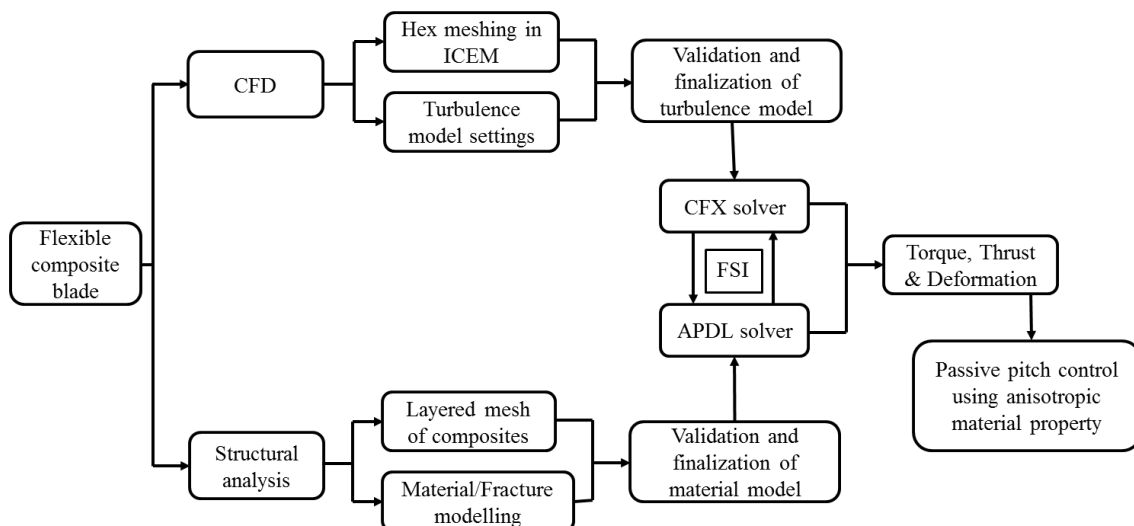


Figure 2.6: Detailed work-flow chart to perform a comprehensive study and fluid-structure interaction of composite blade.

3 Mathematical modelling

Mathematical models and algorithms are needed to perform numerical analysis for any fluid or structures to understand its behavior under various boundary conditions. Computational fluid dynamics (CFD) is a branch of the fluid mechanics that uses numerical modelling and simulation to analyze the fluid flows.

3.1 Computational fluid dynamics

3.1.1 Governing equations

In analyzing fluid motion, flow patterns must be described at every point $P(x, y, z)$ in the *Eulerian* space. Basically, velocity and pressure distribution are numerically calculated using CFD method. The Cartesian vector form of a velocity field which varies in space and time is explained in Eq.(1). Mass conservation (Eq.(3)) and momentum conservation (Eq.(4)) are basic conservation laws which are applied to an infinitesimal incompressible fluid system [55], [56]. For Newtonian flow, the viscous forces are proportional to the product of element strain rate and the coefficient of viscosity as written in Eq.(5). After this modification, these equations are known as Navier-Stokes equations. The equations are nonlinear partial differential transport equations. The nonlinearity is because of convection acceleration which is associated with the change in velocity over position.

Velocity Vector

$$\vec{V}(r, t) = u(x, y, z, t) \hat{i} + v(x, y, z, t) \hat{j} + w(x, y, z, t) \hat{k} \quad (1)$$

Divergence of Vector

$$\nabla \cdot \vec{V} = \frac{\partial u}{\partial x} + \frac{\partial v}{\partial y} + \frac{\partial w}{\partial z} \quad (2)$$

Mass conservation

$$\nabla \cdot (\rho \vec{V}) = 0 \quad (3)$$

Momentum conservation

$$\rho \left(\underbrace{\frac{\partial \vec{V}}{\partial t}}_{\text{Local acceleration}} + \underbrace{\vec{V} \cdot \nabla \vec{V}}_{\text{Convective Acceleration}} \right) = - \underbrace{\nabla p}_{\text{Pressure forces}} + \underbrace{\nabla \cdot \tau_{ij}}_{\text{Viscous forces}} + \underbrace{F_b}_{\text{Body forces}} \quad (4)$$

Viscous force

$$\tau_{ij} = \mu \begin{bmatrix} 2 \frac{\partial u}{\partial x} - 2/3(\nabla \vec{V}) & \frac{\partial u}{\partial y} + \frac{\partial v}{\partial x} & \frac{\partial u}{\partial z} + \frac{\partial w}{\partial x} \\ \frac{\partial u}{\partial y} + \frac{\partial v}{\partial x} & 2 \frac{\partial v}{\partial y} - 2/3(\nabla \vec{V}) & \frac{\partial v}{\partial z} + \frac{\partial w}{\partial y} \\ \frac{\partial u}{\partial z} + \frac{\partial w}{\partial x} & \frac{\partial v}{\partial z} + \frac{\partial w}{\partial y} & 2 \frac{\partial w}{\partial z} - 2/3(\nabla \vec{V}) \end{bmatrix} \quad (5)$$

The numerical solution of the Navier-Stokes equation to capture turbulent flow correctly requires a very fine mesh resolution and time resolution. This increases computational time significantly, which is infeasible for frequent calculations. To solve stated problem *Reynolds-averaged Navier-Stokes equations* are used.

3.1.2 Reynolds-averaged Navier-Stokes equations (RANS)

An idea to decompose an instantaneous quantity into its time averaged and fluctuating quantities was introduced by Reynolds (1895) [57]. The instantaneous velocity $u_i(t)$ can be decomposed in fluctuating and time averaged component as shown in Eq.(6).

$$u_i(t) = \underbrace{\bar{u}_i}_{\text{Time averaged component}} + \underbrace{u'_i}_{\text{Fluctuating component}} \quad (6)$$

Mass balance after Reynolds averaging

$$\frac{\partial(\bar{u}_i)}{\partial x} = 0 \quad (7)$$

Momentum balance after Reynolds averaging

$$\rho \left(\frac{\partial \bar{u}_i}{\partial t} + \bar{u}_j \frac{\partial \bar{u}_i}{\partial x_j} \right) = -\frac{\partial \bar{p}}{\partial x_i} + \mu \frac{\partial}{\partial x_j} \left(\frac{\partial \bar{u}_i}{\partial x_j} + \frac{\partial \bar{u}_j}{\partial x_i} - \frac{2}{3} \frac{\partial \bar{u}_k}{\partial x_k} \delta_{ij} \right) - \underbrace{\rho \left(\frac{\partial \overline{u'_i u'_i}}{\partial x_j} \right)}_{\text{Reynolds stresses}} + F_b \quad (8)$$

The Reynolds averaging produces additional unknown terms called as *Reynolds stresses* as shown in Eq.(8). To achieve “closure” the Reynolds stresses must be modelled further by equations of known quantities. In 1877 Boussinesq [58] proposed a formula to define Reynolds stresses based on molecular viscosity theory which is given in Eq.(9). The final RANS equation for momentum equation after adding Boussinesq eddy viscosity model is defined in Eq.(10).

$$-\overline{\rho u'_i u'_i} = \bar{\tau}_{ij} = \mu_t \left(\frac{\partial \bar{u}_i}{\partial x_j} + \frac{\partial \bar{u}_j}{\partial x_i} \right) - \frac{2}{3} \left(\rho k + \mu_t \frac{\partial \bar{u}_k}{\partial x_k} \right) \delta_{ij} \quad (9)$$

$$\rho \left(\frac{\partial \bar{u}_i}{\partial t} + \bar{u}_j \frac{\partial \bar{u}_i}{\partial x_j} \right) = -\frac{\partial \bar{p}}{\partial x_i} + \frac{\partial}{\partial x_j} \left[\mu_{eff} \left(\frac{\partial \bar{u}_i}{\partial x_j} + \frac{\partial \bar{u}_j}{\partial x_i} - \frac{2}{3} \frac{\partial \bar{u}_k}{\partial x_k} \delta_{ij} \right) \right] - \frac{2}{3} \rho k \delta_{ij} + F_b \quad (10)$$

$$\mu_{eff} = \mu + \mu_t \quad (11)$$

Here, μ, μ_t are known as normal and turbulent viscosity respectively. The concept of turbulent viscosity is phenomenological and has no mathematical basis. Again, it should be modeled to achieve closure. Numerous models are available in which two equations eddy viscosity turbulence models are used more frequently, which is explained in next sections.

3.1.3 Turbulence models: Two equation models

Two equation models apply one partial differential equation for turbulence length scale and other for turbulent velocity scale. *k-ε*, *k-ω* and SST turbulence models are widely used. Basic equations for these turbulence models are shown from Eq.(12) to Eq.(20).

k-ε model:

$$\mu_t = \rho C_\mu \frac{k^2}{\varepsilon} \quad (12)$$

$$\rho \left(\frac{\partial k}{\partial t} + \bar{u}_j \frac{\partial k}{\partial x_j} \right) = \frac{\partial}{\partial x_j} \left[\left(\mu + \frac{\mu_t}{\sigma_k} \right) \frac{\partial k}{\partial x_j} \right] - \rho \varepsilon + P_k + P_{kb} \quad (13)$$

$$\rho \left(\frac{\partial \varepsilon}{\partial t} + \bar{u}_j \frac{\partial \varepsilon}{\partial x_j} \right) = \frac{\partial}{\partial x_j} \left[\left(\mu + \frac{\mu_t}{\sigma_\varepsilon} \right) \frac{\partial \varepsilon}{\partial x_j} \right] + \frac{\varepsilon}{k} (C_{\varepsilon 1} P_k - C_{\varepsilon 2} \rho \varepsilon + C_{\varepsilon 1} P_{\varepsilon b}) \quad (14)$$

Here, $C_{\varepsilon 1}$, $C_{\varepsilon 2}$, σ_ε and σ_k are constant. P_{kb} and $P_{\varepsilon b}$ represent the influence of buoyancy forces. P_k is the production rate of turbulence.

k-ω model:

$$\mu_t = \rho \frac{k}{\omega} \quad (15)$$

$$\rho \left(\frac{\partial k}{\partial t} + \bar{u}_j \frac{\partial k}{\partial x_j} \right) = \frac{\partial}{\partial x_j} \left[\left(\mu + \sigma_k \mu_t \right) \frac{\partial k}{\partial x_j} \right] - 0.09 \rho k \omega + P_k + P_{kb} \quad (16)$$

$$\rho \left(\frac{\partial \omega}{\partial t} + \bar{u}_j \frac{\partial \omega}{\partial x_j} \right) = \frac{\partial}{\partial x_j} \left[\left(\mu + \sigma_\omega \mu_t \right) \frac{\partial \omega}{\partial x_j} \right] - 0.075 \rho \omega^2 + 0.55 \frac{\omega}{k} P_k + P_{\omega b} \quad (17)$$

Here, σ_ω and σ_k are constant. P_{kb} and $P_{\omega b}$ represents the influence of buoyancy forces. P_k is production rate of turbulence. $k-\varepsilon$ is not able to capture turbulent boundary layer behavior up to separation but $k-\omega$ is more accurate in near to the wall layers. So, blending functions are introduced for zonal formulation to ensure proper selection of $k-\varepsilon$ and $k-\omega$ while simulations [59].

SST turbulence model:

SST turbulence model is a type of turbulence model equipped with the blending function to get the advantages of ***k-ε model*** and ***k-ω model***. Basic equation of SST turbulence model is shown from Eq.(18) to Eq.(20). Here, F_1 and F_2 are blending functions. A complete formulation and industrial experience of SST model is discussed in [60].

$$\mu_t = \rho \frac{0.31k}{\max(0.31\omega, \Omega F_2)} \quad (18)$$

$$\rho \left(\frac{\partial k}{\partial t} + \bar{u}_j \frac{\partial k}{\partial x_j} \right) = \frac{\partial}{\partial x_j} \left[(\mu + \sigma_k \mu_t) \frac{\partial k}{\partial x_j} \right] - 0.09 \rho k \omega + P_k + P_{kb} \quad (19)$$

$$\begin{aligned} \rho \left(\frac{\partial \omega}{\partial t} + \bar{u}_j \frac{\partial \omega}{\partial x_j} \right) &= \frac{\partial}{\partial x_j} \left[(\mu + \sigma_\omega \mu_t) \frac{\partial \omega}{\partial x_j} \right] - 0.075 \rho \omega^2 + 0.55 \frac{\omega}{k} P_k + \\ &2(1 - F_1) \frac{0.856 \rho}{\omega} \frac{\partial k}{\partial x_j} \frac{\partial \omega}{\partial x_j} + P_{\omega b} \end{aligned} \quad (20)$$

Gamma-Theta transition model:

The transition of flow from laminar to turbulent is a general behavior of flow over a surface at high Reynolds number. The transition have a strong influence on boundary layer separation over the flow surface. The location of transition plays major role in design and performance of turbomachines where the wall shear stress is important. The recent methods for the transition prediction can be found in [61], [62]. It is essential to calculate for the prediction of natural and bypass transition point accurately. So, additional two transport equations are added with previous two equation turbulence model i.e. one for intermittency (γ) and other for transition momentum thickness Reynolds number ($Re_{\theta t}$) as shown in Eq.(21) and Eq.(22). Intermittency is used to trigger transition locally. And other is required to capture nonlocal influence of the turbulence intensity. Based on the relationship between strain rate and transition momentum thickness Reynolds number, the production term of turbulent kinetic energy is turned on downstream of the transition point.

$$\rho \left(\frac{\partial \gamma}{\partial t} + \bar{u}_j \frac{\partial \gamma}{\partial x_j} \right) = \frac{\partial}{\partial x_j} \left[\left(\mu + \frac{\mu_t}{\sigma_\gamma} \right) \frac{\partial \gamma}{\partial x_j} \right] + P_{\gamma 1}(1 - \gamma) + P_{\gamma 2}(1 - 50\gamma) \quad (21)$$

$$\rho \left(\frac{\partial Re_{\theta t}}{\partial t} + \bar{u}_j \frac{\partial Re_{\theta t}}{\partial x_j} \right) = \frac{\partial}{\partial x_j} \left[2(\mu + \mu_t) \frac{\partial Re_{\theta t}}{\partial x_j} \right] + P_{\theta t} \quad (22)$$

$$\rho \left(\frac{\partial k}{\partial t} + \bar{u}_j \frac{\partial k}{\partial x_j} \right) = \frac{\partial}{\partial x_j} \left[(\mu + \mu_t \sigma_k) \frac{\partial k}{\partial x_j} \right] - \bar{D}_k + \bar{P}_k \quad (23)$$

Transition model interacts with the $k-\omega$ model and changes turbulent kinetic energy equation as shown in Eq.(23). Here \bar{P}_k , $P_{\gamma 1}$ and $P_{\theta t}$ are source terms. $P_{\gamma 2}$ and \bar{D}_k are destructive terms. To capture laminar and transition boundary layer the dimensionless wall distance y^+ should be equal to one for accurate boundary layer solutions. Dimensionless wall distance is defined in Eq. (24), where u_τ is frictional velocity, y is the distance to the nearest wall and ν is kinetic viscosity.

$$y^+ = u_\tau y / \nu \quad (24)$$

There are other models like *Reynolds stress model*, *Large eddy simulation model (LES)*, *Detached eddy simulation model (DES)* and *Direct numerical simulation model (DNS)* are available. These models require high computational power and time. In this project only eddy viscosity models are focused to find a flow field of submersible mixer and tidal-turbines.

Till now, theoretically it was identified that the SST turbulence model with Gamma-Theta transition model should be suitable numerical model to simulate the blade to solve flow fields at high Reynolds number. But to make benchmark, numerical simulations are performed using *k- ϵ model*, *k- ω model*, *SST Model* and *SST model with Gamma-Theta Transition model*. All results are presented in ‘chapter 4’ in detail and comparative study is performed for selected turbulence model settings.

3.2 Finite element analysis

Many physical phenomena in engineering can be described in terms of partial differential equations (PDE). In general, solving these equations by classical analytical methods for arbitrary shapes is almost impossible. The finite element method (FEM) is a numerical approach by which these PDE can be solved approximately. FEM are widely used in diverse fields to solve static and dynamic structural problems.

3.2.1 Governing equations

In FEM analysis, a structure is divided into small pieces by using elements and nodes. Then the behavior of physical quantities on each node is described. After that, the elements are connected at the node to form an approximate system of equations for the

whole structure. Finally systems of equations involving unknown quantities at the nodes are solved and desired quantities are calculated. The system of equation using finite element method is presented in Eq.(25). Here, u_s denotes the structural displacement in Lagrangian frame and M is the mass matrix [63]. The term K is the usual stiffness matrix which is constant for linear elastic behavior and depends on the displacement for non-linear elastic behavior. The deformation in steady or transient structural simulations can be calculated using total Lagrangian (TL) approach. Moreover, the final static deformation of structure for given load does not depend on inertia of structure. Thus governing equation for structural analysis could be reduced to Eq.(26)

$$M\ddot{u}_s + C(\dot{u}_s) + K(u_s) = F \quad (25)$$

$$K^t(\Delta u_s) = F^t \quad (26)$$

3.2.2 Element type

It is already mentioned that the selected mixer blade has layered composite material. It became important to understand which type of finite element should be used to model layered composite. The grid with shell elements are huge time saving model for analysis but there are few practical issues here. There is lack of technique for the proper contact definition between two layers. Correct mesh modelling of trailing edges of the blade was just impossible by using shell element.

Even solid elements are computationally expensive but these elements are better for modelling layered composite. More realistic boundary conditions is reached using solid element like faces is used rather than edges along thickness direction. Contact definition is precise and trailing edge can be modelling easily. Layered-solid element is considered for modelling layered composites. Multiple solid elements are used over the thickness to reduce stiffness and locking of element during bending.

3.2.3 Glue modelling

Adhesive bonding is new and fast developing technique for joining structural elements. Properly designed adhesive bonds may be more efficient than mechanical fasteners. But delamination of layers is a common problem in adhesive bonded products.

Different modes of delamination are shown in Figure 3.1. Mode-1 debonding defines a mode of separation of the interface surfaces when normal stress dominates the shear stress. Mode-2 and mode-3 are modes of separation when shear stress dominates.

Discrete Cohesive Zone Model (DCZM) is used for stiffness calculation of glue (Figure 3.2) [64]. The normal contact stress (tension) and contact gap behavior is plotted in Figure 3.3. It shows linear elastic loading followed by linear softening. Debonding begins at the peak of elastic loading, where maximum normal contact stress is achieved. It is completed at the point when the normal contact stress reaches zero value. After that, any further separation occurs without any normal contact stress.

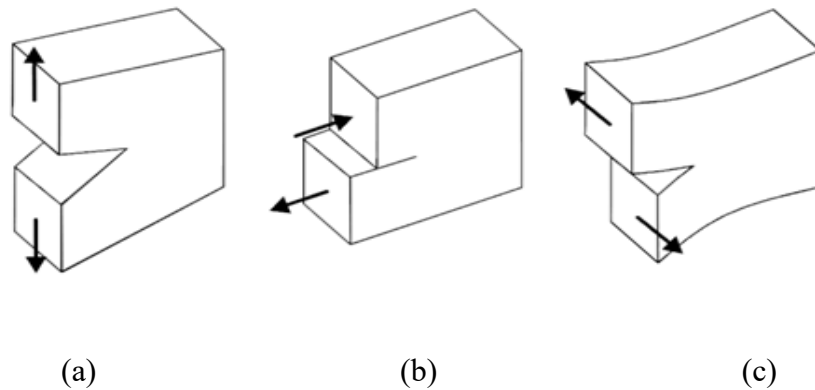


Figure 3.1: Different modes of delamination in layered composites (a) Interlaminar tension failure; (b) Interlaminar sliding shear failure; (c) Interlaminar scissoring shear failure

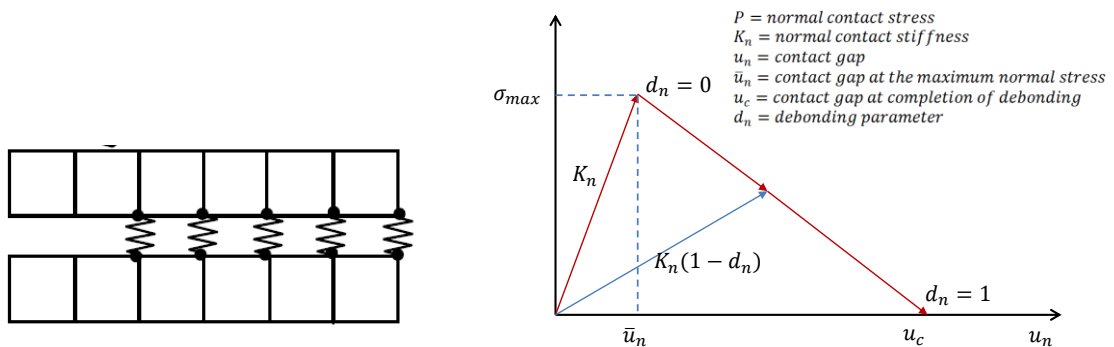


Figure 3.2: Spring foundation and discrete element in Cohesive Zone Model[64]

Figure 3.3: Stress development and debonding law for DCZM

After debonding has been initiated it is assumed to be cumulative. Any subsequent unloading and reloading occurs in a linear elastic manner along blue line as shown in Figure 3.3. This technique is used to model glue in the blade. It is very important to know

the correct value of maximum normal contact and tangential contact stress including contact gap at the complete debonding.

3.3 Failure prognostic modelling of composite

Laminated composite materials are formed by stacking two or more layers together with a suitable adhesive material called plies or laminae. The stiffness and strength of plies can be customized to provide desired stiffness and strength for the ply. Each lamina or ply consists of long fibers embedded in a matrix material. Typical fiber materials used are glass and carbon. In some applications the matrix material can be metallic or ceramic. Most commonly used matrix materials are polymers such as epoxies and polyamides. The orientation of fibers in each laminate may differ as per required strength and stiffness considerations. The individual laminae are generally orthotropic i.e. material properties differ along the orthogonal directions or transversely isotropic which means that material properties differ along the in-plane orthogonal directions and remain isotropic in the transverse directions. Numerical modelling to predict failure of composite materials is a challenging task. To evaluate failure it is important to know the type of failure modes in composite which are discussed in next sections.

3.3.1 Main failure modes in fiber reinforced laminated composites

Laminated composites either consisting of unidirectional or woven fibers, can fail in a number of modes. Depending on loading conditions, various modes of failure are observed in composite material which are matrix delamination (Figure 3.1), matrix tensile failure, fiber tensile failure, matrix compressive failure and fiber compressive failure as displayed in Figure 3.4.

In laminated materials, repeated cyclic stresses cause layers to separate with significant loss of mechanical toughness. This is known as delamination (Figure 3.1). The fracture surface resulting from the matrix tensile failure mode (Figure 3.4(a)) is normal to the loading direction. Some fiber splitting at the fracture surface can be usually observed. This failure basically occurs under the application of transverse tensile load. This type of failure is known as inter-fiber failure (IFF). Matrix compressive failure (Figure 3.4(c)) is an inter-fiber failure, which is actually a shear matrix failure. This

failure occurs at an angle with the loading direction, which proves the shear nature of the failure process. Fiber tensile failure (Figure 3.4(b)) basically occurs under the application of longitudinal tensile load. Fiber compressive failure mode (Figure 3.4(d)) is largely affected by the resin shear behavior and imperfections (like fiber misalignment angle and voids).

Various efficient failure prognostic theories are available. Three theories are selected based on worldwide failure exercise [33], [34], [65] for the fracture modelling, which is explained in next section. In house codes for selected theories are developed to simulate the failure of composite blade numerically.

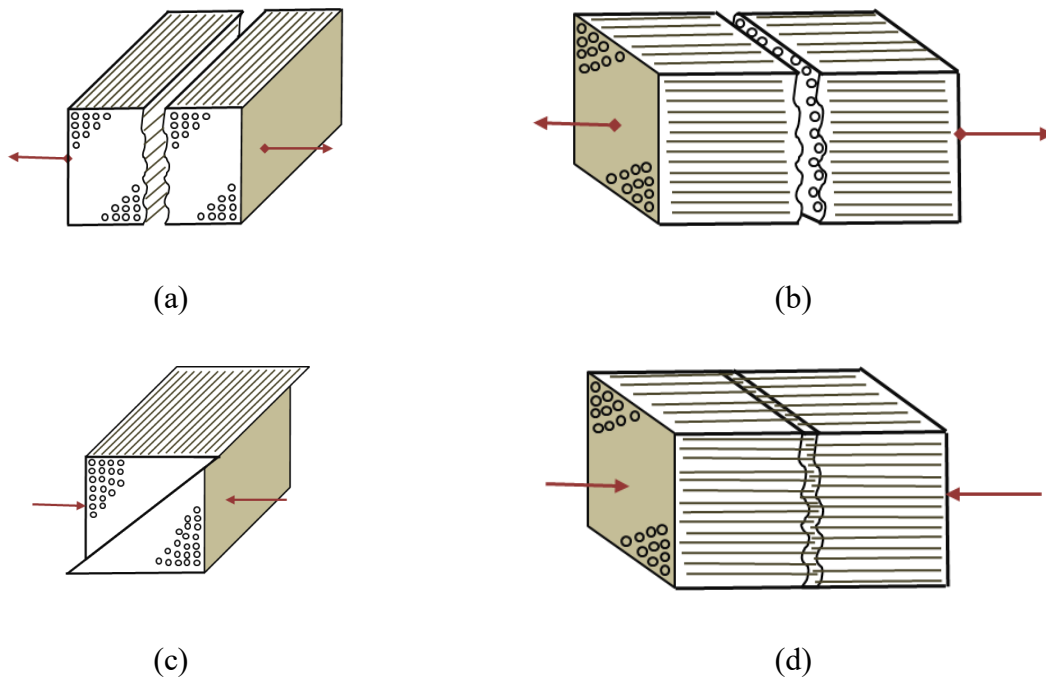


Figure 3.4: (a) Matrix tensile failure, (b) Fiber tensile failure, (c) Matrix compressive failure and (d) Fiber compressive failure. Red arrow is showing the direction of applied force.

3.3.2 Theories for failure prognostics

The uncertainty in the fracture prediction for composites material motivates to revisit the existing failure theories and to develop in house code where necessary. In this section, three existing phenomenological criteria for predicting failure of composite structures are described which are Tsai-Wu failure criterion, Rankine's failure criteria and LaRC failure criteria.

3.3.2.1 Tsai-Wu failure criterion

The Tsai-Wu failure criterion is widely used for failure prognostic of anisotropic composite materials. This failure criterion is expressed as Eq.(27).

$$f_i \sigma_i + f_{ij} \sigma_i \sigma_j \leq 1 \quad (27)$$

This equation evolved from the general quadratic failure criterion proposed by Gol'denblat and Kopnov [66]. In the above equation, i and j are indices varying from 1-to-6; f_i and f_{ij} are experimentally determined material strength and σ_i takes into account internal stresses which can describe the difference between positive and negative stress induced failures. The quadratic term $\sigma_i \sigma_j$ defines an ellipsoid in space. The Tsai-Wu failure criterion accounts for stress interactions. Once all the strength parameters are known the Tsai-Wu failure index can be calculated (Eq.(28)). If the failure index is greater than 1, failure occurs. The value of the failure index can be determined by the Eq.(31) and Eq.(32) .

$$\text{Failure Index} = A + B \quad (28)$$

$$\text{Failure Index} \leq 1; \text{ Safe} \quad (29)$$

$$\text{Failure Index} \geq 1; \text{ Fracture} \quad (30)$$

$$A = -\frac{(\sigma_x)^2}{f_{xt}f_{xc}} - \frac{(\sigma_y)^2}{f_{yt}f_{yc}} - \frac{(\sigma_z)^2}{f_{zt}f_{zc}} + \frac{(\sigma_{xy})^2}{(f_{xy})^2} + \frac{(\sigma_{yz})^2}{(f_{yz})^2} + \frac{(\sigma_{xz})^2}{(f_{xz})^2} \quad (31)$$

$$+ \frac{C_{xy}\sigma_x\sigma_y}{\sqrt{f_{xt}f_{xc}f_{yt}f_{yc}}} + \frac{C_{yz}\sigma_y\sigma_z}{\sqrt{f_{yt}f_{yc}f_{zt}f_{zc}}} + \frac{C_{xz}\sigma_x\sigma_z}{\sqrt{f_{xt}f_{xc}f_{zt}f_{zc}}}$$

$$B = \left[\frac{1}{f_{xt}} + \frac{1}{f_{xc}} \right] \sigma_x + \left[\frac{1}{f_{yt}} + \frac{1}{f_{yc}} \right] \sigma_y + \left[\frac{1}{f_{zt}} + \frac{1}{f_{zc}} \right] \sigma_z \quad (32)$$

Where, C_{xy} , C_{yz} & C_{xz} =x-y, y-z & x-z, coupling coefficients for Tsai-Wu theory. The equations used here are the 3D versions of the failure criterion for the strength index [67]. A complete derivation of Tsai-Wu failure criterion is presented in appendix 'A'.

3.3.2.2 Puck's failure Criteria

Puck's failure criteria are one of the direct mode criteria, which distinguish fiber failure and matrix failure. These criteria are an interactive stress-based criteria valid for uni-directional composite (UDC) lamina. Puck and Schürmann [68] presented a physically based 'action plane' criteria for failure prediction in UDC. The Puck's failure theory is based on Mohr-Coulomb hypothesis of brittle fracture. Puck was the first author, who published the idea that fiber failure (FF) and inter-fiber failure (IFF) should be distinguished. Theoretically it should be treated by separate and independent failure criteria. To differentiate certain types of stresses Puck introduced the term 'Stressing' to explain proposed failure theory. The basic stressing on UDC elements is as shown in the Figure 3.5. In this figure σ_{\parallel} (tensile or compressive) is responsible for FF whereas $\sigma_{\perp}, \tau_{\perp\perp}, \tau_{\perp\parallel}$ stressing lead to IFF.

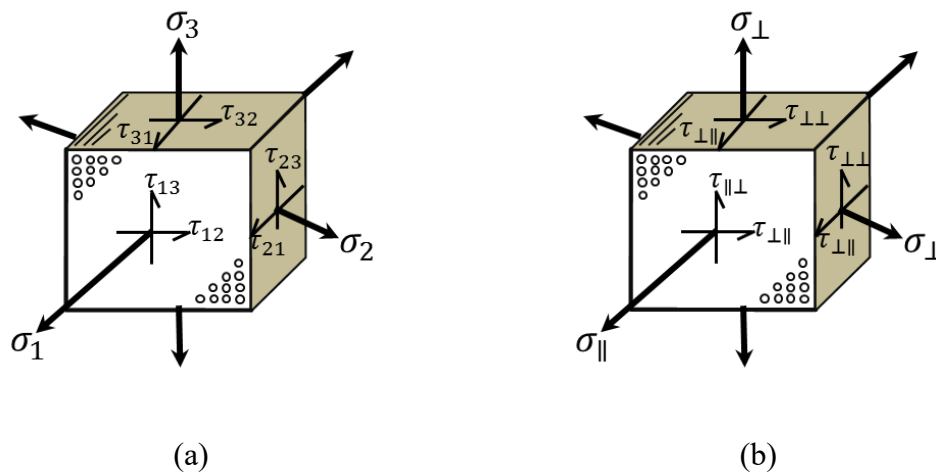


Figure 3.5: The basic stressing on uni-direction composite elements

There are three action planes in which fracture occur in composite materials [69]. Puck modified the Mohr-Coulomb criteria and proposed that the stresses on the action plane are decisive for fracture. This hypothesis is easy to understand but very difficult to analyse because the position of the action plane is unknown. Thus, the position of the action plane should be found out using a suitable brittle failure criterion and this criterion should depend on the stresses acting on this plane. This hypothesis says that the normal stress σ_n and the shear stresses τ_{nt} and τ_{n1} on the action plane are decisive for Inter-Fiber Failure (IFF).

The stresses σ_n , τ_{nt} and τ_{n1} are the stresses acting on the plane at which the fracture occurs. This fracture plane is inclined at an angle θ_{fp} . The stresses σ_n , τ_{nt} and τ_{n1} are proportional to the global stresses represented as σ_2 , σ_3 , τ_{23} , τ_{31} and τ_{21} (Figure 3.5(a)) or σ_{\perp} , σ_{\parallel} , $\tau_{\perp\perp}$, $\tau_{\perp\parallel}$ and $\tau_{\parallel\parallel}$ (Figure 3.5(b)). Complete derivation of the criteria are explained in appendix ‘ ’. Formulae for FF and IFF criteria are shown below.

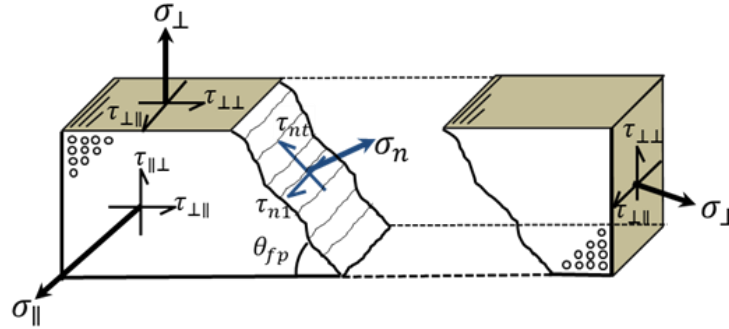


Figure 3.6: Stresses acting on the Fracture Plane

Fiber failure:

Fiber fracture is basically caused by the σ_{\parallel} stressing which acts longitudinal to the direction of the fibers. This stressing may be tensile (Figure 3.7(a)) or compressive (Figure 3.7(b)). These criteria (Eq.(33) and Eq.(34)) was proposed by Puck in 1969 [70]. Y_{\parallel}^t and $-Y_{\parallel}^c$ are tensile and compressive Young’s modulus respectively.

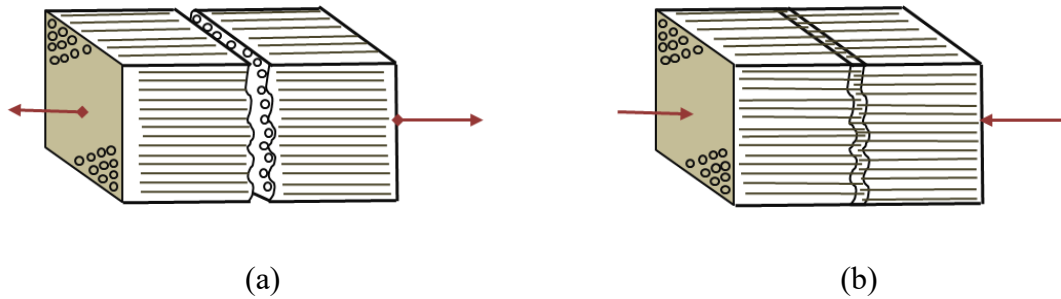


Figure 3.7: (a) Fiber tensile failure, (b) Fiber compressive failure

$$\frac{\sigma_{\parallel t}}{Y_{\parallel}^t} < 1 \quad \text{for } \sigma_{\parallel t} > 0 \text{ for tensile failure} \quad (33)$$

$$\frac{\sigma_{\parallel c}}{-Y_{\parallel}^c} < 1 \quad \text{for } \sigma_{\parallel c} < 0 \text{ for compressive failure} \quad (34)$$

Inter fiber failure:

According to Mohr's fracture hypothesis, IFF is characterized as a macroscopic crack which runs parallel to the fibers and causes separation of the layers. This macroscopic crack is first initiated by the micro-mechanical damage of the matrix or the matrix-fiber structure as a whole. The IFF criteria developed by Puck are based on modified Mohr-oulomb hypothesis and therefore they have to be formulated using the Mohr's Stresses $\sigma_n(\theta_{fp})$, $\tau_{nt}(\theta_{fp})$, $\tau_{n1}(\theta_{fp})$.

As shown in Figure 3.6, σ_{\perp} , $\tau_{\perp\perp}$ and $\tau_{\perp\parallel}$ stresses are mostly responsible for IFF. Hence, their corresponding fracture resistances of the fiber parallel to action plane are denoted as Y_{\perp} , $S_{\perp\perp}$ and $S_{\perp\parallel}$ respectively.

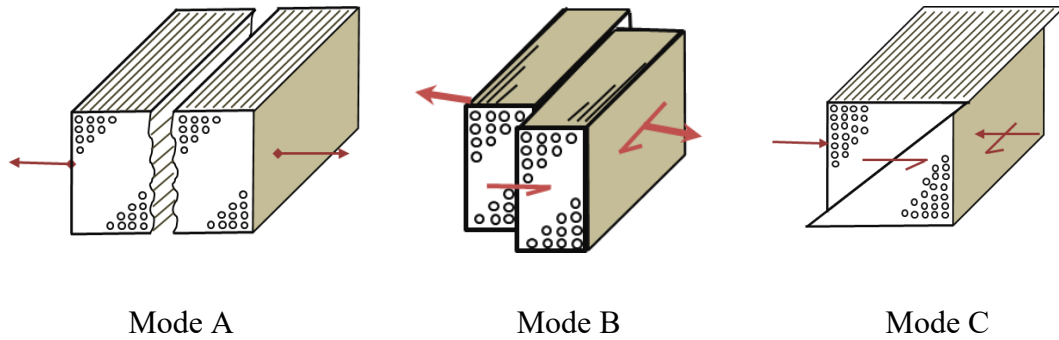


Figure 3.8: Inter-fiber failure modes A, B and C, where mode A and B has a 0-degree fracture plane and Mode C has non zero degree fracture plane

The experimental results of various samples subjected to in-plane loading have given rise to the problem of not knowing the fracture plane for IFF. Three inter-fiber failure modes; *Mode A*, *Mode B* and *Mode C* (Figure 3.8) are distinguished in experimental observations. The occurrence of a specific failure mode is associated with the type and magnitude of loading.

Mode A:

Eq. (35) describes the failure criterion given by Puck for *Mode A*. The occurrence of it is given by application of σ_{\perp} and $\tau_{\perp\parallel}$.

$$0.3 \left(\frac{\sigma_{\perp}}{S_{\perp\parallel}} \right) + \sqrt{\left(1 - 0.3 \left(\frac{Y_{\perp}}{S_{\perp\parallel}} \right) \right) \left(\frac{\sigma_{\perp}}{Y_{\perp}} \right)^2 + \left(\frac{\tau_{\perp\parallel}}{S_{\perp\parallel}} \right)^2} = 1 \text{ for } \sigma_{\perp} \geq 0 \quad (35)$$

Mode B:

Mode B failure occurs purely due to $\tau_{\perp\parallel}$ stressing. Tensile stresses acting on an action plane lead to fracture whereas compressive stresses acting on an action plane prohibits fracture. It means the surfaces are pressed against each other and the crack doesn't open. Hence in cases of combined loading when the axial load acting on the action plane is compressive, τ_{nt} and τ_{nl} have to overcome an extra fracture resistance which is proportional to $|\sigma_n|$. It was seen in the experiments that for $|\sigma_{\perp}| \leq |0.4Y_{\perp}|$ fracture plane was always zero. This set of condition is called as *Mode B* type of failure. Taking this into consideration the shear terms in equations are modified by Puck [71] and given by Eq. (36). The $S_{\perp\parallel,c}$ is ultimate shear strength.

$$0.25 \left(\frac{\sigma_{\perp}}{S_{\perp\parallel}} \right) + \sqrt{\left(\frac{\tau_{\perp\parallel}}{S_{\perp\parallel}} \right)^2 + \left(\frac{0.25\sigma_{\perp}}{S_{\perp\parallel}} \right)^2} = 1 \text{ for } \sigma_{\perp} \leq 0, |\sigma_{\perp}| \leq |0.4Y_{\perp}| \quad (36)$$

Mode C:

It was seen in the experiments that for $|\sigma_{\perp}| \geq |0.4Y_{\perp}|$ the fracture plane was not zero. This mode is called as *Mode C*, which is very difficult to formulate. Puck introduced some parameter based on analytical understanding and experimental observation. He proposed formula for *Mode C* [71]. The failure mode is described in Eq. (37).

$$\left[\left(\frac{\tau_{\perp\parallel}}{2(1+0.22)S_{\perp\parallel}} \right)^2 + \left(\frac{\sigma_{\perp}}{Y_{\perp}} \right)^2 \right] \frac{Y_{\perp}}{(-\sigma_{\perp})} = 1 \text{ for } \sigma_{\perp} \leq 0, |\sigma_{\perp}| \geq |0.4Y_{\perp}| \quad (37)$$

3.3.2.3 LaRC failure criteria

LaRC is a set of three-dimensional failure criteria for determining failure in laminated fiber-reinforced composites. LaRC criteria are consists of six failure modes.

- Two fiber failure modes
- Three matrix failure modes
- One combined mode when fiber and matrix failures occur simultaneously

These failure criteria are basically based on the concepts given by Hashin and the fracture plane theory proposed by Puck. According to the theory of fracture mechanics,

it is proposed that a crack will occur when it is mechanically possible (stress is equal to the failure stress) and energetically favorable (supply of energy is greater than the consumption of energy)[72].

Fiber tensile failure:

The LaRC failure criterion for tensile fiber failure is nothing but a non-interactive maximum allowable stress criterion. This failure criterion can simply be given by Eq.(38).

$$\frac{\sigma_{\parallel}}{Y_{\parallel}} < 1 \text{ for } \sigma_{\parallel} > 0 \quad (38)$$

Fiber compressive failure:

Compressive fiber failure is a field where a lot of research is going on. Depending on the material, different types of compressive fiber failure modes are possible like micro-buckling and kinking. This mode consists of the micro-buckling [73] of the fibers in the elastic matrix.

Kinking can be defined as the localized shear deformation of the matrix, along a band. Once the kink plane is defined then the stresses are rotated to the misalignment frame. The stresses in misalignment frame are computed by using transformation equations. The criteria can be expressed as Eq. (39).

$$\frac{\tau_{1m2m}}{S_{\parallel} - \eta_{\parallel}\sigma_{2m2m}} < 1 \text{ for } \sigma_{2m2m} > 0 \quad (39)$$

Matrix tensile failure

This failure mode occurs when the transverse tensile stress ($\sigma_{\perp} > 0$) is applied. Generally, matrix cracks are expected to initiate from manufacturing defects and can propagate further within planes parallel to the fiber direction and normal to the stacking direction. The criteria can be expressed as Eq. (39)

$$(1 - g) \left(\frac{\sigma_{\perp}}{Y_{\perp}} \right) + g \left(\frac{\sigma_{\perp}}{Y_{\perp}} \right)^2 + \left(\frac{\tau_{\parallel\perp}}{S_{\perp}} \right)^2 < 1 \text{ for } \sigma_{\perp} > 0 \quad (40)$$

Matrix compressive failure

Matrix compressive failures occur by shear stresses. Thus the failure takes place at an angle ‘ α ’ to the plane where the stress is applied. The value of ‘ α ’ has been found out experimentally which is equal to $53 \pm 2^\circ$ for maximum composite materials. The LaRC failure criterion considers that the compressive stress reduces the effective shear stress. Thus, the failure criterion considering both $\tau_{\perp m}$ and $\tau_{\parallel m}$ proposed for matrix compression failure is given in Eq.(41) and equation for matrix failure under biaxial compression is given in Eq.(42)

$$\left(\frac{\tau_{\perp m}}{S_T - \eta_{\perp} \sigma_{nm}}\right)^2 + \left(\frac{\tau_{\parallel m}}{S_L - \eta_{\parallel} \sigma_{nm}}\right)^2 < 1 \text{ for } \sigma_{\perp} < 0, \sigma_{\parallel} < -Y_C \quad (41)$$

Matrix failure under biaxial compression

$$\left(\frac{\tau_{\perp}}{S_{\perp} - \eta_{\perp} \sigma_n}\right)^2 + \left(\frac{\tau_{\parallel}}{S_{\parallel} - \eta_{\parallel} \sigma_n}\right)^2 < 1 \text{ for } \sigma_{\perp} < 0, \sigma_{\parallel} > -Y_C \quad (42)$$

Mixed mode failure

For, $\sigma_{2m2m} \geq 0$ the criterion to determine the matrix tensile failure under longitudinal compression (with eventual fiber kinking) is given Eq.(43)

$$(1 - g) \left(\frac{\sigma_{2m2m}}{Y_{\perp}}\right) + \left(\frac{\sigma_{2m2m}}{Y_{\perp}}\right)^2 + \left(\frac{\sigma_{1m2m}}{S_{\parallel}}\right)^2 < 1 \text{ for } \sigma_{\parallel} < 0, \sigma_{2m2m} > 0 \quad (43)$$

A complete derivation of the LaRC failure criteria is presented in appendix ‘ ‘ . LaRC criteria is more detailed than Puck Tsai-Wu criteria. In house code for each criteria are developed and verified using test samples probes.

Theoretically, it was identified that the LaRC failure criteria with layered solid elements should be most appropriate numerical technique for structural modelling and failure prognostic of composite blades. But to make a benchmark, numerical simulations are performed using all selected failure theories, which are explained before. All results and conclusions are presented in ‘chapter 5’.

3.4 Multi-physics solver coupling

The detailed classification of fluid-structure interaction based on solver coupling techniques is illustrated in Figure 3.9. The different type of coupling approach is discussed in section 2.3. In this section further classification of partitioned conforming mesh approach is discussed briefly. In the uni-directional partitioned approach, a converged solution of one field is used as boundary condition for second field for once, which is suitable for weak physical coupling. In the bi-directional partitioned approach a converged solution of first field is used as boundary condition for second field and the converged solution of the second field is used as a boundary condition for the first field for one time step as shown in Figure 3.10.

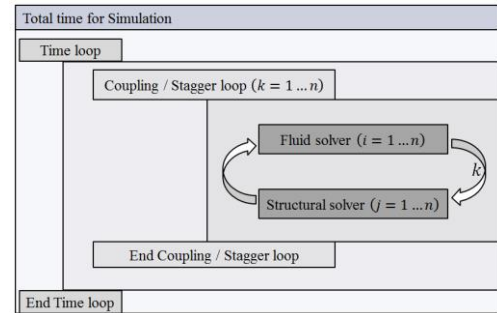
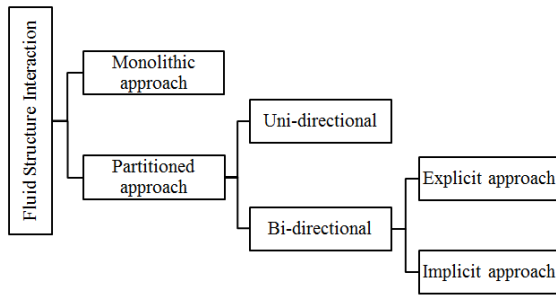


Figure 3.9: Detailed classification of the approaches adopted to handle FSI

Figure 3.10: Schematic view of algorithm used for bi-directional FSI

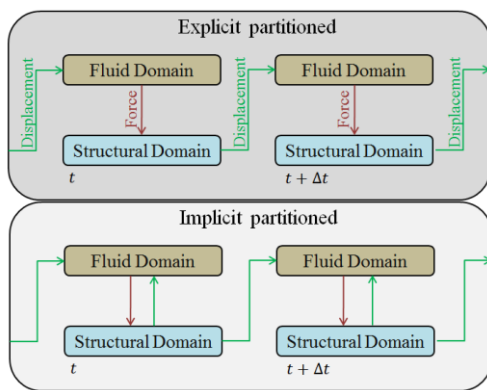


Figure 3.11: Data communication between fluid and structural domain for explicit and implicit partitioned approach

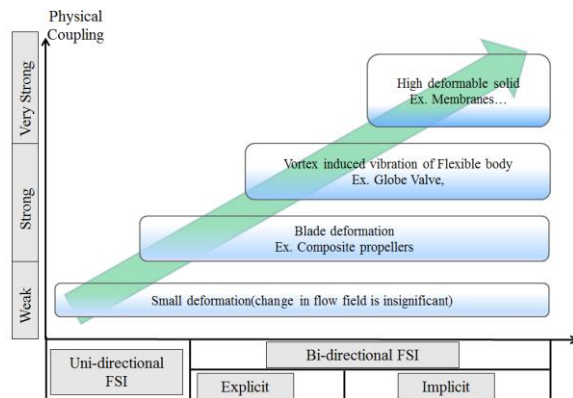


Figure 3.12: Plot depicting the level of physical coupling versus numerical coupling for different applications [74]

If the number of stagger loop is defined to one then it is called as explicit partitioned approach otherwise it is called as implicit partitioned approach (Figure 3.11). But, multiple small time steps are needed for explicit approach to reach the final converged

solution of both domains. Figure 3.12 shows about the type of physical coupling and FSI approaches are needed for given applications. The physical coupling of composite blades with a water domain is considered as strong coupling so implicit bi-directional numerical coupling methodology is used for simulations. In this thesis, the implicit bi-directional partitioned conforming-mesh approach is used for stable fluid-structure interaction simulation. The uni-directional approach is also used and compared to bi-directional approach.

3.4.1 Governing equations

FSI problems are actually a two field problem. Therefore, its mathematical description includes the governing equations of the fluid and structural parts, which are explained in section 3.1 and section 3.2. Displacement and pressure load data are exchanged between structural solver and fluid solver by using mapping algorithm.

3.4.2 Mapping

Mapping plays a key role for the correct data transfer between two domains. For mapping, a general grid interface mapping technique is used [74]. Element sectors from both sides are projected onto a control surface as shown in Figure 3.13. Flows from the source side are projected and split between the control surfaces. Furthermore, flows from control surface are gathered and sent to target side. If the mesh is same both sides, the mapping can reach an accuracy of 100 percent.

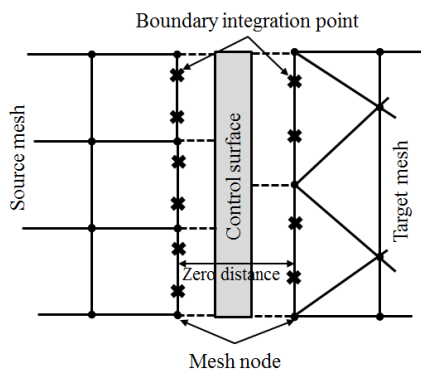


Figure 3.13: General grid interface mapping algorithm [74]

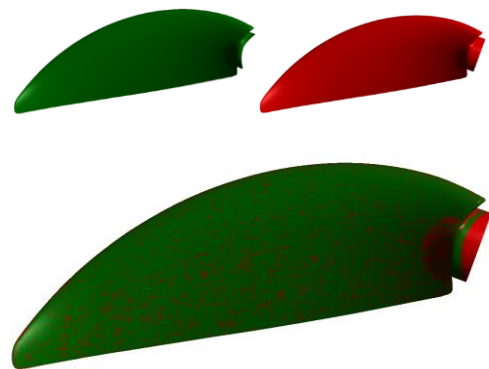


Figure 3.14: Green surface from fluid domain and red surface from structural domain are perfectly matching for accurate data transfer

3.4.3 Smoothing

In the conforming mesh approach, the mesh deformation in fluid domain must be handle accurately without disturbing boundary layer mesh. For the current research, the small mesh deformation is handle by spring based smoothing technique. In this method, edges between two mesh node are considered as interconnected springs, where k_{ij} is the spring constant between two nodes i and j as shown in Eq.(44).

$$k_{ij} = \frac{K_{input}}{\sqrt{|\vec{x}_i - \vec{x}_j|}} \quad (44)$$

$$\vec{F}_i = \sum_j^{n_i} k_{ij} (\Delta\vec{x}_j - \Delta\vec{x}_i) \quad (45)$$

$$\Delta\vec{x}_i^{m+1} = \frac{\sum_j^{n_i} k_{ij} \Delta\vec{x}_j^m}{\sum_j^{n_i} k_{ij}} \quad (46)$$

$$\frac{\Delta x_{rms}^m}{\Delta x_{rms}^1} < \text{Convergence tolerance} \quad (47)$$

$$\vec{x}_i^{n+1} = \vec{x}_i^n + \Delta\vec{x}_i^{converged} \quad (48)$$

An initial spacing is considered as the equilibrium state of the mesh created. The boundary nodes displacement generate forces based on Eq.(45) and, after that the adjacent nodes are displaced so that the net force on boundary nodes becomes zero. The same procedure is extended for all fluid domain nodes. This condition results an iterative equation as shown in Eq.(46), which is controlled by manually defined convergence tolerance (Eq.(47)). After calculating all displacements node positions are updated for next time step (Eq.(48)).

3.4.4 Re-meshing

The smoothing technique works for small deformations of the boundary but while smoothing the element quality deteriorates. It is highly possible that at large deformation, smoothing could lead to bad element quality like negative volume and many more, which cause convergence error during simulations. To resolve this issue, re-meshing is used

based on element skewness and size. The mesh with bad elements is locally eliminated and filled with new elements with better quality. The solution for new elements is interpolated from the previous element solutions. Smoothing with re-meshing facilitate to simulate fluid-structure interaction involving large deformation. Mesh smoothing and re-meshing is achieved using commercially available ANSYS Fluent solver.

In this section, mathematical modelling and process algorithms for fluid-structure interaction are explained in detail. In next section, a mixer propeller blade made of layered composite and a tidal-turbine blade made of random-oriented carbon-fiber reinforced composites are selected for the application of knowledge. For the selected propeller and turbine blade, an extensive flow simulation, structural simulations and FSI are performed. Furthermore the feasibility, robustness, accuracy of the calculations and the ease of application are discussed later.

4 Flow simulation

4.1 Domain and grid modelling

The two blade submersible mixer selected for the numerical simulation has a diameter of 2.6 m as shown in Figure 4.1. Rotating speed of blade is defined at 46 RPM. The Reynolds number of this mixer is $5.2e^6$. So, the flow around blade is turbulent. Blades are made of glass fiber-reinforced layered composites. To reduce the complexity of CAD geometry for meshing, the hub is simplified into solid cylinder. Similar to the mixer, the four blade tidal-turbine used for flow simulation has a diameter 4 m, which rotates at 60 RPM (Figure 4.2). The Reynolds number of the tidal-turbine is $1.8e^7$.



Figure 4.1: CAD model of the mixer blade provided by WILO SE



Figure 4.2: CAD model of the tidal-turbine blade provided by SCHOTTEL GmbH

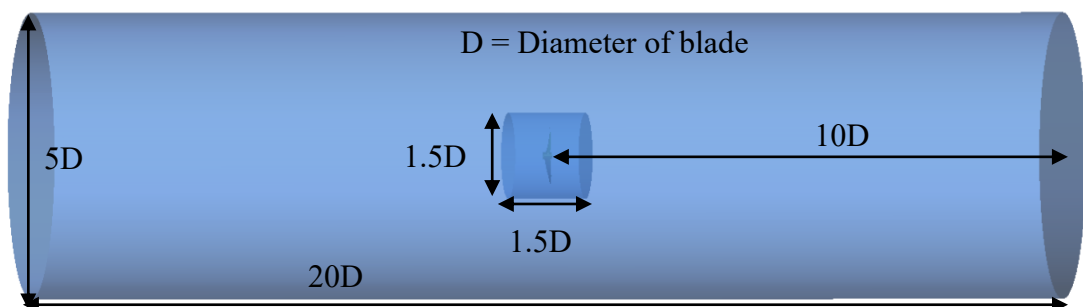


Figure 4.3: Dimensions of rotor and stator domains created for simulations

The state of the art for CFD analysis of rotating machines is to define rotor and stator domains. So, domains are designed in cylindrical form to capture all possible hydraulic

effects. The length and diameter of the rotor domain are defined 1.5 times of the diameter of the rotating machine. Furthermore, the length and diameter of stator domain are 20 times and 5 times of the diameter of the rotating machine respectively. The guidelines for domain dimensions has been taken from the best-practice guide for the mixer simulations, created by ASYS-CFX Berlin [75]. Dimension of the domains are shown in Figure 4.3.

Rotor Domain for the Mixer:

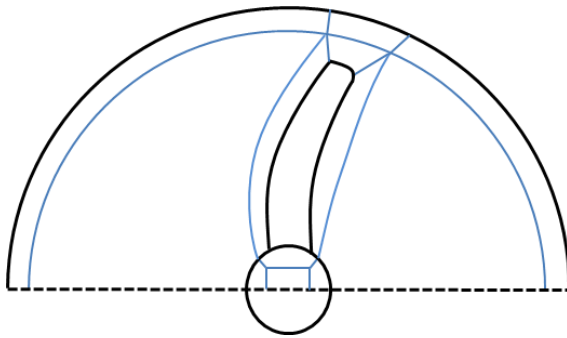


Figure 4.4: Block around the blade in axial direction of the rotor domain

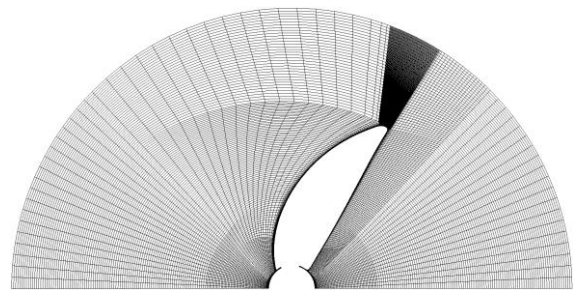


Figure 4.5: Hex-grid in axial direction of rotor the domain

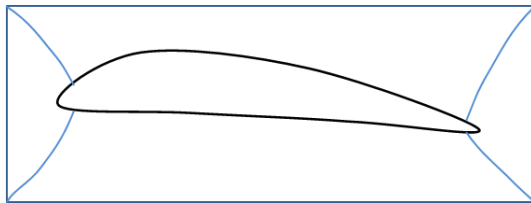


Figure 4.6: O-block around the blade

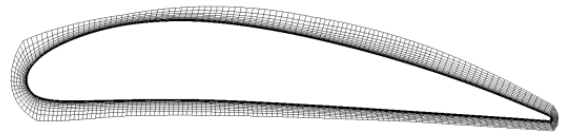


Figure 4.7: Hex-grid around the blade

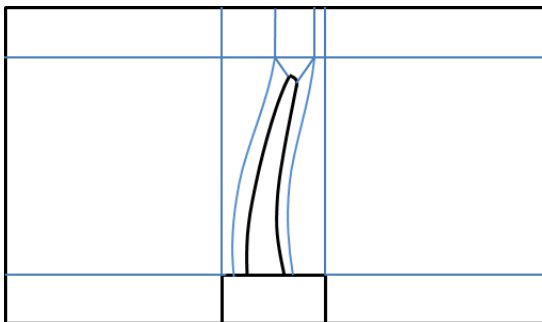


Figure 4.8: Block in transverse direction of the rotor domain

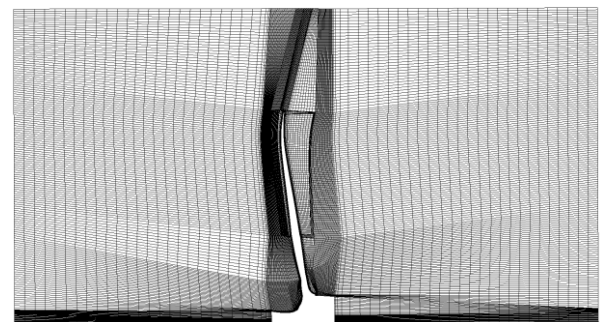


Figure 4.9: Hex-grid in transverse direction of the rotor domain

High quality mesh is very important for the convergence of a simulation and the accuracy of calculation. A quality parameter is maintained for the meshing of the stator and rotor domain as defined in Table 4.1. For the analysis of mixer a high quality hex grid mesh is generated in ICEM meshing software by using block structured approach.

Block structures for mixers are shown from Figure 4.4 to Figure 4.13. The 3D mesh topology for the fluid domain of the mixer is presented in Figure 4.14. To reduce computational efforts for simulations, the symmetry is considered about diameter of fluid domain and the half fluid domain (with one blade) is simulated as shown in Figure 4.14.

Stator domain for the Mixer:

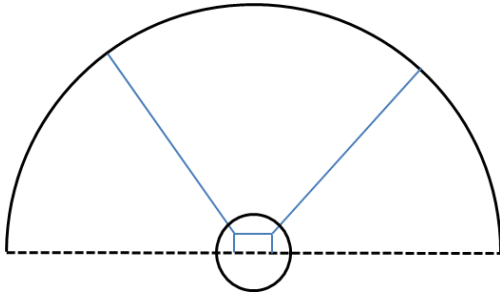


Figure 4.10: Block created for the stator domain in axial direction

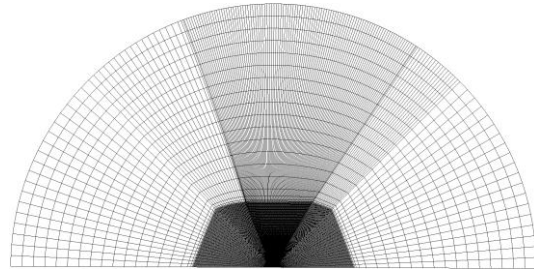


Figure 4.11: Hex-grid created for the stator domain in axial direction

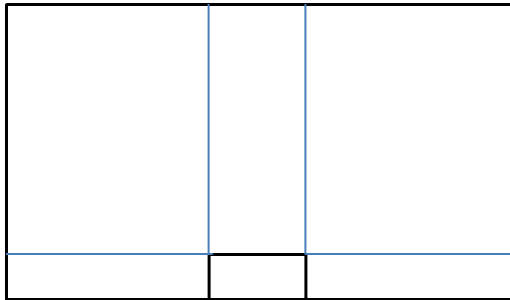


Figure 4.12: Block created for stator domain in transverse direction

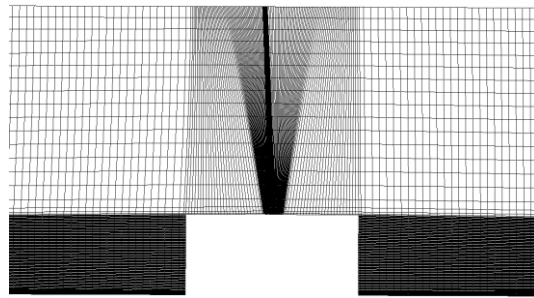


Figure 4.13: Hex-grid created for stator domain in transverse direction

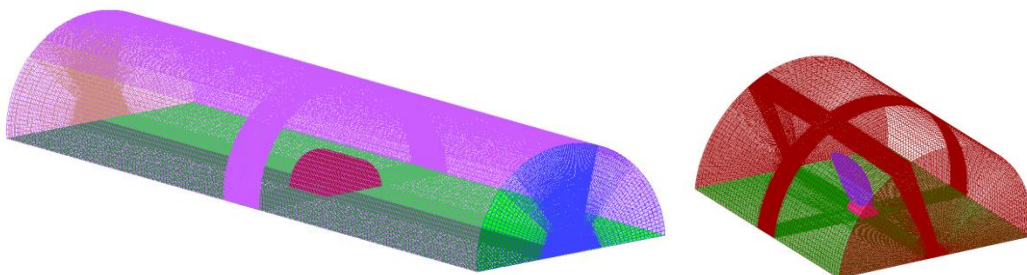


Figure 4.14: Complete 3D mesh topology of rotor and stator domain for the mixer simulations

Table 4.1: Element quality parameters maintained while creating the hex mesh for fluid domain

Quality parameter	Value
Minimum angle	>27 degree
Minimum Determinant(3x3x3)	>0.3
Minimum volume	>0.001 (all positive)
Maximum Y-Plus	1-2

The total number of elements and nodes are $1.62e^7$ and $1.58e^7$ respectively for the mixer blades. The total number of elements and nodes are $6.1e^6$ and $6.2e^6$ respectively for turbine blades. Mesh of rotor and stator domain are connected to each other node by node such that interfaces are able to balance physical fluxes in the best manner. Due to repetition of similar information, the block structure for the turbine is not presented here but 3D mesh topology is presented in Figure 4.15 for better understanding.

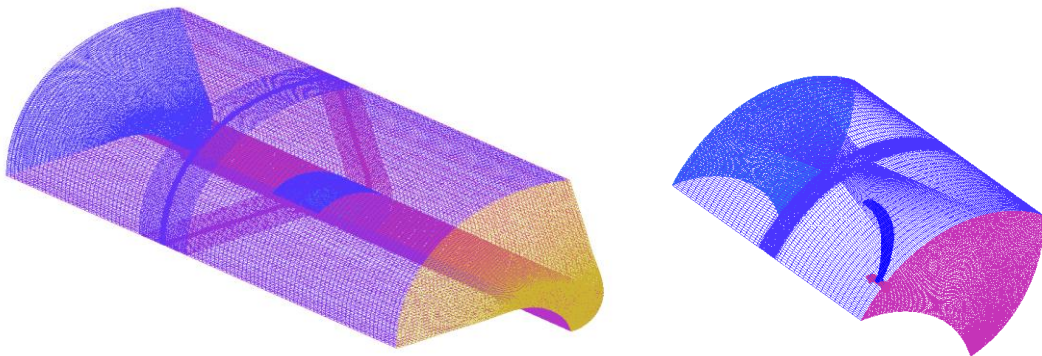


Figure 4.15: Complete 3D mesh topology created for rotor and stator domain of the tidal-turbine for its simulation

4.2 Boundary conditions

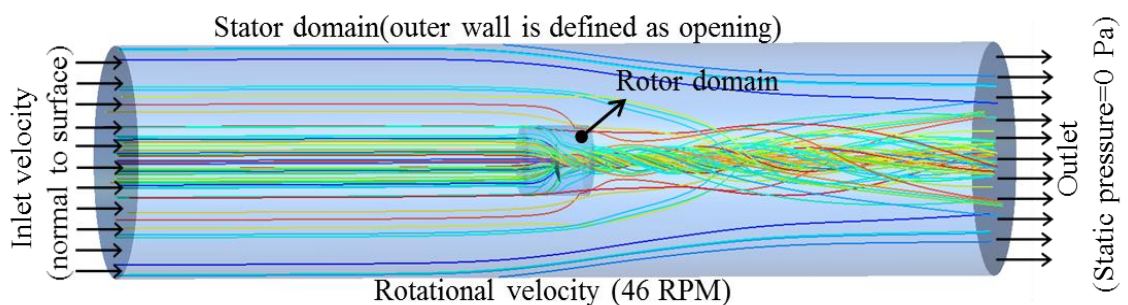


Figure 4.16: Boundary conditions defined for the simulations

A number of CFD simulations are performed to calculate power, torque and thrust with various turbulence models and inlet velocities. The boundary conditions must be correct and similar to the real application for reliable results from CFD calculations. The velocity is defined normal to the surface at the inlet and, zero static pressure is defined at the outlet as shown in Figure 4.16 .

Boundary conditions for turbulence model verification

As a first step, various frequently used turbulence model are defined to calculate torque and thrust in order to find out most accurate numerical settings for the mixer simulations. All turbulence model used for calculations are shown in Table 4.2.

Table 4.2: Turbulence model used for simulation to find accurate numerical model for future FSI calculations

Inlet velocity [m/s]	Rotational speed [RPM]	Turbulence model setup
0.05	46	k - ϵ steady state
0.05	46	k - ω steady state
0.05	46	SST steady state
0.05	46	SST with Gamma-Theta transition model- Steady state

Parameter variation

As a second step different inlet velocity are used to calculate torque and thrust at the selected appropriate turbulence settings as presented in Table 4.3. This step is done to create torque and thrust curve versus inlet velocities.

Table 4.3: Variation in inlet velocity to find thrust and torque behavior versus inlet velocity

Inlet velocity [m/s]	Rotational speed [RPM]
0.05	46
0.1	46
0.15	46
0.2	46
0.5	46
1	46

Similar to the mixer propeller, the torque, thrust and power curve are created for different velocity using appropriate numerical setup for the tidal-turbine. Table 4.4 shows boundary conditions used for the tidal-turbine simulations.

Table 4.4: Boundary conditions used to simulate the tidal-turbine to find torque, thrust and power characteristic

Inlet velocity [m/s]	Rotational speed [RPM]	Tip-speed ratio[-]
1	60	12.5
1.25	60	10
2.50	60	5
5	60	2.5

4.3 Simulation results

The simulation results are used to determine pressure on blade surface, which helps to calculate the power, thrust and torque. Initially, an analysis of flow behind the mixer blade is performed and later the simulation results of the turbine blade is discussed. Convergence limits for all simulations has been defined to 0.0001 and 0.001 for RMS and Max residuals respectively. The formulation of thrust and torque are shown in Eq.(49) and Eq.(50) respectively. The actual power of the water mixer is calculated on basis of the number of blades, rotational speed and torque as shown in Eq.(51). Three dimensional streamline flow for mixer observed in numerical simulation is presented in Figure 4.17.

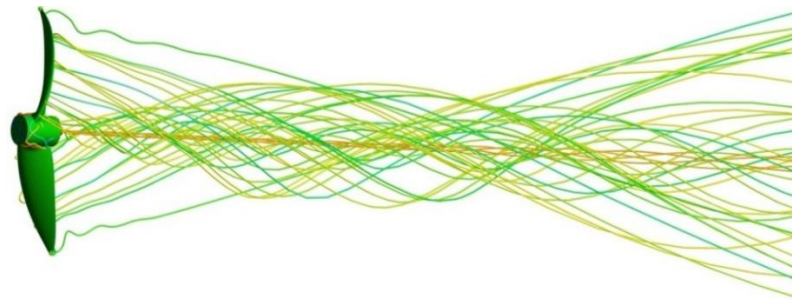


Figure 4.17: Three-dimensional streamline flow behind mixer

4.3.1 Turbulence model: Comparison and selection

The mixer system was installed in an open pond for the experimental analysis by company partners. The static thrust is measured in the normal water of the pond. This situation is considered as zero inlet velocity for the mixer. Experimentally measured values of thrust and torque are 4380 N and 850 Nm respectively[14]. After that, turbulence models (as described in boundary conditions) are used to calculate the integral values of thrust and torque at 0.05 m/s inflow velocity. The convergence of numerical simulations at zero inlet velocity was hard to reach. Moreover, it violates the continuity and mass conservation. At zero velocity back flow over the blade was dominating (to

maintain mass conservation) and it was changing the thrust and torque values a lot. So, lowest inlet velocity of 0.05 m/s is used to simulate and calculate integral values. Additionally simulations are performed at 0.1 m/s and 0.15 m/s inflow velocity. Using three point data, thrust and torque values are extrapolated to estimate these integral values at 0.0 m/s and then the estimated values are compared to the experimental values as shown in Figure 4.18 and Figure 4.19. The $k-\varepsilon$ turbulence model has maximum deviation and SST turbulence model with Gamma-Theta transition model has minimum deviation from the experimental data.

$$Thrust = \int Force_{rotation\ axis}@blade\ area \quad (49)$$

$$Torque = \int r \times Force@blade\ area \quad (50)$$

$$Power = N_b * \omega_o * Torque \quad (51)$$

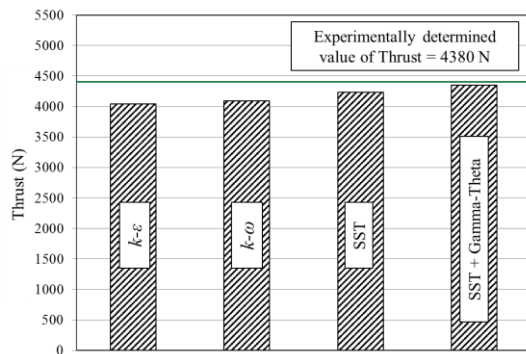


Figure 4.18: Column chart to compare thrust value calculated by using various turbulence model

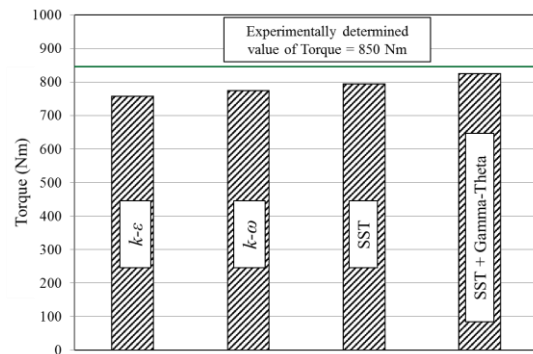


Figure 4.19: Column chart to compare torque value calculated by using various turbulence model

The gradient diffusion hypothesis is used by $k-\varepsilon$ model to relate Reynolds stresses to the mean velocity gradients and the turbulent viscosity. So, it performs poorly for flow involving strong streamline curvature and severe pressure gradient. As a consequence, it is calculating high turbulence kinetic energy at leading edge (Figure 4.20(a)). The $k-\omega$ model is more accurate near wall because of automatic switch from wall function to low-Reynolds number formulation based on grid spacing [59]. This model does not employ damping function so transition is typically predicted early (Figure 4.20(b)). The SST model behave like standard $k-\omega$ model so flow around blade is same for both turbulence

model (Figure 4.20(c)). The SST model with Gamma-Theta transition model is not showing high turbulent kinetic energy at leading edge. Moreover it is predicting transition later on the blade surface as shown in Figure 4.20(d).

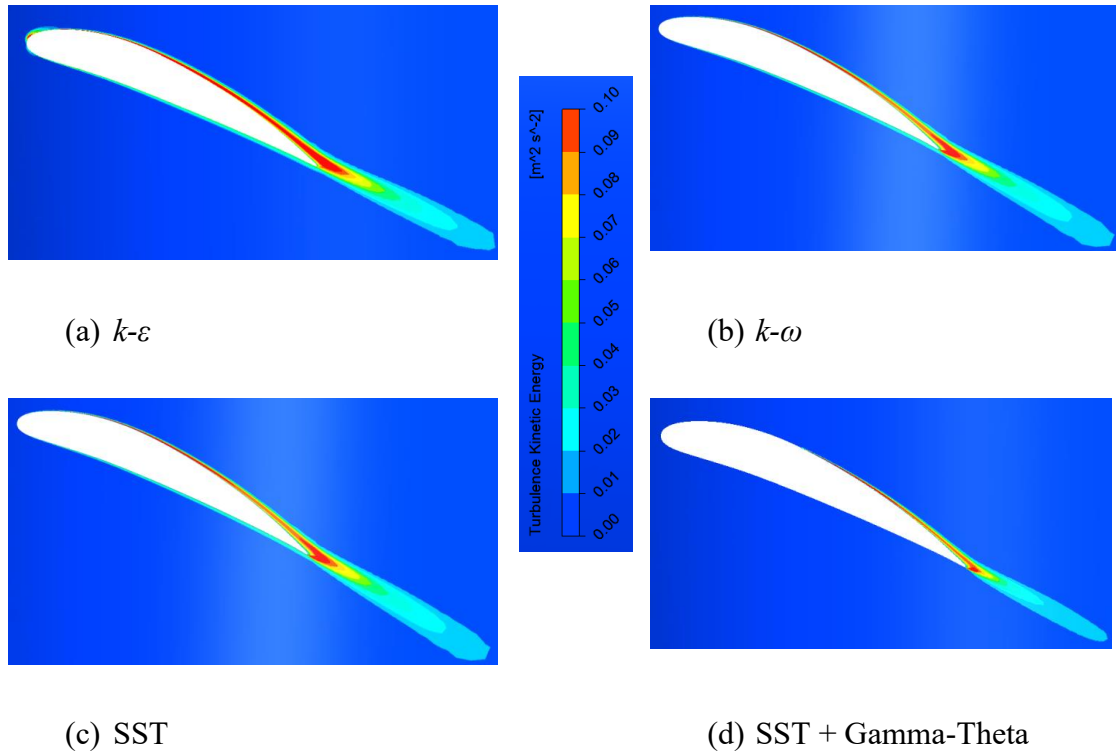


Figure 4.20: Contour of turbulent kinetic energy for various turbulence model and settings at $0.5 \cdot R$ of blade

Furthermore, to justify the selection of SST with Gamma-Theta transition model as a bench mark for the future CFD calculation of the mixers, the relative percentage of laminar flow is calculated over the blade using an empirical formula proposed by Mayle (1991) [76] as shown in Eq. (53). The relative percentage of laminar flow on the blade is 0.42. It means the assumption of fully turbulent flow is not correct and the Gamma-Theta model is a better model for the setup of mixers to predict the flow field and transition. Because this model has two more equations, one for intermittency and other for transition momentum thickness Reynolds number as explained in section 3.1.3.

The Gamma-Theta transition model is used to determine the point of transition using turbulent intensity, which is calculated using the turbulence kinetic energy and the velocity. A point where turbulence intensity exceeds 10 percent is considered as the point of transition, as shown in Figure 4.21. Based on the theoretical understanding, CFD

results and experimental data, SST turbulence model with Gamma-Theta turbulence model is selected for all future CFD and FSI calculations.

$$Tu = \frac{(2k/3)^{0.5}}{V} \quad (52)$$

$$\frac{Re_{xt}}{Re_x} = \frac{380000 * (100 * ((2k/3)^{0.5}/V))^{-5/4}}{(\rho/\mu) * V * L_{chordlength}} \quad (53)$$

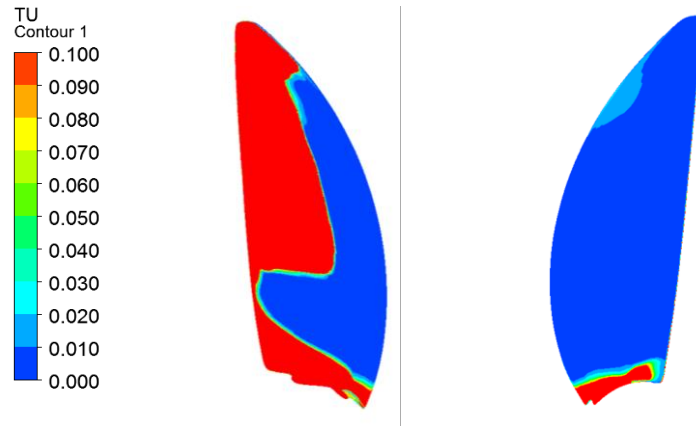


Figure 4.21: Contour showing transition from laminar (blue) to turbulent flow (red) over the blade. Transition is considered if turbulent intensity (TU) goes more than 0.10.

4.3.2 Torque and thrust characteristics

Thrust and torque versus inlet velocity curves are plotted in Figure 4.22 and Figure 4.23 for SST turbulence with Gamma-Theta transition models. These curves are extrapolated up to zero inlet velocity. Thrust and torque increase with decreasing inlet velocity. It can be noticed that slope of thrust and torque curve at lower velocity is very less. It means thrust and torque are not changing very much at lower velocities.

Based on thrust and torque characteristics, it is identified that pressure load at 0.05 m/s inflow velocity can be transferred for FSI simulation because thrust is not changing much at lower velocities. Moreover, no simulation data is available for velocity lesser than 0.05 m/s.

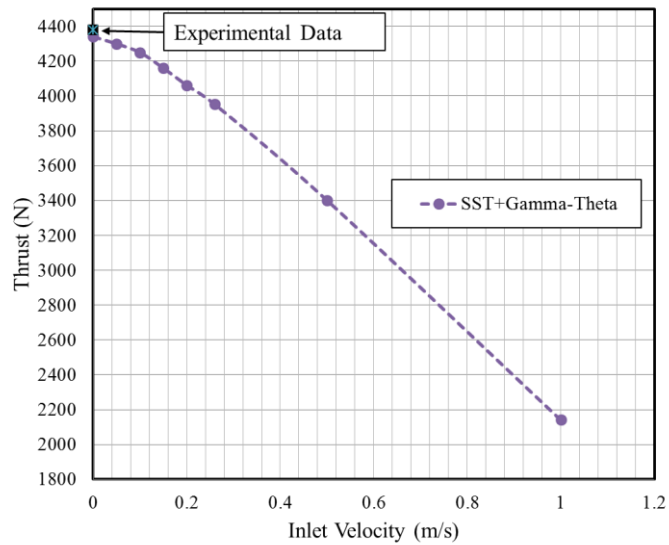


Figure 4.22: Plot of Thrust versus inlet velocity for the mixer using SST turbulence model with Gamma-Theta transition model for the simulation. Experimentally observed thrust is plotted as a single bullet point too.

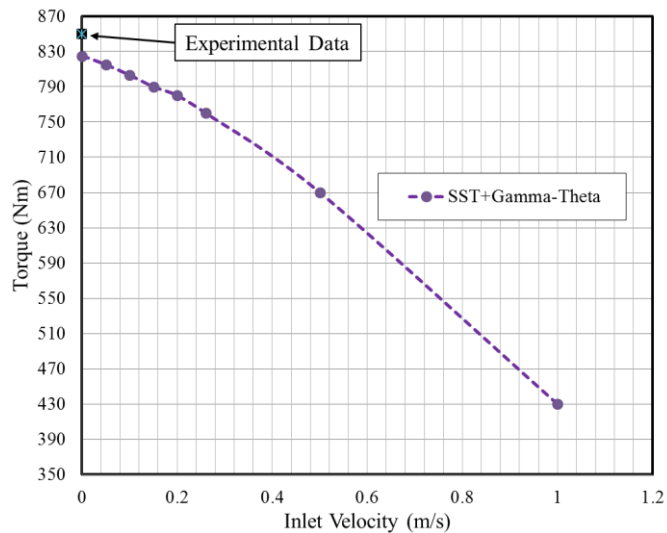


Figure 4.23: Plot of Torque versus inlet velocity for the mixer using SST turbulence model with Gamma-Theta transition model for the simulation. Experimentally observed torque is plotted as a single bullet point too.

Integral value of thrust and torque also affected by an aerodynamic design of the blade. Blade loading is one of the key plots in order to understand hydrodynamic loads on the blade. It tells the pressure distribution over the suction and pressure side of the blade. The blade loading is shown in Figure 4.24. Contour for the pressure distribution on the suction side and pressure side are shown in Figure 4.25. The static pressure distribution on the blade is transferred from CFD solver to structural solver for fluid-structure interaction simulation.

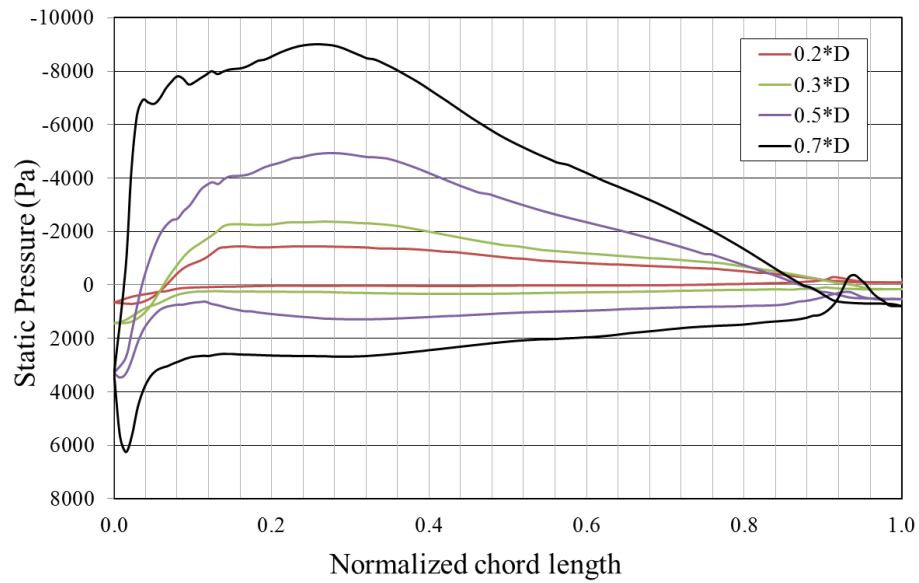


Figure 4.24: Blade loading plot for mixer propeller at 0.05 m/s inlet velocity and 46 RPM

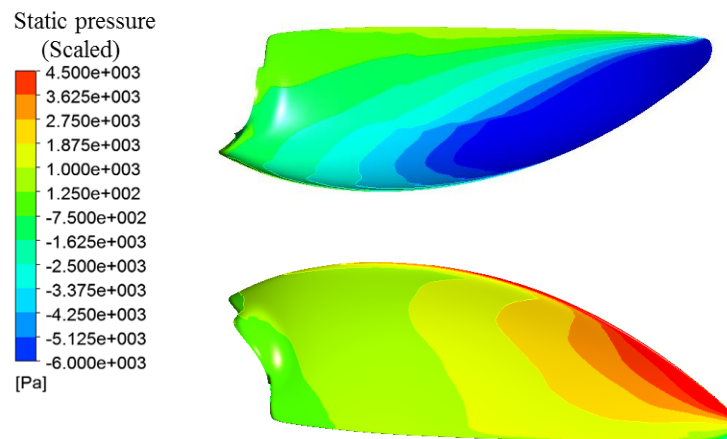


Figure 4.25: Contour for static pressure over blade surface at 0.05 m/s inflow velocity. Suction side (up) and Pressure side (down)

The selection of turbulence model setting and boundary condition are selected for future FSI calculation. But it is important to see that the flow behavior at selected numerical setup is matching to theoretical understanding of the flow field behind the mixer propeller.

At low velocity, mixer blade may generates back flow behind the blade to maintain the mass conservation and continuity. This flow field is not correct for true estimation of thrust and torque on blade. But on other hand, simulation at lower velocity is mandatory for the calculation of maximum thrust experienced by blades at given speed. In current

research work, simulation are performed at low velocities but it is important to verify that flow field behind the mixer blade is correct or not as per theoretical understating turbulent jet flow field.

4.3.3 Velocity profile: Jet turbulent flow

The schematic flow field behind a mixer is plotted in Figure 4.26. The mixer develops axial, circumferential and radial flow velocities behind the blade. Furthermore, the flow behind mixer can be divided into entrainment, expansion and hub delay zones. It can be observed that axial and circumferential velocities decreases with increasing distance from the mixer because of dissipation.

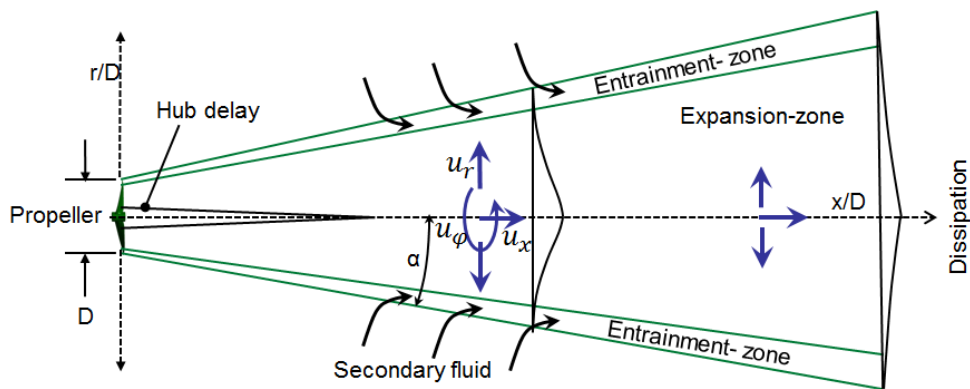


Figure 4.26: Schematic swirl flow behind the propeller, where u_x , u_r and u_ϕ are axial, radial and circumferential velocity [16]

The axial and circumferential velocities over the plane normal to the axial direction at different axial distances from the mixer are plotted in Figure 4.27. The shape of the velocity profile changes with the axial distance from the mixer as shown in Figure 4.28(a). The axial velocity on the axis line is low because of the hub delay phenomena. Thus it could be concluded that the CFD numerical setup is able to correctly reproduce the jet turbulent flow behind the mixer as per the theoretical background.

Moreover, it can be observed from Figure 4.28(a) that axial and circumferential velocities decrease with distance from the mixer because of dissipation and both velocities become constant far from the mixer. The decrease in velocity is not uniform. The tip vortex generated by the blade are shown in Figure 4.28(b) which is plotted using *the lambda-2* criteria proposed by Jeong and Hussain [77]. The tip could be modified to

improve the efficiency of the blade by reducing the tip vortex as proposed by Kumar et al. (2012) [23].

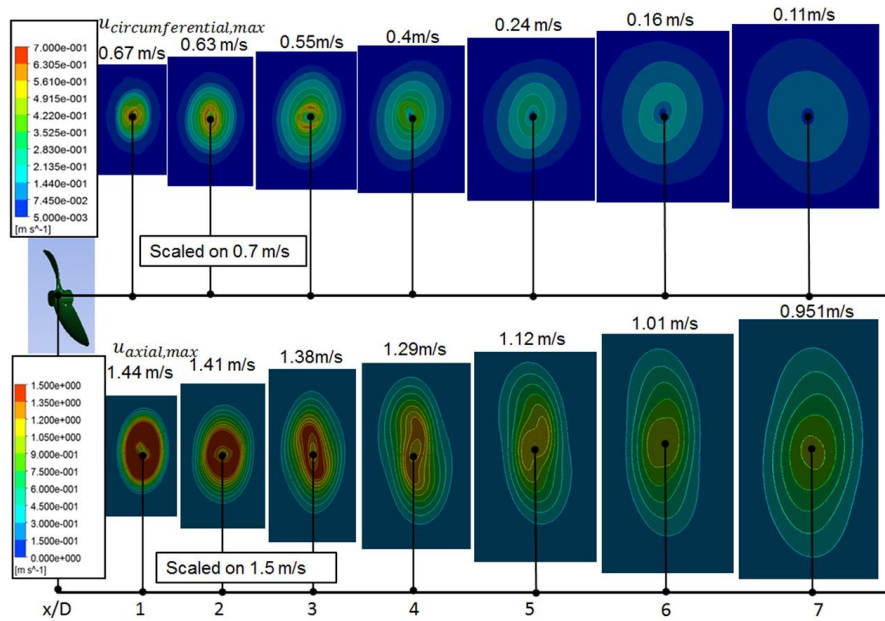
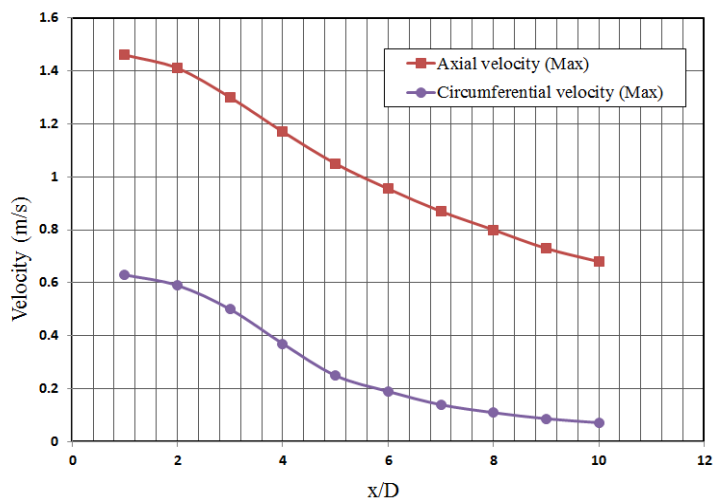


Figure 4.27: Contour of Axial and circumferential velocity at different axial position from mixer



(a)



(b)

Figure 4.28: (a) Maximum axial and circumferential velocity at different axial distance from the propeller, (b) Tip vortex solved in simulation

It can be accepted that current CFD numerical model calculated correct flow field thrust and torque for the mixer propeller blade. So, this numerical model is used for FSI simulations. Similar simulations are done for the tidal-turbine. CFD simulation results of turbine blade are presented in next section of this chapter.

4.3.4 Flow, thrust and power characteristic of the tidal-turbine

Flow behind the turbine behaves similar to the flow behind the mixer as shown in Figure 4.29. It has axial, circumferential and radial velocities but the axial velocity in the expansion zone is smaller than inlet velocity as plotted in Figure 4.30. This means energy is extracted from the flowing liquid, which is the typical behavior of the flow behind the turbine. The circumferential velocity is generated by the rotation of turbine blades.



Figure 4.29: 3D Streamline plot of flow behind the tidal-turbine

The simulations are performed for 1, 1.25, 2.5 and 5 m/s inlet velocity at constant rotational speed of the blade. Contrary to the mixer blades, thrust and torque increases linearly with increasing inlet velocities (Figure 4.31).

The tip-speed ratio is defined as ratio of circumferential velocity to inlet velocity (Eq. (54)). Average velocity of water in tidal current is around 2.5 m/s. This particular blade is designed to extract maximum power at 2.5 m/s velocity [78]. The tip-speed ratio is equal to 5 at 2.5 m/s velocity for 2 m blade radius. The maximum power is calculated using Betz's law [79] as shown in Eq.(55). The coefficient of power is calculated by using Eq. (57) and plotted in Figure 4.32(a). The numerical simulation shows that maximum power is extracted at 2.5 m/s inlet velocity with 60 RPM rotational speed. At a tip-speed ratio equal to 5, the coefficient of power is near to 0.485.

$$\lambda = \frac{\omega_o * r}{v} \quad (54)$$

$$Power_{max} = 0.5 * \rho * \pi * r^2 * v^3 \quad (55)$$

$$Power_{turbine} = N_b * \omega_o * Torque \quad (56)$$

$$C_{PR} = \frac{Power_{turbine}}{Power_{max}} \quad (57)$$

$$C_{MR} = C_{PR} / \lambda \quad (58)$$

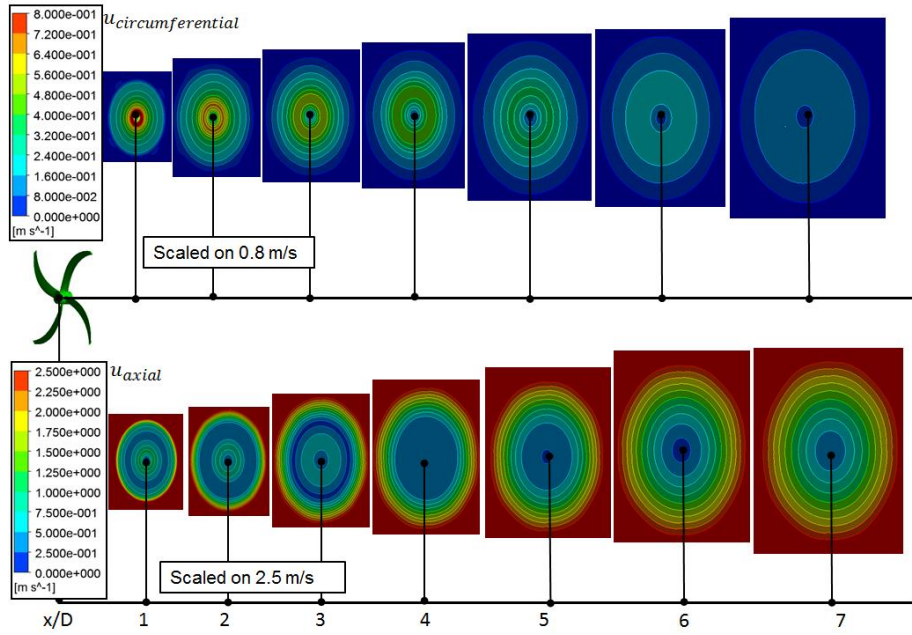


Figure 4.30: Contour of axial and circumferential velocity at different axial distance from tidal-turbine

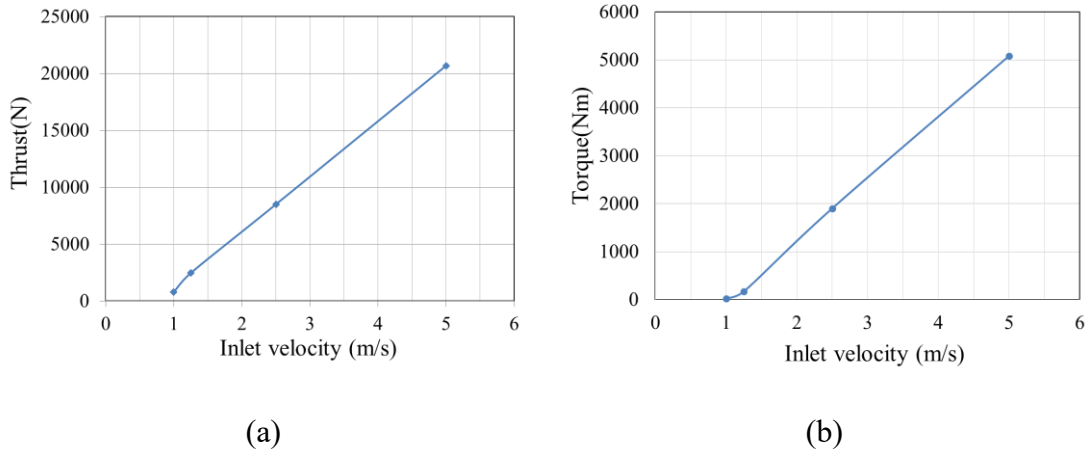


Figure 4.31: Plot for (a) Thrust and (b) Torque versus inlet velocity for the one blade of tidal-turbine

Torque is required to start the rotation of the blade. The formulations of torque and thrust are same, which are used for the mixers propeller blades. The coefficient of torque or moment is defined in Eq. (58). The complete results for all inlet velocities are presented in Table 4.5.

Table 4.5: Integral values of torque on blade, power available in the water, power extracted by the one blade and the coefficient of power & torque verses inlet velocity of the water

Velocity [m/s]	Omega [RPM]	Tip-speed ratio [-]	Torque [Nm]	$Power_{max}$ [W]	$Power_{turbine}$ [W]	C_{PR} [-]	C_{MR} [-]
1.00	60	12.5	21	6283.0	63.0	0.01	0.008
1.25	60	10.0	170	12271.5	4250.0	0.34	0.034
2.50	60	5.0	1903	98171.8	47575.0	0.485	0.097
5.00	60	2.5	5083	783375.0	127075.0	0.162	0.065

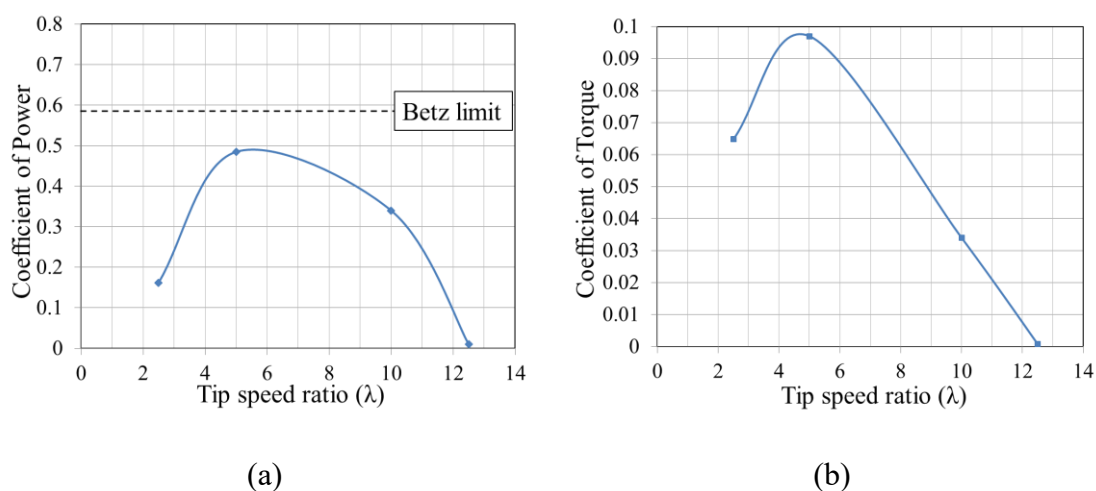


Figure 4.32: (a) Plot for the coefficient of power extracted by the turbine verses tip-speed ratio, (b) Plot for coefficient of torque taken by turbine versus tip-speed ratio

It is observed that the highest value for the coefficient of torque is around 0.1 at the tip-speed ratio of five (Figure 4.32 (b)). At 1 m/s inlet velocity torque is very small so that it cannot start the rotation of the blade (Table 4.5). Different velocities are generating different pressure distributions around the blade as shown in Figure 4.33. A high pressure difference is created around the blade at a high inlet velocity which leads to a high thrust on the blade. A high thrust leads to high deformation of the blade.

High deformations may lead to fracture of the body and instant failure of the system. Moreover, it could change the pitch angle of the blade which cause a significant reduction in the power generation. To see real deformation of the blade fluid-structure interaction simulations become very important. But before going into FSI, structural model must be created and verified for composite material. Extensive study for structure modelling is done and presented in next chapter.

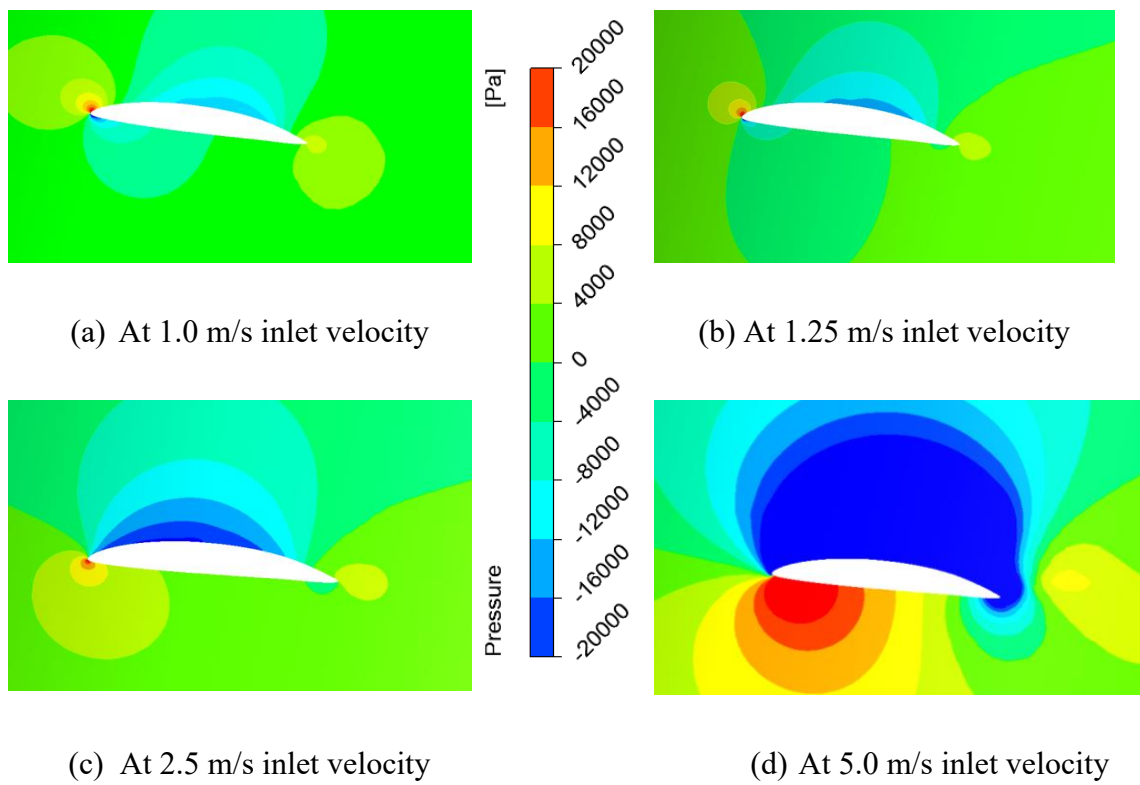


Figure 4.33: Contour plot of static pressure distribution around blade at $0.5 \cdot R$ for different inlet velocity

5 Structural simulation

The mixer propeller selected for this project has blades with multiple composite layers. To analyze these blades, it is extremely important to know their manufacturing process and material properties in detail. Moreover, the material modelling must be defined for each single layer and it should be validated experimentally. The process for an extensive structural analysis is shown in Figure 5.1. This process is followed to create a structural model for fluid-structure interaction analysis.

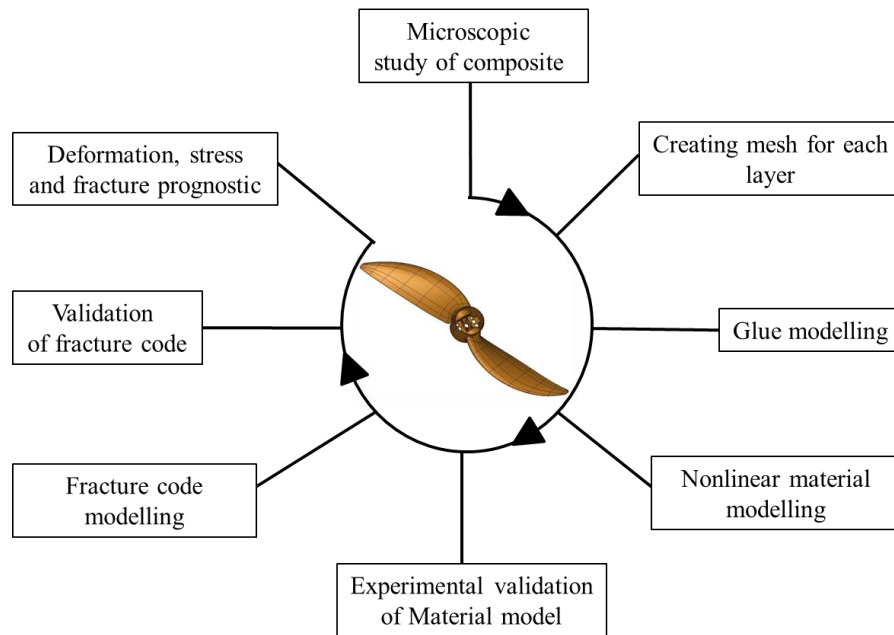


Figure 5.1: Steps followed to perform a structural analysis for a layered composite

5.1 Microscopic study of the blade

A microscopic study of the blade is first step to create a detailed structural model for analysis. Various specimens from different section of the original blade are cut out to see the composition of the blade (Figure 5.2). A high resolution microscope measurement technique is used to measure the thickness of each layer as shown in Figure 5.3. Each layer is pasted over another layer using glue and a gel coat is plated on the top of blade

to give its surface finish. The inside volume is filled with polyurethane foam. Thickness, material property and orientation of fiber for each layer are presented in Table 5.1.

Table 5.1: Material properties for each layer of composite laminate used to manufacture the mixer blade

	Thickness	Material	Orientation
Gel coat	0.42mm	Polyester resin	Uniform
Layer1	0.80mm	Glass fibers	Random
Layer2	0.84mm	Glass fibers	± 45 degree
Layer3	0.80mm	Glass fibers	Random
Layer4	0.84mm	Glass fibers	± 45 degree

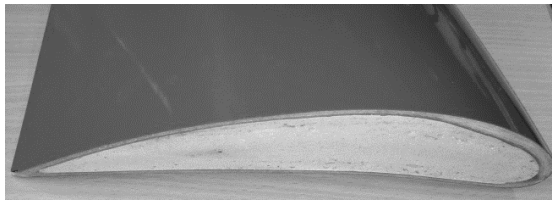


Figure 5.2: Specimen cut from the original blade to see a layer orientation. The blades was provided by WILO SE, Research and Development Center, Dortmund, Germany [14].

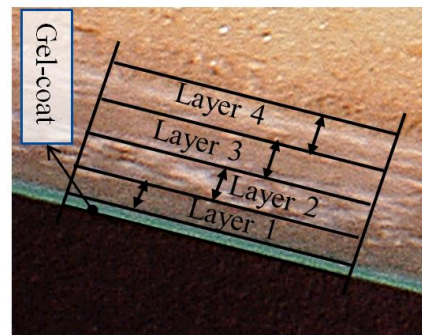


Figure 5.3: Microscopic image of specimen cut from original blade to measure layer thickness

5.2 Grid modelling

The meshing of layered composite as a second step is itself a time consuming task. The accuracy of numerical calculations depend on the quality of mesh in FEM. At first, a layered geometry is created using CAD software based on the information collected from a microscopic study of the blade. After that, the blade is meshed layer by layer using the Hypermesh software. Only solid hex elements are used for grid generation as shown in Figure 5.4.

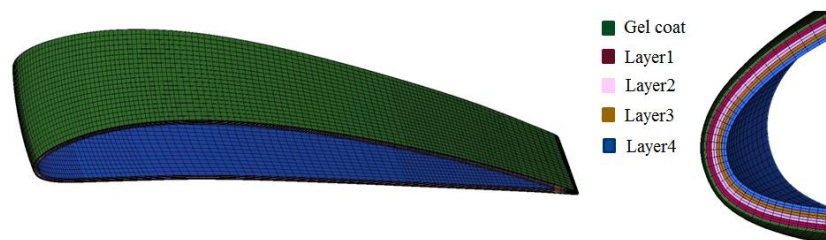


Figure 5.4: Layer by layer hex mesh topology created for the blade

5.3 Glue modelling

A gap is defined between each layer to incorporate the effect of glue and delamination of the layers. Between each single layer, 10 micron uniform gap thickness is maintained. Stiffness and damping of glue is added in terms of contact definition between each single layers. A cohesive zone modelling is used to define the glue behavior. Here, σ_{max} , δ_n , τ_{max} , δ_τ , and η are maximum normal contact stress, normal debonding gap, maximum tangential contact stress, tangential debonding gap and damping coefficient respectively. The maximum normal and tangential contact stress is defined to be 4 MPa. The debonding gap is defined to be 0.1 mm and an artificial damping coefficient is defined equal to $5 \cdot e^{-2}$. The complete code to implement the CZM model in ANSYS APDL is presented in Eq. (59), (60) and (61).

$$tb, czm, cid, 1, , cbdd \quad (59)$$

$$tbdata, 1, \sigma_{max}, \delta_n, \tau_{max}, \delta_\tau, \eta, \beta \quad (60)$$

$$tbdata, 1, 4e^6, 1e^{-4}, 4e^6, 1e^{-4}, 5e^{-2}, 0 \quad (61)$$

5.4 Material modelling for mixer blade

There are few laboratories, where different types of composites are tested to find material's tensile, flexural and compressive strengths. These data are needed for the stress and strain calculations. To start the calculation, the material data are taken from well know open source 'MATWE' [80]. The initial material data is shown in Table 5.2, which are used for glass fiber, resin and foam.

For the manufacturing, two type of composite layers are used for the mixer blades, one type has glass fiber oriented at 45 degree to the reference axis and other type has random fiber orientation (see Table 5.1). Initially, to incorporate the orientation of the fiber, stiffness is resolved in a global fixed frame of reference as shown in Figure 5.5.

$$Y_x = 5.5 \text{ GPa}$$

$$Y_y = 17.2 * \cos(45) = 8.5 \text{ GPa}$$

$$Y_z = 17.2 * \sin(45) = 8.5 \text{ GPa}$$

Table 5.2: Initial material data of all layers used for simulation (LW: Longitudinal wise; CW: Cross wise)

Material	Modulus - LW/CW [GPa]
Glass fiber reinforced polyester	
Tensile Parameters	17.2/5.5
Flexural Parameters	12.2/5.5
Compressive Parameters	17.2/6.9
Polyester Resin (Gel coat)	
Tensile Parameters	1.1
Flexural Parameters	4
Polyurethane Foam	
All direction(isotropic)	0.01

For the random oriented fibers, cross wise stiffness is considered in all directions. Table 5.3 shows material parameters in all directions for the fiber reinforced polyester. Now the material data and the mesh topology are ready to start the structural calculation. But it is known that composites are anisotropic materials and it have non-linear stress strain curves. Therefore, load dependent deformation experiments are needed to create actual non-linear stress strain curves of current composite materials.

Table 5.3: Detailed material data of each layer in all direction to start the calculation

Modulus	45 degree Oriented fiber	Random
Young's Modulus X direction	5500 MPa	5500 MPa
Young's Modulus Y direction	8500 MPa	5500 MPa
Young's Modulus Z direction	8500 MPa	5500 MPa
Poisson's ratio XY	0.32	0.32
Poisson's ratio YZ	0.32	0.32
Poisson's ratio XZ	0.32	0.32
Shear Modulus XY	5500 MPa	5500 MPa
Shear Modulus YZ	5500 MPa	5500 MPa
Shear Modulus XZ	5500 MPa	5500 MPa

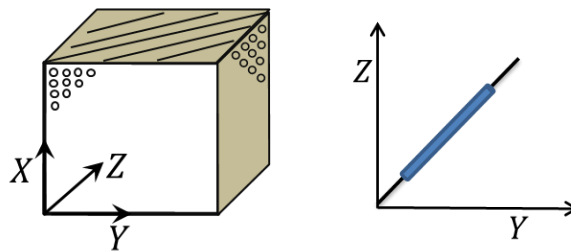


Figure 5.5: Orientation of fiber at 45 degree

5.5 Experimental validation of material model

A load-deformation curve is created experimentally by using Vic-3D technique [81]. Based on the principle of Digital Image Correlation, it provides three-dimensional measurements of displacement and strain. The actual object movement is measured and the Lagrangian strain tensor is calculated at every point on the surface of observation. Vic-3D can measure strains from 50 micron to 20, for specimen sizes ranging from lesser than 1 mm to greater 10 m. This simple and quick method don't need any special illumination or lasers. Moreover, no specimen contact is required during testing.



Figure 5.6: Vic 3D camera setup for the experiment

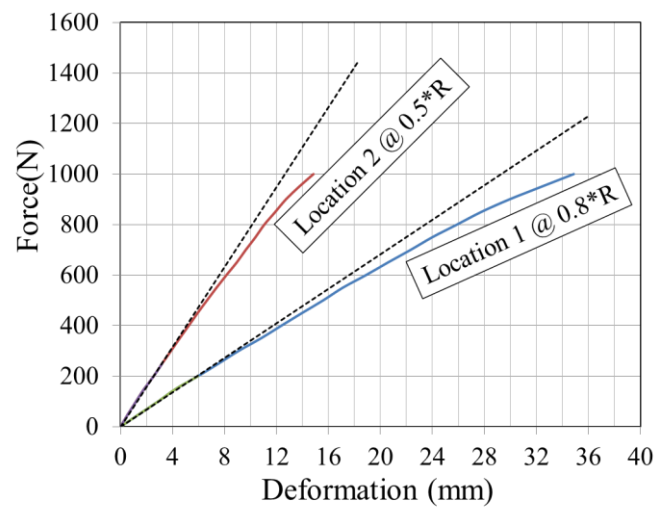


Figure 5.7: Force deformation curve for two location where cameras were focusing

Figure 5.6 shows the camera setup for the deformation measurement of the blade. Deformation and strain are measured at two locations for different amounts of load. The curves are plotted in Figure 5.7. It is observed that load-deformation curves are non-linear. So, material of blade has non-linear material behavior.

After plotting the load-deformation curve from the experiment, the next step was to create the final material data for the numerical FEM calculations. For that, similar boundary conditions like the experimental setup are defined in ANSYS Workbench (Figure 5.10). And, stating material data (Table 5.3) are defined too. The deformation are measured against the load at the same two points, which are observed in the experiments. Then material data is tuned to match experimentally observed blade's deformation.

A comparison of the blade deformation in the numerical simulations and the experiments is shown in Figure 5.8. Tuning of the material data is performed till the load-deformation curves become equal for the experiment and the numerical calculations. Thus the last tuned material is taken as the final material data which is plotted in Figure 5.9. From this, it can be concluded that the nonlinear anisotropic material data developed is acceptable for next studies.

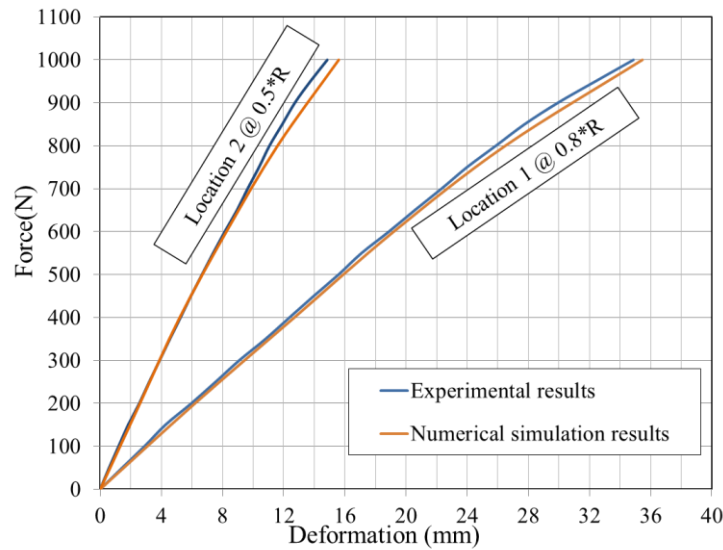


Figure 5.8: Load-deformation curves of the tuned materials are obtained from numerical analysis (saffron) at two locations, which are exactly matching to the experimentally obtained load-deformation curves (blue)

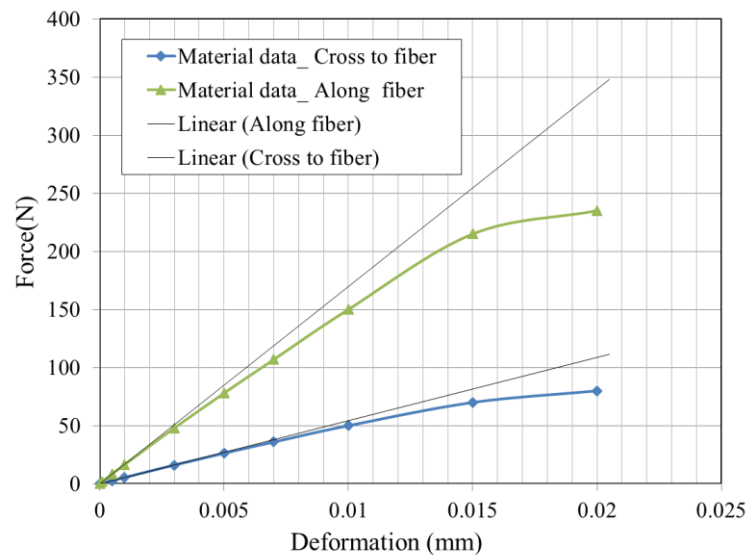


Figure 5.9: Material data of the composite along and cross to the fiber are drawn. The linear interpolation curves are created to justify that the material data curves are non-linear.

After the development of the material model, failure analysis are performed. For this the user defined routines and procedures are developed in ANSYS, which are explained in the following pages.

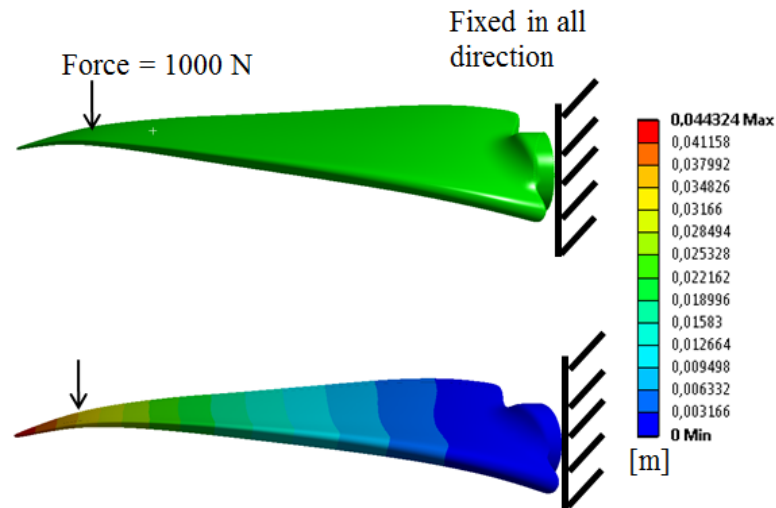


Figure 5.10: Picture shows the boundary conditions used for the numerical analysis. The hub side of the blade is fixed and ramped force up to 1000 [N] is applied at $0.9 \cdot R$ of the blade. Contour of total displacement is plotted.

5.6 Fracture code modelling

Fracture codes for Tsai-Wu, Puck and LaRC criteria are developed in house to find the point of fracture in blades. Before performing fracture analysis of the blades, the fracture codes are validated for small composite probes using the experimental and the numerical techniques.

5.6.1 Probes: Microscopic study

The detailed dimensions of the layered composite probes are given in Figure 5.11. Six probes are used and they have gel-coat layers on the top and bottom of the each probes. Out of six probes, each of two probes have same thickness. So, three groups of the probes are manufactured and each groups have different number of layers and thicknesses as shown in Table 5.4. For each group, tensile and bending destructive tests are performed to find load-deformation curve, tensile ultimate strength and bending ultimate strengths for the probes. The thicknesses of gel-coats are 0.65 mm at top and 0.3 mm at bottom in the used probes. Cross-sectional views for three groups of probes is

shown in Figure 5.12, which shows the number of layers and the thickness of layer and probes.

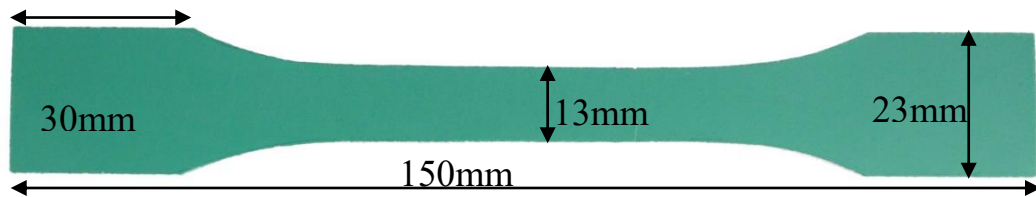


Figure 5.11: Detailed dimensions of the probe used for the validation of the fracture code

Table 5.4: It shows detailed information for the type of the test used for given probe. For each probes tensile and bending test are performed. The thickness and number of layer for each probes are presented in this table.

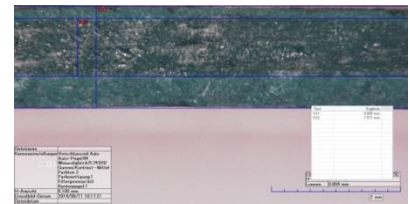
Probes	Group	Thickness	Number of layer	Type of test
1	A	3.5 mm	3 layers	Tensile test
2		3.5 mm	3 layers	Bending test
3	B	2.7 mm	2 layers	Tensile test
4		2.7 mm	2 layers	Bending test
5	C	1.8 mm	1 layer	Tensile test
6		1.8 mm	1 layer	Bending test



(a)



(b)



(c)

Figure 5.12: (a) Group A type of the probes have total thickness of 3.5 [mm] and 3 layers; (b) Group B type of the probes have total thickness of 2.7 [mm] and 2 layers; (c) Group C type of the probes have total thickness of 1.8 [mm] and 1 layer. The information about number of layers for each probes are provided by manufacturer.

5.6.2 Probes: Grid modelling

A layered hex mesh is created for each type of probes as shown in Figure 5.13. The thickness of each layer is defined as per information taken from microscopic study of the probe and manufacturer. A 10 micron gap is defined between each layer to incorporate the glue effect. The minimum angle for the solid elements are maintained up to 68 degree.

After meshing in Hypermesh, the mesh is exported to ANSYS Workbench for numerical simulations.

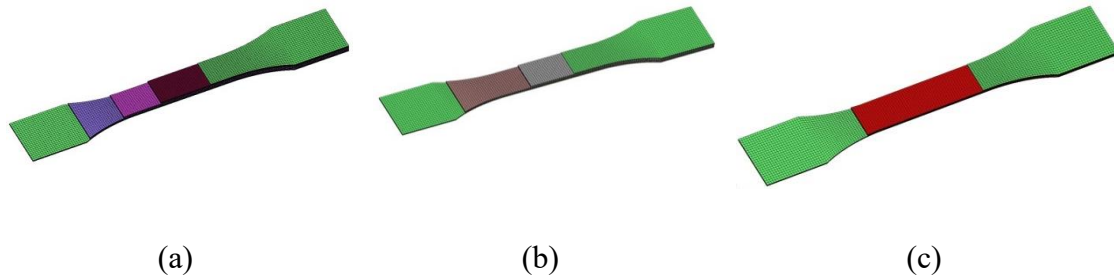


Figure 5.13: The hex grid mesh topology for (a) Group A, (b) Group B and (c) Group C type of the probes is shown. An each layer is shown with different color. Gelcoat is displayed with green color.

5.6.3 Probes: Experimental study

The destructive tensile and bending tests are performed to create the load-deformation curves and to find the failure ultimate strengths of material. The experimental setup for the tensile and bending tests are shown in Figure 5.14 and Figure 5.15 respectively.

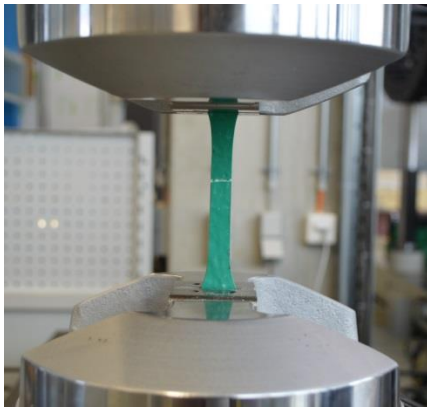


Figure 5.14: The destructive tensile experiment setup. The point of fracture is observed.



Figure 5.15: The destructive bending experiment setup. The fracture is seen on the tensile loading side of the probe.

5.6.4 Probes: Material modelling and simulation

To design correct material data, fiber orientation of each layer is analyzed. It is observed that the fiber orientation is random as shown in Figure 5.16. So, the material stress strain curve is taken same for all direction. The material data is tuned to get the load deformation curve for all types of probes.



Figure 5.16: The random glass fiber orientation inside the probes is observed.

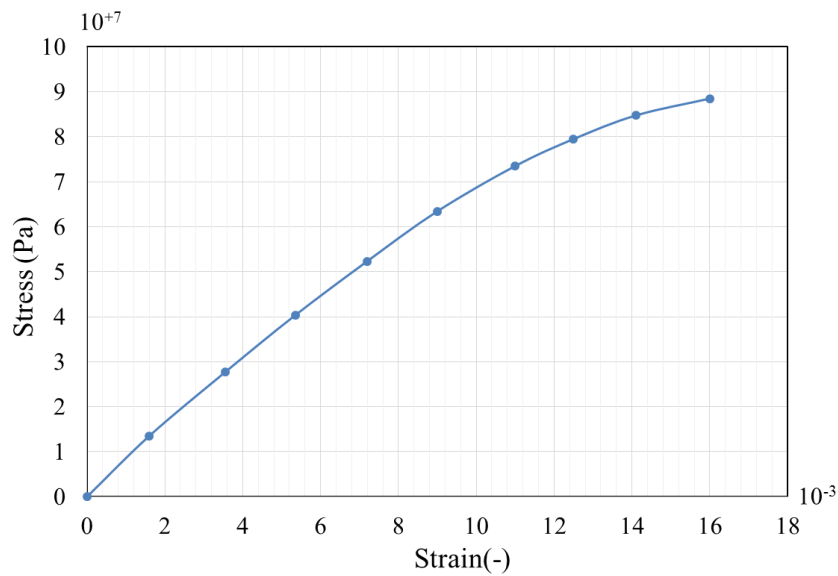


Figure 5.17: The tuned material data for the probes in all directions.

For the numerical simulation boundary conditions are setup to be similar to the experimental setup (Figure 5.18 and Figure 5.19). The load deformation curve for the tensile and bending tests generated from the numerical simulation using tuned material data are shown in Figure 5.20 and Figure 5.21 respectively. The stress strain curve for final tuned material is plotted in Figure 5.17.

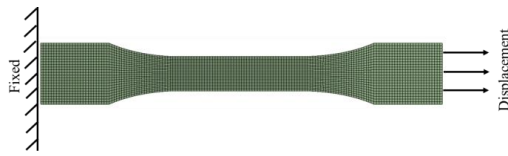


Figure 5.18: The boundary condition used for the numerical analysis under the tensile loading.

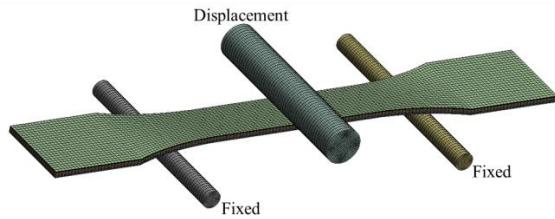


Figure 5.19: The boundary condition used for the numerical analysis under the bending loading

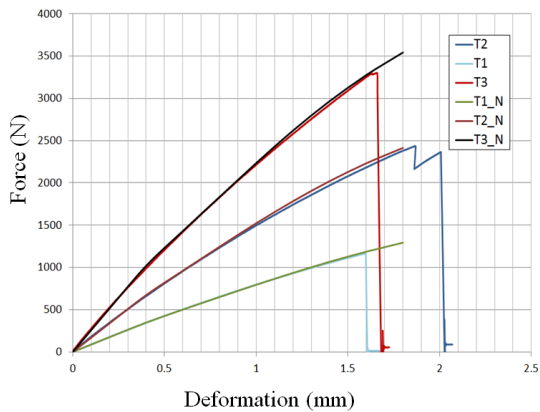


Figure 5.20: The T1 (single layered probe), T2 (double layered probe), and T3 (triple layered probe) are experimentally obtained force deformation curves for the probes under the tensile loading till probes are broken. T1_N, T2_N and T3_N are the force deformation curves obtained after the numerical analysis of the probe under the tensile loading. The material model is tuned to get same force deformation curves for each type of the probes from the numerical analysis and experimental results.

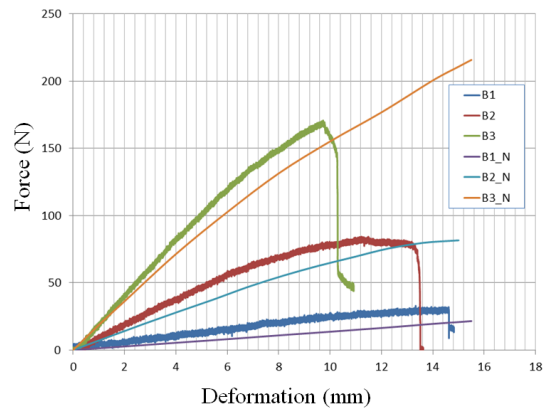


Figure 5.21: The T1 (single layered probe), T2 (double layered probe), and T3 (triple layered probe) are experimentally obtained force deformation curves for the probes under the bending loading till probes are broken. T1_N, T2_N and T3_N are the force deformation curves obtained after the numerical analysis of the probe under the bending loading. The material model is tuned to get same force deformation curves for each type of the probes from the numerical analysis and experimental results.

5.6.5 Probes: Simulation results

At first, the point of fiber tensile failure is calculated for the probes using Tsai-Wu, Puck and LaRC criteria. All selected criteria are able to find the fracture at the same place where fractures are occurred during experiments (see Figure 5.22(a)-(c)). The position of the point of fracture in the experiment is shown in Figure 5.22(d), and it matches with the numerically calculated fracture point. This shows that written code is able to predict tensile fracture correctly for composites. Similar analysis are done for the bending tests. In the bending tests, one side of probe experiences compressive load and other side experiences tensile load. In experiment as shown in Figure 5.15, tensile side failed before

the compressive side. After the fracture calculation, all criteria predicted the failure at the tensile load side as shown in Figure 5.23, Figure 5.24 and Figure 5.25. It can be concluded that the criteria worked well and able to predict the point of fracture in probes. The in house fracture code is ready for application to any composite parts to predict fracture.

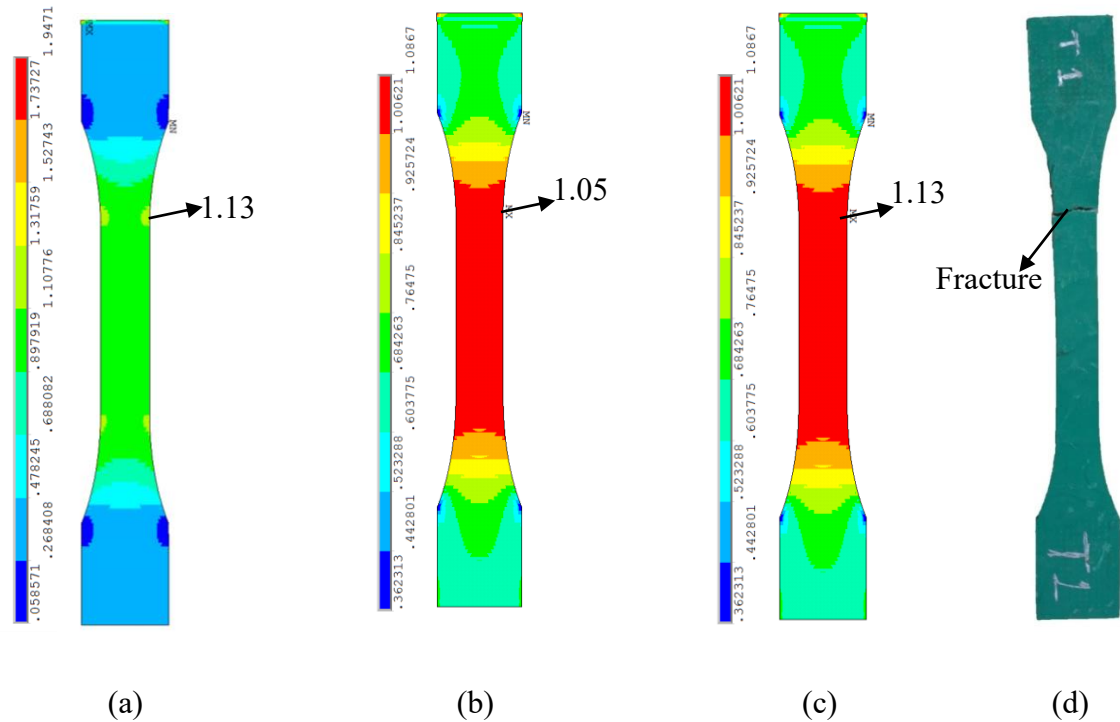


Figure 5.22: (a) Contour plotted for Tsai-Wu criterion, (b) Contour plotted for Puck fiber tensile criterion, (c) Contour plotted for LaRC fiber tensile criterion, (d) Fracture of the probe under tensile load during experiments. All fracture criteria find the point of fracture at the same point where fracture occurred while experiment.

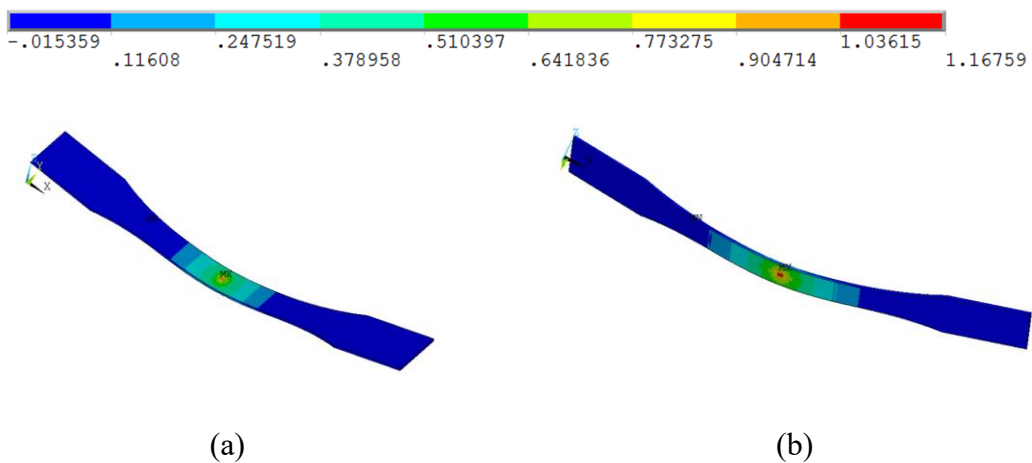


Figure 5.23: Contour of the Tsai-Wu criterion during the bending loading condition, (a) plotted on the compressive side of the probes, (b) plotted on the tensile side of the probes. It is observed that the used criterion shows the point of fracture on tensile side of the probe during the bending loading conditions.

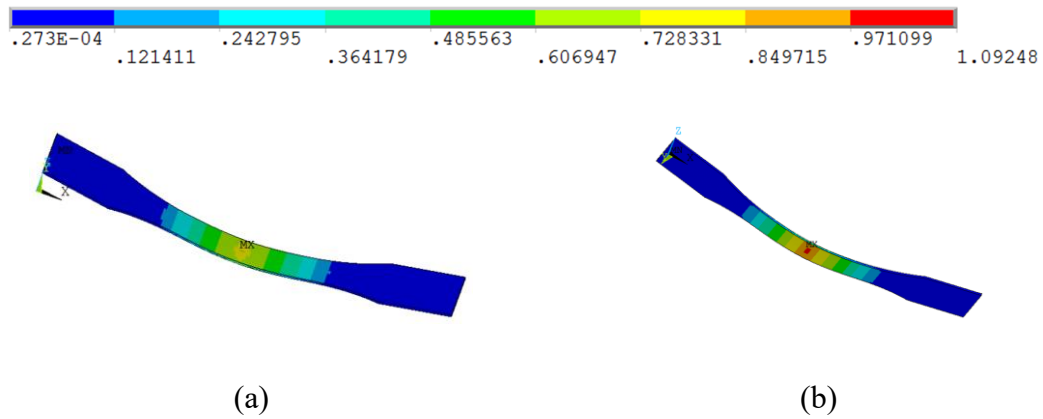


Figure 5.24: Contour of the Puck fiber failure criteria during the bending loading condition, (a) plotted on the compressive side of the probes, (b) plotted on the tensile side of the probes. It is observed that the used criterion shows the point of fracture on tensile side of the probe during the bending loading conditions.

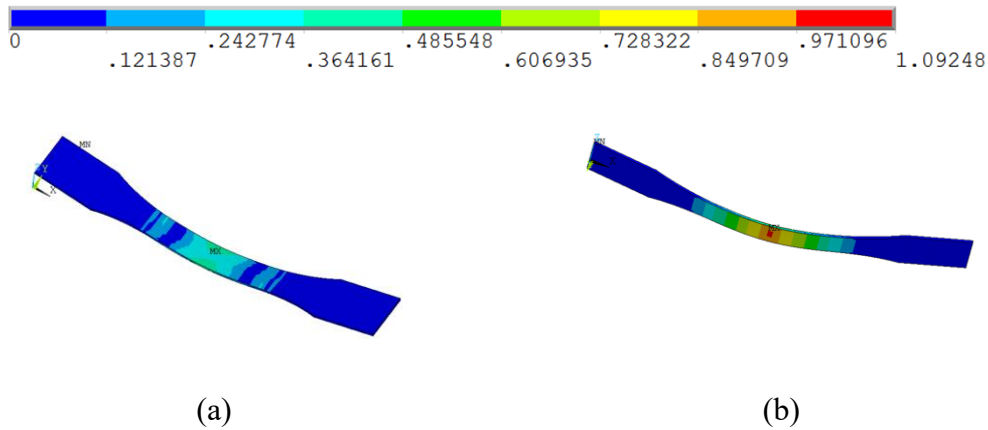


Figure 5.25: (a) Contour of the LaRC fiber failure criteria during the bending loading condition, (a) plotted on the compressive side of the probes, (b) plotted on the tensile side of the probes. It is observed that the used criterion shows the point of fracture on tensile side of the probe during the bending loading conditions.

Contour for tensile failure index of Puck and LaRC criteria are exactly same because equation for failure index are same for both. But Twai-Wu uses different formulation for tensile failure index. For compressive load, contour for failure index are different for each used criteria as they have different formulation for compressive failure prognostic.

Until now, an extensive structural modelling for the mixer blades and fracture modelling for the composite materials are presented. For the tidal-turbine similar procedure is followed. The tidal-turbine blade is made of random-oriented carbon-fiber reinforced composites (without any layer) and so it is less complicated to model for the

numerical simulation rather than the mixer blades. Although, its material model is developed in house and used for the simulations.

5.7 Material model for the tidal-turbine blade

The tidal-turbine blades (made of random-oriented carbon-fiber reinforced composites) are lighter than metallic propeller. The injection molding technique can be used to manufacture tidal blades. This manufacturing technique is easier than the manufacturing technique for layered composite blades and it is excellent advantage for industrial applications. So, some industries are adopted the injection molding technique for random-oriented carbon-fiber reinforced composites to manufacture the blade rather than layered composites or metals. The material can be considered as an isotropic material. The Young's modulus and poisson's ratio are $1.85e^{+10}$ Pa and 0.3 respectively for this material. Its strengths are similar to the glass fiber reinforced composites. A high quality hex dominant grid is used to mesh complete blade. For the mesh quality control, Jacobian lesser than 0.6 is maintained.

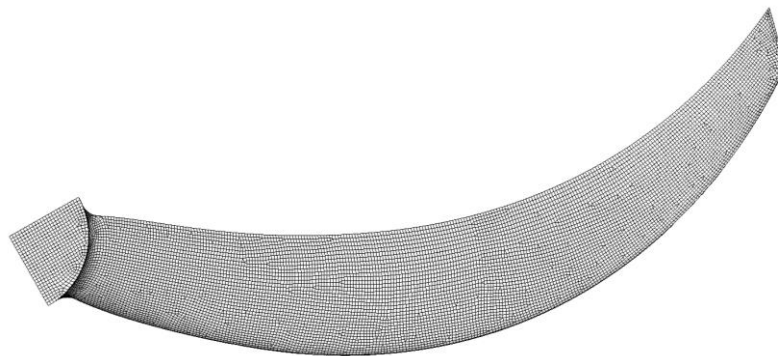


Figure 5.26: The mesh topology used for the tidal-turbine blade

A structural model for the mixer and tidal-turbine are ready for FSI simulations. In next sections, uni-directional and bi-directional fluid-structure interaction are presented.

6 Fluid-structure interaction

The interactions between incompressible fluid flows and flexible composite structure are nonlinear multi-physics phenomena. Applications and importance of fluid-structure interaction are discussed in section 1.1. Various methodologies are developed to handle fluid-structure interaction phenomena as explained in section 3.4. In this chapter uni-directional and bi-directional implicit iterative fluid-structure interaction are focused and analyzed in detail involving conforming mesh for the interface.

6.1 Uni-directional fluid-structure interaction

In the uni-directional approach, a converged solution of one field is used as a boundary condition for the second field for once, as shown in Figure 6.1.

$$\Omega_f(t_{n=converged}) \longrightarrow \Omega_s(t_{n=Converged})$$

Figure 6.1: The uni-directional approach for the fluid-structure interaction simulations

A CFD simulation is performed using the SST turbulence model with Gamma-Theta transition model for the mixer propeller and tidal-turbine. The value of fluid forces are calculated and presented in Table 6.1. But for FSI simulations, the pressure distribution is needed to be mapped accurately over the blade surface in structural domain.

6.1.1 Mapping

For the mapping, nodes on the interaction surface of the structural domain are projected normal onto the interaction surface of the fluid domain. F_x , F_y and F_z are calculated based on equation (62), (63) and (64) for each element face of the interaction surface. Then pressure load vector is calculated based on equation (65) and (66) to apply the load onto the nodes of the structural interaction surface mesh. 98 percent mapping accuracy is achieved by this algorithm.

Table 6.1: The fluid forces components from CFD analysis and mapped fluid forces components for structural simulations on the mixer and tidal-turbine blades.

Force component	Mixer propeller Forces @ 0.05 m/s inlet velocity		Tidal-turbine Forces @ 2.5 m/s inlet velocity	
	Fluid pressure load [N]	Structural load [N] (Mapped)	Fluid pressure load [N]	Structural load [N] (Mapped)
X-component	-2130	-2105	-8505	-8522
Y-component	-541	-530	-1486	-1434
Z-component	-31	-28	1157	1219

$$F_x = Pressure * Area * Normal X \quad (62)$$

$$F_y = Pressure * Area * Normal Y \quad (63)$$

$$F_z = Pressure * Area * Normal Z \quad (64)$$

$$\overrightarrow{Pressure\ load} = \left(\frac{F_x}{Area}, \frac{F_y}{Area}, \frac{F_z}{Area} \right) \quad (65)$$

$$|Pressure\ load| = Sqrt \left(\left(\frac{F_x}{Area} \right)^2 + \left(\frac{F_y}{Area} \right)^2 + \left(\frac{F_z}{Area} \right)^2 \right) \quad (66)$$

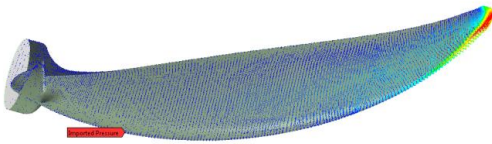


Figure 6.2: Mapping of CFD force on the mixer blades for structural simulations

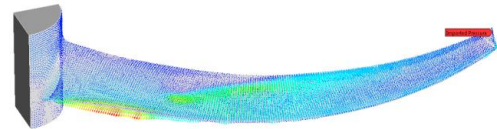


Figure 6.3: Mapping of CFD force on the tidal-turbine blades for structural simulations

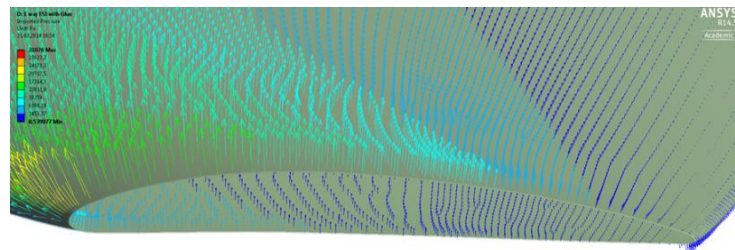


Figure 6.4: Mapping force vector on the mixer blades for structural simulations

Figure 6.2 and Figure 6.3 show the mapped CFD forces on the blade surface of the mixer and the tidal-turbine respectively for the structural simulation. The mapped force vector is displayed in Figure 6.4 for general understanding.

6.1.2 Simulation results

The uni-directional FSI simulations computed a deflection of the mixer propeller blade near about 58 mm against the flow direction as presented in Figure 6.5. The hub is fixed during the simulations. The Max-Principal stresses are analyzed and a zone of concentrated stresses near to hub is observed (Figure 6.7).

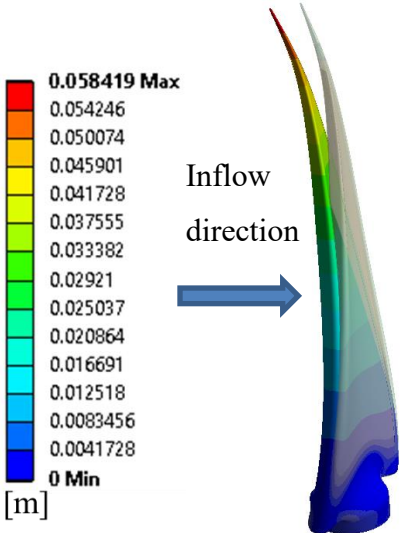


Figure 6.5: Contour for total deformation of the mixer blade. The 58 mm maximum deformation is observed at the tip of the blade.

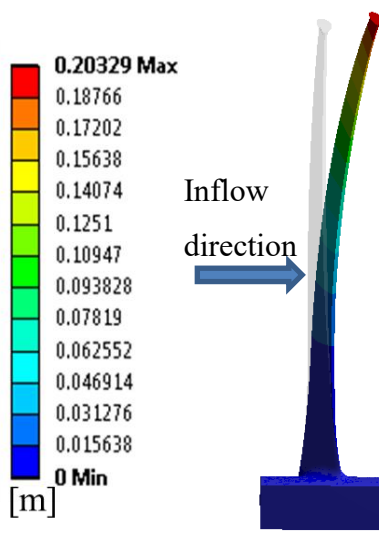


Figure 6.6: Contour for total deformation of the tidal-turbine blade. The 200 mm maximum deformation is observed at the tip of the blade.

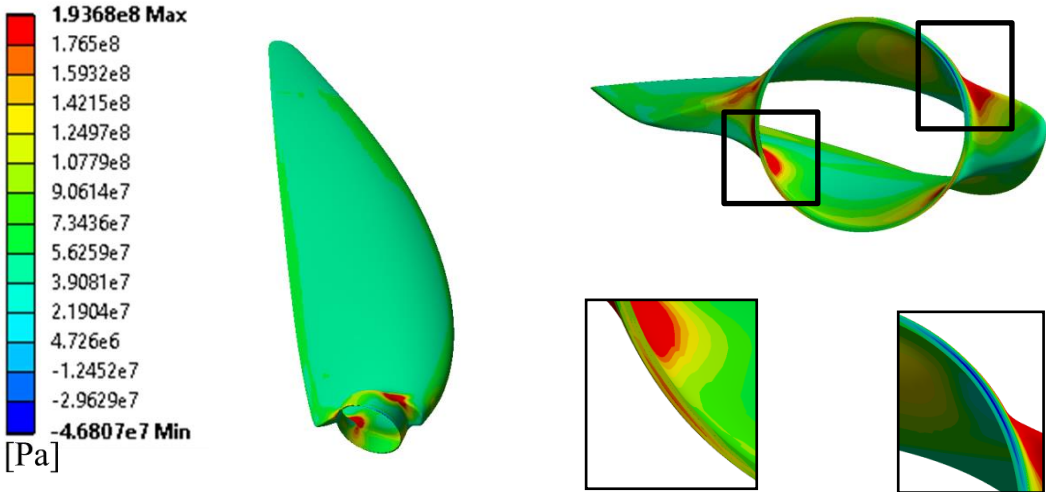


Figure 6.7: Contour for Max-Principal stress distribution over the blade. The zones with high stress concentration can be noticed near to hub side of the blade (left). On the right side stress distributions over the layer thickness are analyzed. One side of the blade is experiencing compressive load and other side is experiencing tensile load.

A detailed stress analysis for each layer of the composite is performed and presented in Figure 6.8. It is important to pay attention on stress value experienced by each layer. The highest stresses are observed in layer 1 and with every subsequent layer stresses are decreasing. All layers are designed with a similar thicknesses but this manufacturing idea is not an appropriate approach. The thickness modification or change in fiber orientation will be helpful to improve the strengths of each layer.

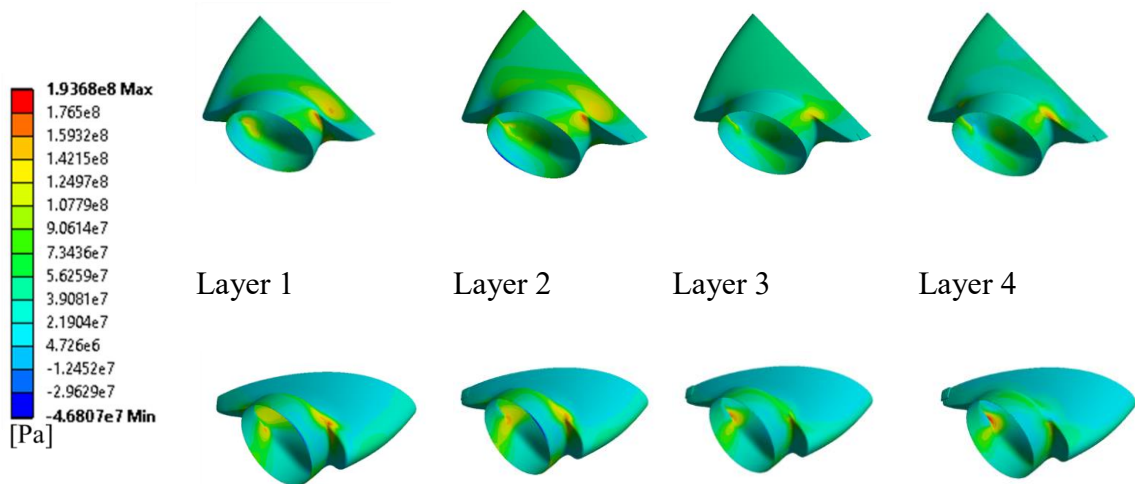


Figure 6.8: Contour plot of Max-Principal Stresses for each single layer of the mixer blade

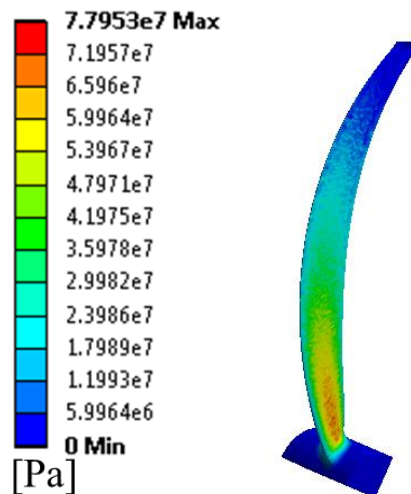


Figure 6.9: Contour of von-Mises stress for the tidal-turbine blade. A high stress concentration zone is near to the hub.

The tidal-turbine blade is made of random-oriented carbon-fiber reinforced composites as explained in a previous section. Its simulation shows a deflection of the blade near about 203 mm in the direction of flow as displayed in Figure 6.6. Similar to

the mixer blade it also shows highest stress zone near to the hub, which is fixed during the simulations (Figure 6.9). In both simulations (mixer and tidal-turbine), the final deformation is quite high, which cause equally high deformation of the fluid domain. Bi-directional FSI simulations for the large deformation is taken as a next task in this research work, which is explained in the following sections.

6.2 Bi-directional fluid-structure interaction

For a large deformation of the blade, a coupled fluid-structure analysis becomes more and more important for the optimization and the reliability of the product in real applications. A few FSI handling strategies are presented in literature [30], [33] and [35]. As another strategy, the bi-directional iteratively implicit modelling approach is used for the simulation of large deformation FSI problems using a mesh deformation and re-meshing method. The fluid and structural solvers are solved separately, and then deformation and force data are transferred using a mapping technique. A transient bi-directional implicit FSI has three levels of iteration named as ‘time loop’, ‘coupling loop’ and ‘field loop’ as depicted in Figure 3.10. The field loop is the most inner loop which is used to converge the flow field within a solver. It stops when the flow field variables reach their convergence target. At the coupling loop, load and displacement are transferred between the fluid and structural solver. It stops when both the force and the displacement converge. The time loop is used for the advancement in the real time transient simulation.

6.2.1 Mapping

Forces are mapped using a flow-based general grid interface method, which is available in the ANSYS commercial software. It enforces a conservation of quantity, and displacement is mapped using a profile preserving algorithm with relaxation control. A control surface is created and element sectors from both sides are projected onto it. Then flow from the source is projected and split between the control surfaces. Later control surface flows are gathered and transferred to the target side. Node position and element size are maintained on the blade surface in the fluid and structure domain for 100 percent perfect mapping.

6.2.2 Mesh deformation and Re-meshing

A mesh deformation is quite large because of large structural deformations. During mesh element deformation, element quality decreases, and it leads to a crash of the solver. To solve this quality problem, re-meshing plays a key factor in simulations. A local cell re-meshing algorithm is used based on cell skewness, and minimum and maximum element lengths for creating valid element while simulation using the FLUENT commercial software.

In this method, if the element violates any quality criteria, the bad element is smoothed using a spring based method along with a full dynamic mesh domain. If it does not work, the bad element is deleted along with neighboring elements and re-meshed with better elements. For this case, maximum cell skewness and spring constant are set at 0.85 and 0.1, respectively, in FSI simulation. The marking of cell-based scenes is done at every step. If the local cell re-meshing is failed to create a valid local element the full dynamic zone is re-meshed based on a size criterion. Boundary layer mesh is created on the blade surface for accurate CFD results and it is not re-meshed at any step. The initial mesh of the fluid domain is presented in Figure 6.10. Grid before and after mesh deformation, smoothing and re-meshing with respect to time are compiled in appendix 'D'.

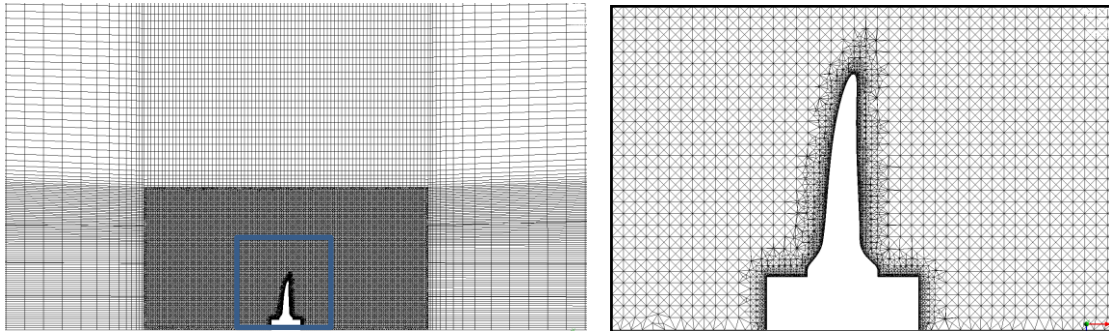


Figure 6.10: Tetra mesh is used for meshing the rotor domain with prism boundary layers. Hex grid is created for the stator domain.

6.3 Comparison between Uni-directional and Bi-directional FSI

A simulation is performed for 0.5 s with a 0.015 s increment time step, 5 coupling iterations per loop and 500 field convergence iterations for each inlet velocity of fluid.

Here, plots are given for one set of boundary conditions for better comparison of uni-directional and bi-directional FSI.

In uni-directional FSI, cross coupling of the solver is not used, which limits the calculation of change in the flow field due to blade deformation. It is the reason for giving a deformation of 58 mm which is larger than a bi-directional FSI final deformation of 50 mm as plotted in Figure 6.11. The final thrust on the blade in bi-directional FSI is about 1872 N. The flow field is changing due to its deformation, which reduces thrust. Consequently, the deformation becomes smaller than the deformation predicted by the uni-directional FSI.

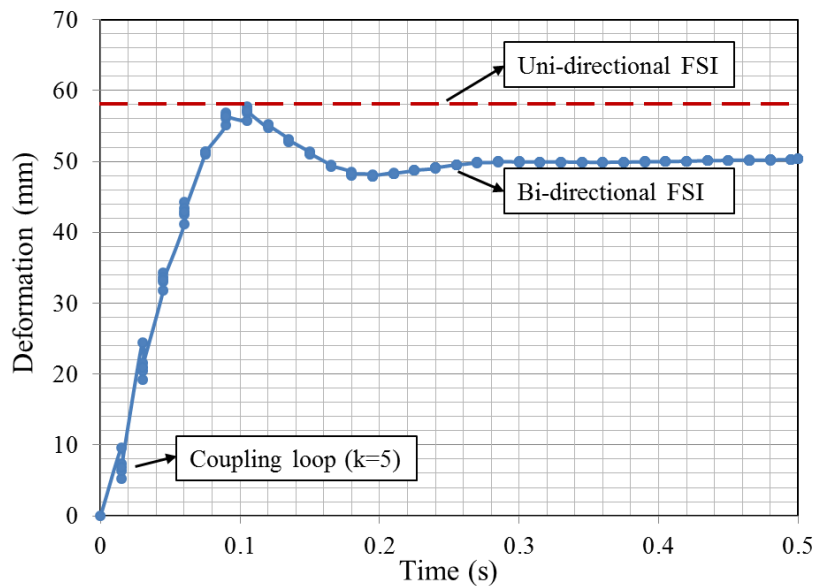


Figure 6.11: Total deformation at the tip of the mixer blade in bi-directional FSI versus time. Final deformation obtained in uni-directional FSI is plotted in red curve to show the difference.

The final pressure distribution on the blade after its final deformation is not possible to calculate in uni-directional FSI, which is possible to generate in bi-directional FSI. The pressure contours are plotted for the both sides of the blade observed in uni-directional FSI and bi-directional FSI. On the pressure side of the blade in bi-directional FSI, the pressure on the tip of the blade is lesser than the pressure at the same point in uni-directional FSI, as shown in Figure 6.12 (a)-(b). Pressure on the suction side of the blade in uni-directional FSI and in bi-directional FSI are almost equal, as shown in Figure 6.12(c)-(d).

Moreover, a blade loading curve is plotted in Figure 6.13 for the blade in uni-directional FSI and in bi-directional FSI where a difference in pressure on the pressure side for both cases is observed. To make this clear, the line integral of the pressure per unit area is calculated for an aero-foil at 0.9 R of the blade. In bi-directional analysis, it is 1330 N, which is 1463 N in uni-directional FSI. Therefore, it can be concluded that the pressure distribution changes with deformation of the blade, which causes change in the thrust value and finally leads to a change in the flow field. It goes on till a convergence is not reached.

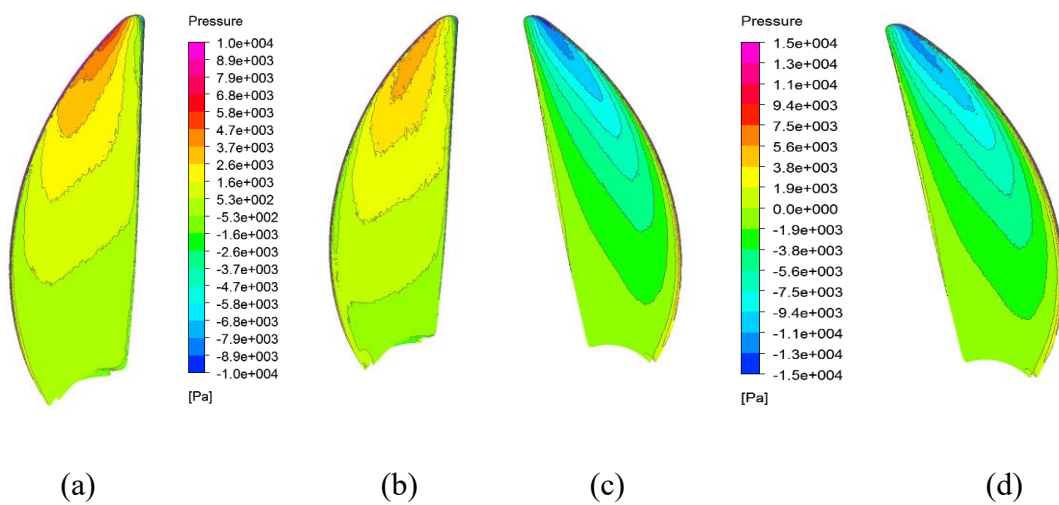


Figure 6.12: (a) Static pressure distribution over pressure side of the blade in uni-directional FSI, (b) Static pressure distribution over pressure side of the blade in bi-directional FSI, (c) Static pressure distribution over suction side of the blade in uni-directional FSI, (d) Static pressure distribution over suction side of the blade in bi-directional FSI

The second advantage of bi-directional FSI over uni-directional FSI is that it observes the change in angle of attack of the blade. The hub is fixed about the center of the blade system and rotation is defined in the structural domain just as in the fluid domain. Deformation and pitch angle are changing non-linearly from bottom to tip of the blade as shown in Figure 6.14. Change in the pitch angle along the radius of the blade is decreasing and the maximum pitch angle change is up to 2.8 degree. It is a primary reason for the reduction of thrust generated by the blade from 2130 N to 1872 N.

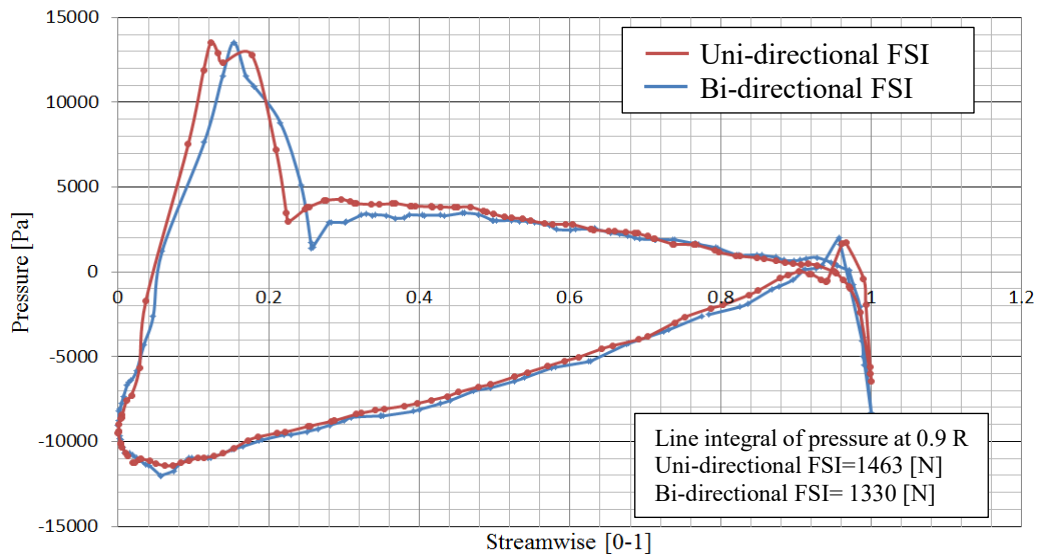


Figure 6.13: Blade loading curve after uni-directional FSI (red) and bi-directional FSI (blue) at 0.9 times of radius of the mixer blade.

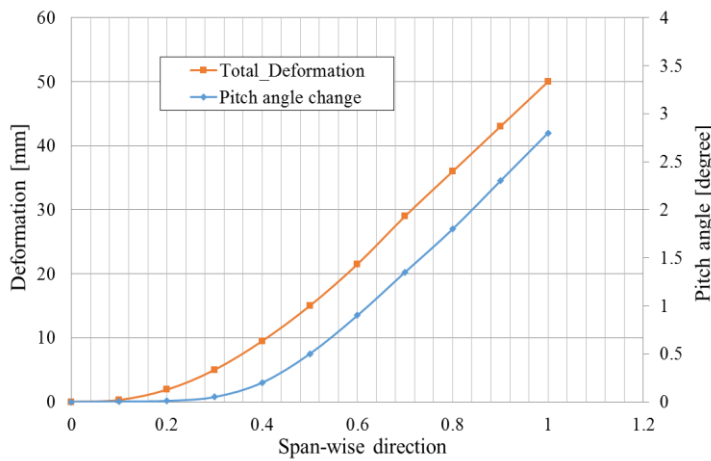


Figure 6.14: Deformation and pitch angle change over the radial direction of the blade in bi-directional FSI. At 0.2 R deformation slope changes significantly.

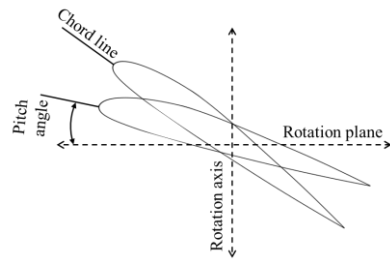


Figure 6.15: Schematic view for pitch angle change

The von-Mises stress is presented in Figure 6.16(a), where a high-stress, critical zone is near to the hub, as it is fixed about the center. The reason for the stress concentration could be justified from Figure 6.16(b), where it can be noticed that deformation near to hub is almost zero. The deformation gradient is changing very fast at 0.2 R of the blade, which can be understood from the curve plotted in Figure 6.14. A similar process with given parameter for re-meshing and mesh smoothing can be used for bi-directional FSI

simulation of any other propeller or turbines blades. To reduce repetitive work, results of bi-directional FSI for the tidal-turbines are not published here.

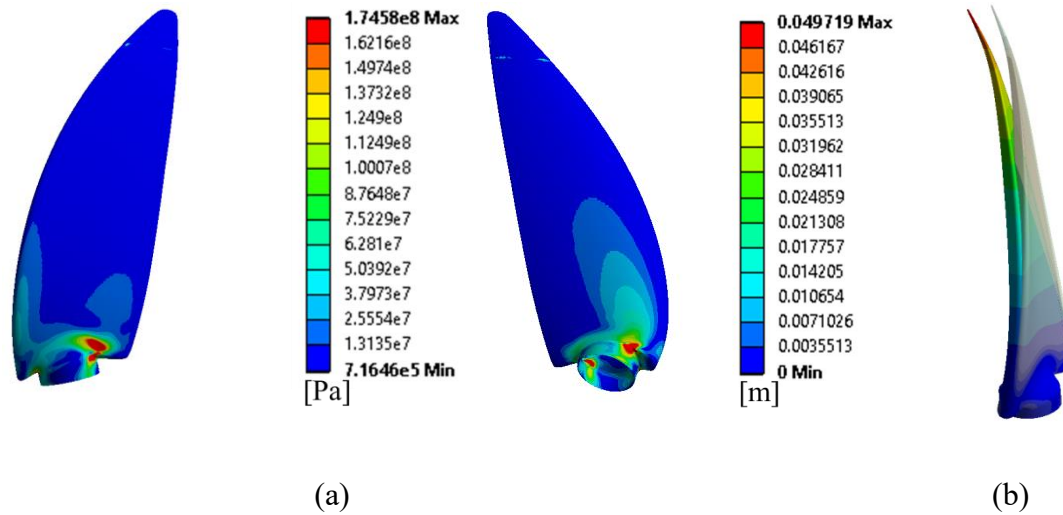


Figure 6.16: (a) Von-Mises stresses over the blade and high stress concentration zone is near to the hub. (b) Contour plot for total deformation of the blade, where deformation at the hub side of the blade is almost zero.

6.4 Fracture analysis

The fracture codes are implemented in house and validated for the probes as explained in section 5.6. The same tested code is applied for the layered composite blade to find the location of fracture. All fracture codes are predicting the potential location of fracture near to the neck of the blade. The result of Tsai-Wu criterion is shown in Figure 6.17. The result of LaRC criteria are shown in Figure 6.18, Figure 6.19 and Figure 6.20.

Puck and LaRC criteria are predicting same location and magnitude for the maximum value of failure index. The Tsai-Wu criterion is predicting failure index value near about 0.75, where LaRC and Puck criteria are predicting failure index value near about 0.67 using tensile failure criterion. Moreover, the contour of failure index for the blade is plotted using the LaRC compressive failure criterion and LaRC mixed mode criterion. The maximum value of failure index are predicted for these criteria are 0.66 and 0.41 respectively. All predicted values of failure index are lesser than one. So, it can be concluded that the mixer material can sustain the maximum thrust.



Figure 6.17: The contour and maximum value of failure index calculated by Tsai-Wu criterion.

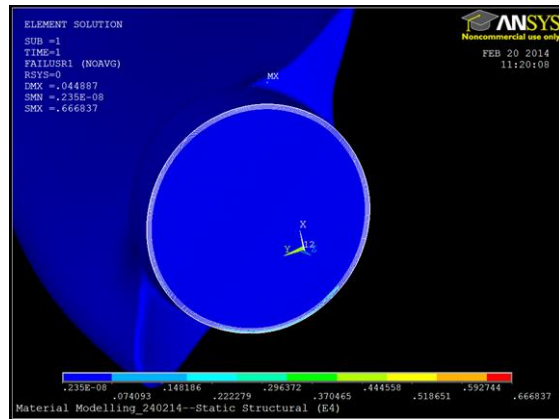


Figure 6.18: The contour and maximum value of failure index calculated by LaRC criterion (fiber tensile failure).

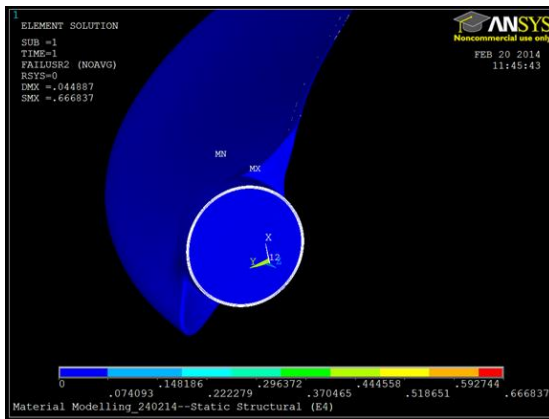


Figure 6.19: The contour and maximum value of failure index calculated by LaRC criterion (fiber compressive failure).

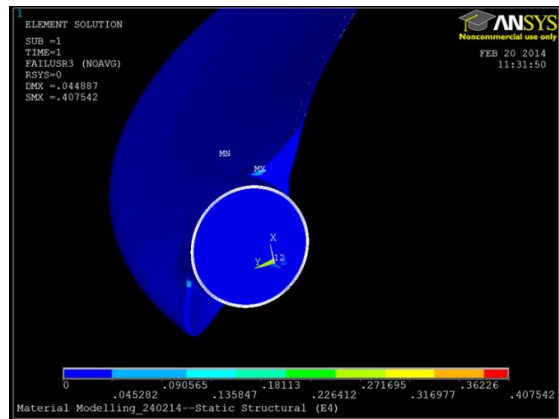


Figure 6.20: The contour and maximum value of failure index calculated by LaRC criterion (mixed mode failure).

For the tidal-turbine, fracture analysis is done for 2.5 m/s and 5 m/s inflow velocity. The ultimate tensile strength of the random-oriented carbon-fiber reinforced composites is 240 MPa. The thrust at these two point are 8100 N and 21000 N respectively as presented in Table 4.5. For these two thrust forces per blade, Tsai-Wu predicts failure index 0.34 and 1.04 respectively as shown in Figure 6.21 and Figure 6.22 .

The random-oriented carbon-fiber reinforced composites material is considered as isotropic material so the failure index by Tsai-Wu criterion is only presented. In these figures the location of fracture is on the surface of the blade and this location experiences tensile load. The maximum water inflow velocity in tides is observed up to 7 m/s. It is observed from the failure analysis that even at 5 m/s inflow velocity, failure index is more

than one. It means that the tidal-turbine blade will fail in real application if inlet velocity will reach or go above 5 m/s.

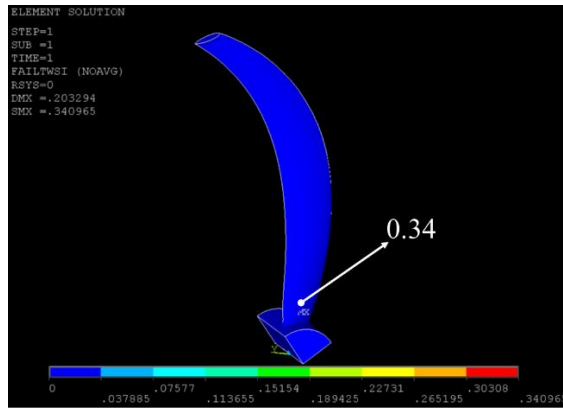


Figure 6.21: The contour and maximum value of failure index calculated by Tsai-Wu criterion at 2.5 m/s inflow velocity

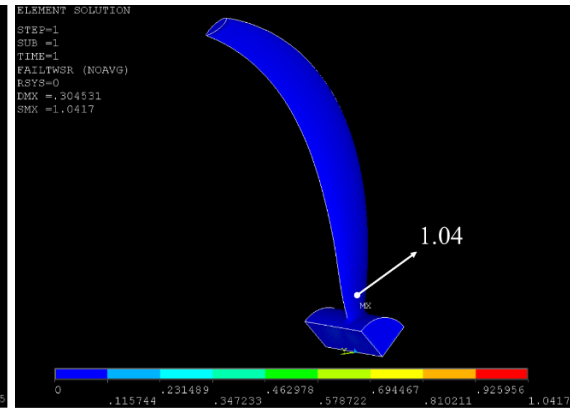


Figure 6.22: The contour and maximum value of failure index calculated by Tsai-Wu criterion at 5 m/s inflow velocity

Stable simulation of strongly coupled fluid-structure interactions involving large deformations is achieved for composite blades. Various benefits of FSI is discussed in detail. But additionally it can be used as a tool to solve real time problem for submersible turbo machines. 3D tailoring of composite blade is done based on FSI simulation results. An application of FSI is shown in next chapter.

7 Application of FSI: blade pitch control

Blade pitch control is necessary to improve blade reliability and to generate constant power for different boundary conditions. In general, blades are pitched using sensor based electro-mechanical instruments. This technique is used in wind turbine applications. This is an expensive technique and moreover it needs more attention for underwater applications. Thus, this technique is not suitable for tidal-turbines. This motivates to explore the possibility of automatic pitch of the blade because of composite materials.

It is well explained in previous chapter that change in an angle of attack of the fluid leads to change in a pressure distribution over the blade surface for an identical boundary conditions. The pressure changes lead to the changes in thrust values. If a pitch is done towards the feather position then angle of attack will decrease. This cause reduction in lift coefficient as well as drag coefficient significantly.

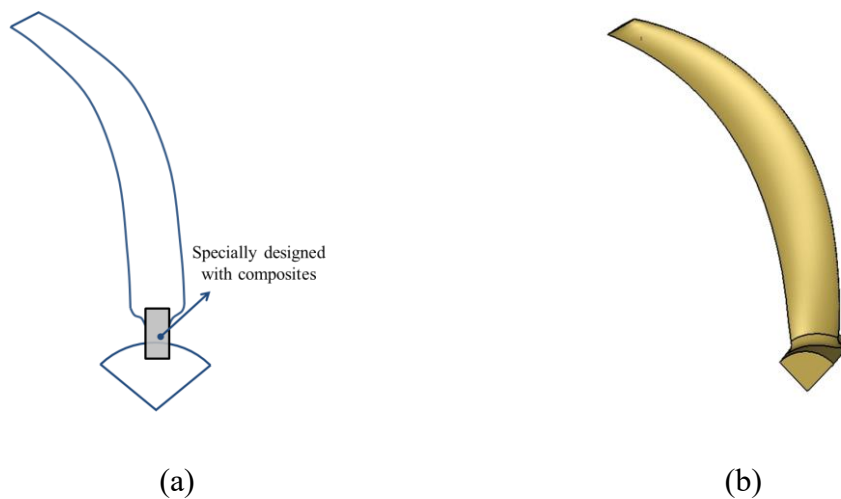


Figure 7.1: (a) Schematic view of connector position; (b) Original blade design of the tidal-turbine blades

The pitch towards the feather position can be done passively by using fluid forces itself. No electrical part is needed. This idea is investigated in this chapter using FSI. It is easy to understand that if pitch is done at the hub end then complete blade will change its angle of the attack. For the passive pitching of the blade, a connector is designed between

the blade and hub as shown in Figure 7.1(a). To make the point clear, original design of the blade is shown in Figure 7.1(b). But the position, shape and dimensions of the connector must be selected logically.

For known pressure force at point ‘P’, the direction of moments are different about the points ‘1’ and ‘2’ as schematically depicted in Figure 7.2. For passive pitch position ‘1’ is favorable position for connector. Moreover, the cross-sectional space is more towards the leading edge of the blade. So, the design of thicker connector can be realized.

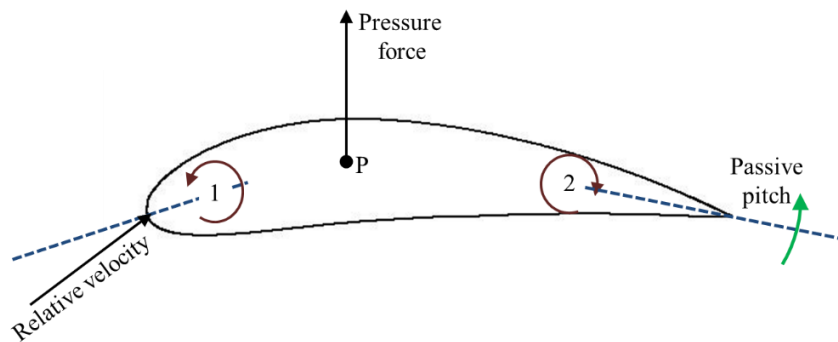


Figure 7.2: The moment at the leading and the trailing edge of aero-foil because of pressure force. A connector position is considered at ‘1’ to get passive pitch of the blade

After finalizing the position of a connector, shape of connector is focused as a next task. Basic study on the shape of connector design is done by Hallier and he proposed ‘U- shape’ profile for it [82] as shown in Figure 7.3. But it was very hard to implement with the blade for real application. It is realized that the shape of connector is a key factor for its bending and torsional rigidity. Various shape and related rigidity are analyzed by Erhard [83] and the findings are summarized in Figure 7.4.



Figure 7.3: U-Profile connector added at the hub end of the blade. Cross-sectional view of connector (left) and mesh topology (right) are shown [82].

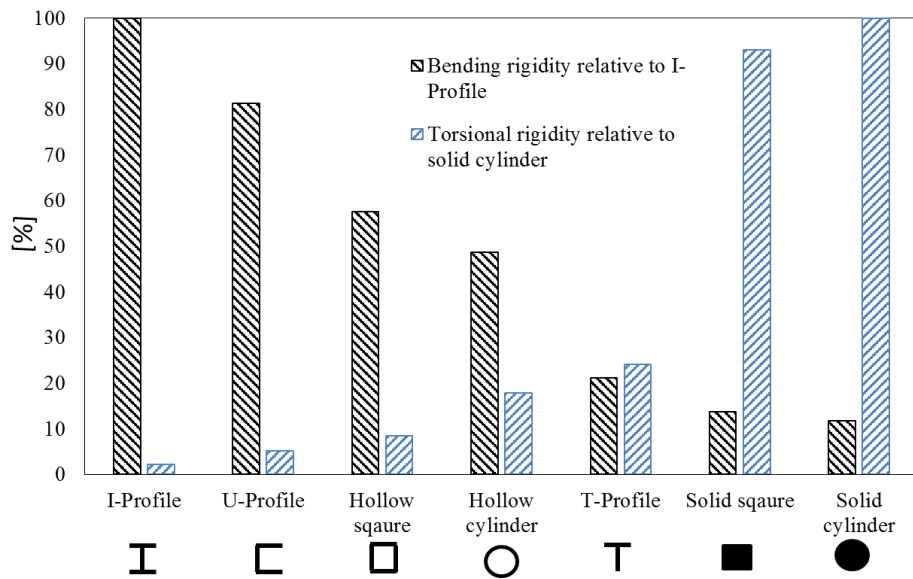


Figure 7.4: Relative bending and torsional rigidity for different shape [83].

‘I’ shape has lowest torsional rigidity relative to solid cylinder and highest bending rigidity relative to all described shapes. Considering both facts, connector is designed in double ‘I’ shape and it is connected to the blade as shown in Figure 7.5(a). A complete dimension of the connector is shown in Figure 7.5(b).

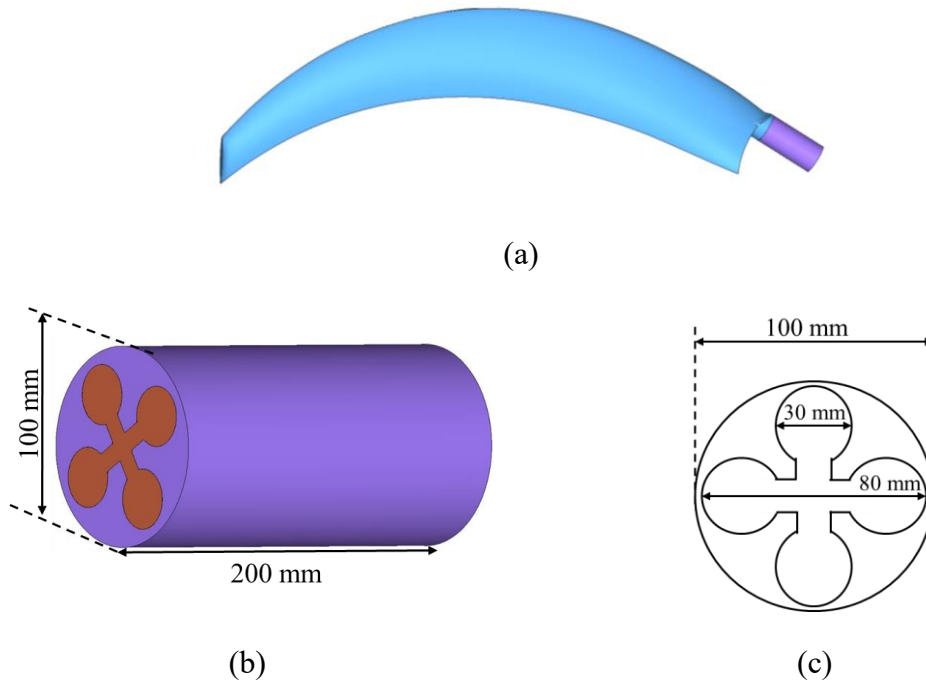


Figure 7.5: (a) An assembly of connector and blade, Material of purple zone is same as blade and material of saffron zone is new composite material designed for connector (b) Height and diameter of connector, (c) Dimension of double I-shape used for connector design.

The material data used for the connector is presented in Table 7.1. The material data for the composite is created using the general rule of mixtures. The material data of composite is designed in such way that blade with and without connector deform by same amount for 5m/s inflow velocity of the water.

Table 7.1: Material data of the connector used for the simulations

Material	Young's Modulus X-direction[MPa]	Young's Modulus Y-direction[MPa]	Young's Modulus Z-direction[MPa]
Blade	1.85e10	1.85e10	1.85e10
Connector	1.06e11	1.80e10	1.80e10
Material	Shear Modulus XY-direction[MPa]	Shear Modulus YZ-direction[MPa]	Shear Modulus ZX-direction[MPa]
Blade	5.12e9	5.12e9	5.12e9
Connector	1.31e9	1.31e9	1.31e9

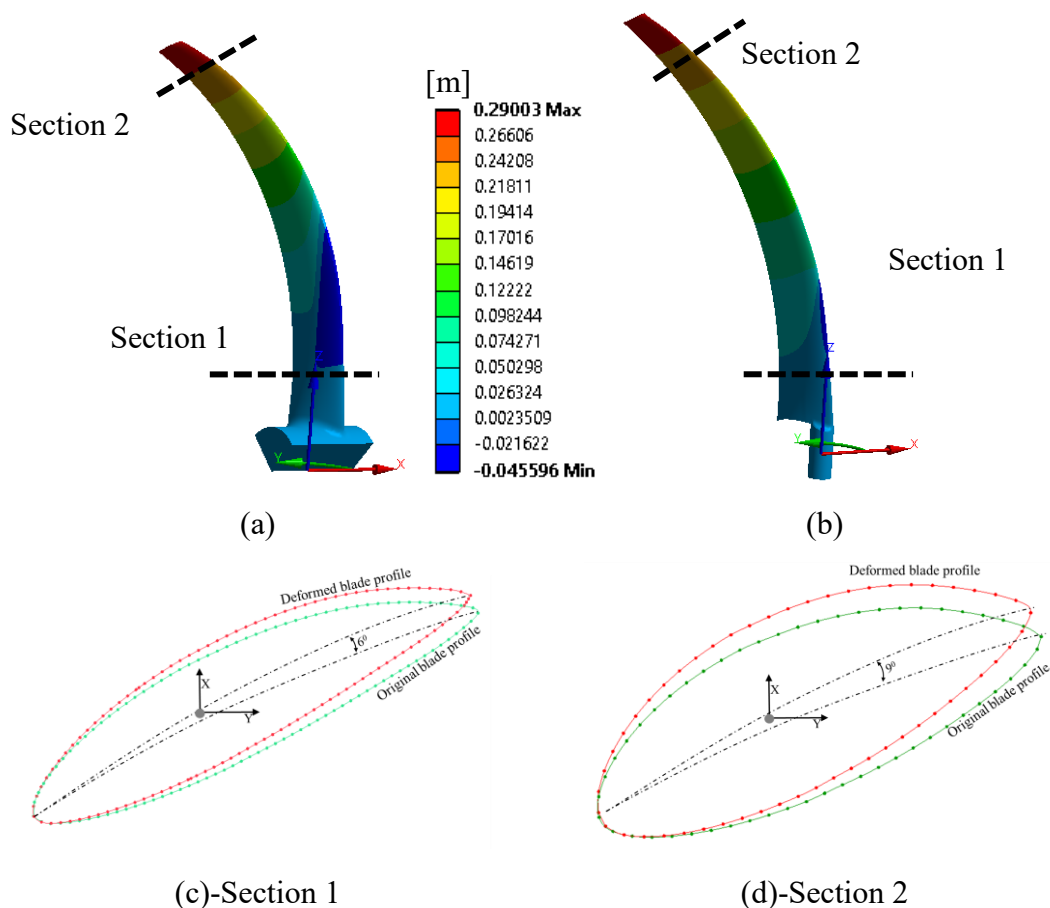


Figure 7.6: Deformation in the flow direction (a) for the original blade, (b) for the blade with a connector. A passive pitch change in airfoil taken (c) from the bottom of the blade and (d) from the tip of the blade.

The deformation for both blades are 30 cm for 5 m/s inflow velocity as presented in Figure 7.6 (a), (b). It is observed that pitch of the blade changes significantly. The blade has six degree pitch at the bottom (Figure 7.6(c)) and nine degree pitch at the tip (Figure 7.6(d)) of the blade.

The change in pitch angle with respect to dimensionless distance from the center of the hub is plotted in Figure 7.7. The connector is twisted by 6 degree over its length. This passive pitch reduces the blade angle for given inflow condition (5 m/s). This cause reduction in thrust value up to 12 percent as plotted in Figure 7.8. The reduction in thrust will reduce the deformation and stress at high inflow velocity.

At lower inflow velocities, connector is not twisting much and change in blade angle is insignificant. Thus reduction in power change because of connector at lower velocity will be same like previous. The tailoring of blade using anisotropic material behavior of composite is achieved and implemented for tidal-turbines blades.

The presented novel idea can be investigated further by FSI. The strategy for the bi-directional FSI is presented in previous section and this could be used as a tool for 3D tailoring of the composite blade and connector.

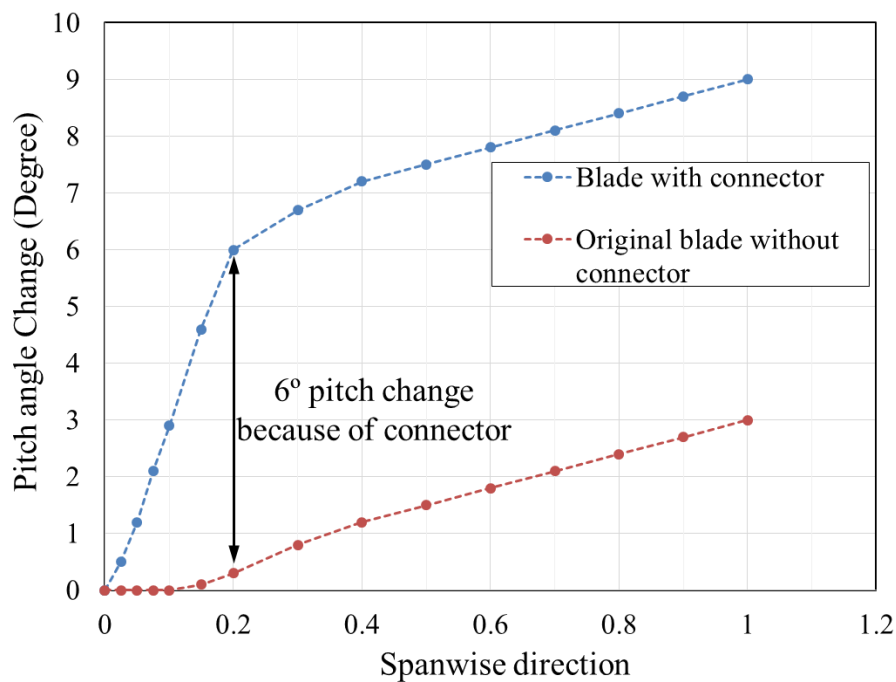


Figure 7.7: Span wise pitch angle change of the blade with and without connector at 5 m/s inflow velocity

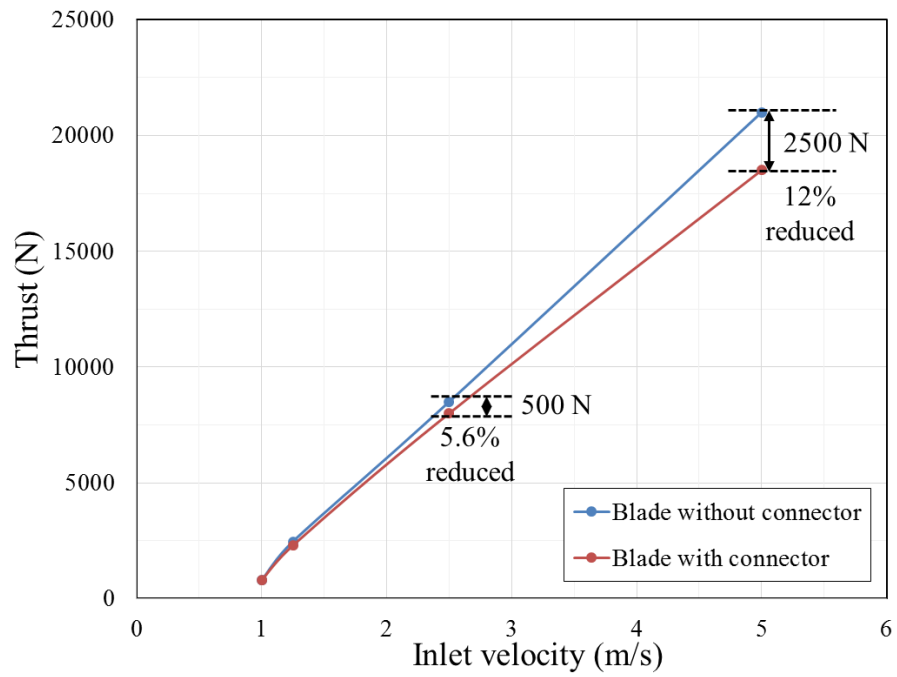


Figure 7.8: Thrust reduction on the blade at different inflow velocity using connector.

8 conclusion

A stable implicit partitioned approach is investigated for fluid-structure interaction involving large deformation. Experimentally validated numerical setups in CFD and FEM solver are created for reliable FSI simulations. A comprehensive study of flexible composite blades of mixer and tidal-turbine is conducted for accurate conclusion.

After an extensive CFD simulations, it has been observed that thrust and torque vary with different turbulence models settings. The SST turbulence model with Gamma-Theta transition model calculates thrust and torque value nearest to experimental results. The dimensionless wall distance ' y^+ ' should be less than one, which is essential parameter for accurate prediction of thrust, torque and transition points. It is important to note that flow is not fully turbulent or neither fully laminar over the blade surface, therefore the transition model has least deviation from the experimental results than other turbulence model settings. For a CFD analysis, rotor-stator domains are defined following state of the art. To ensure accuracy of the results, hex grid mesh is used for simulations.

A swirl jet flow behind the mixer blade in the simulations are matching to theoretical understanding of the flow behind the propeller, like hub delay and velocity profiles in axial, radial, and circumferential directions. It is observed that velocity decreases significantly with axial distance from the mixer blade and it became unchanged later when the hub delay disappears. For the tidal-turbine, similar procedure is followed like the mixer blade simulations but with different boundary conditions. The numerically calculated coefficient of power and torque versus tip-speed ratio are matching to normal behavior of the turbines. Thrust on the turbine increases linearly with increase in inlet velocity. At inlet velocity 5 m/s, thrust is about 21000 N and it may cause permanent failure of blade. At tip-speed ratio equal to five, the turbine is extracting maximum power.

A detailed FEM modelling of the layered composite blade is performed to create correct numerical input data for FSI simulations. A microscopic study is carried out to determine the layered thickness and fiber orientation for each single layer. In numerical

model, 8-node solid elements are used to create mesh for each single layer and 10 micron gap is maintained uniformly between consecutive layers to account glued contact. The discrete cohesive zone model is applied for glue modelling. The non-linear material property of the mixer blade is determined and further validated by using Vic-3D experimental technique. For the tidal-turbine same procedure is followed but its blade is made of random-oriented carbon-fiber reinforced composites without any layered setup. So, hex grid dominant mesh is used and isotropic material data is defined for tidal-turbine simulations.

FEM modelling without fracture modelling of composite is incomplete. The Tsai-Wu, Puck and LaRC criteria are written as in house code and implemented in ANSYS APDL for instant fracture prognostic. The written criteria are used for probes to detect the fracture onset. Furthermore all analysis results are validated by experimental destructive tests. Criteria are validated for tensile and bending failure. Tsai-Wu criterion is appropriate for predicting the location of fracture but not the type of fracture and associated reasons. Puck and LaRC criteria are similar and they are able to separate fiber failure and inter-fiber failure. LaRC is comparatively better than other two criteria because it consider misalignment plane and kinking phenomena for compressive criterion. All mentioned criteria can be applied for fracture analysis of the composites. It is important to note that more experimental analysis are required to validate compressive and load dependent matrix failure.

The CFD numerical setting and FEM modelling with material model are defined for FSI simulations to estimate blade deformation in real applications. Initially, uni-directional FSI is modelled and simulated. It is calculating 58 mm of the total deformation at the tip of the blade. This large deformation was sufficient to justify that bi-directional fluid-structure interactions is important for the flexible composite blade, as it can change the local flow field, thrust and torque values. The layered modelling of the blade facilitate the researcher to understand the tensile and compressive stress distribution for each single layer. It is observed that the stress concentration zones are near to hub side of the blade. In similar way, uni-directional FSI is performed for the tidal-turbine blades. For 2.5 m/s inlet velocity, blade is deforming by 20 cm at blade tip, which is distinctively large deformation. Also in this case, the stress concentration zones are near to hub side of the

blade. The large deformation of the blades in uni-directional FSI push the research to simulate bi-directional FSI.

A transient bi-directional iterative implicit modelling and simulation for fluid-structure interaction is achieved for large deformation of the composite blades using a mesh deformation and re-meshing method. 50 mm deformation is observed in bi-directional FSI, which is 14 percent lesser than the deformation calculated in uni-directional FSI. A large deformation changes the pitch angle and pressure distribution onto the blade surface significantly. This causes reduction in thrust value. So as a result, the deformation reduces. The changes in its pitch angle is up to 3 degree. The change in pitch angle reduces the angle of attack on the blade which results reduction of thrust up to 1872 N from 2130 N for each blade. The final thrust estimated in bi-directional FSI is 12 percent lesser that the thrust estimated in uni-directional FSI

As an application, efficient FSI simulation technique involving large deformations and composite material modelling technique with fracture code are used together as a tool to find the possibilities for the thrust reduction of tidal turbine blades at 5 m/s inlet velocity. Large deformations can be controlled by adding composite connector between blade and hub. At higher inlet velocity, thrust goes up but also moment of blade about its axis increases. So, increase in moment is used to pitch the blade by the help of connector. For the tidal-turbine blade with connector, six and nine degree pitch are achieved at the bottom and the tip of the blade respectively for 5 m/s inlet velocity. The pitch of the blade reduced thrust by 12 percent. Thus, it will reduce the stresses and delay the fractures of the blade.

Now, numerical modelling techniques are investigated for FSI simulation, which could be used for other turbo-machinery systems. Even bi-directional FSI simulations are computationally expensive, but prior information about deformation and final thrust value using FSI calculations will help significantly in blade designs process in terms of reliability and safety. The idea of connector of composite material for passive pitch control is realized using FSI to improve reliability of flexible blade during real applications.

9 outlook

In current fluid-structure simulations, total Lagrangian approach is used in structural solver and inertia of structure is not considered during simulations. Only stiffness of structure is taken into account. Thus, dynamic response of structure is not investigated. For this velocity and accelerations must be mapped together with structural deformations. Implicit FSI approach can be used to investigate dynamic response of the flexible blade. This is considered as a future study. Added mass instability for FSI simulations will not be an issue here as density of composite blade is much higher than density of water [84].

A comprehensive modelling of turbo-machines also includes a rotor-dynamic analysis of the system for stability prediction. But FSI simulation with rotor-dynamic analysis is still not yet done, which will be common practice in near future to understand transient system behavior of turbomachines in real application. It is observed that the bi-directional FSI is computationally expensive. The CFX-solver takes huge CPU time for a small simulation time step. Thus it can be stated that FSI with rotor-dynamic analysis would be more computationally expensive. Moreover, a common platform for simultaneous simulations of both type of analysis are required.

A bond graph methodology is one of the best technique to create a model for engineering system [85]–[88]. This methodology is based on energy transfer between two domains and system causality [89]. Kumar et.al have been done preliminary work to understand modelling capability using a bond graph [90]. A propeller blade has been modelled based on Rayleigh beam model having 6 degree of freedom. Added mass, gravity and time dependent CFD load are not incorporated in the integrated bond graph model. Further improvement in bond graph model for each mechanical component is considered as a future work.

To get CFD force on the propeller blade quickly, a vortex lattice method could be appropriate substitute for dynamic fluid simulations rather than ANSYS CFX solver. The Quasi-VLM in thin wing theory is first presented by Lan in 1974 [91]. VLM solves the

potential flow around a propeller by placing discrete vortices and sources on the blade camber surface and its trailing wake surface. Numerous studies are published for further investigation on VLM and its application for steady and unsteady performance of marine propellers [92]–[94]. The time dependent CFD forces can be used as input in rotor-dynamic analysis. So the development of in house code for VLM to predict the fluid forces is also considered as a future work.

So rotor-dynamic analysis of the rotating system including the fluid forces computed by VLM method will significantly reduce the computational time. This will enable researches or engineers to perform parametric study of rotating system for optimization in a small amount of time.

ibliography

- [1] G. Kuiper, “ Aviation Research and Rhip ropeller Design,” *Appl. Sci. Res.*, vol. 58, pp. 33–50, 1998.
- [2] E.-J. Foeth, T. van Terwisga, and . van Doorne, “ n the ollapse Structure of an Attached Cavity on a Three-Dimensional Hydrofoil,” *J. Fluids Eng.*, vol. 130, no. 071303, pp. 1–9, 2008.
- [3] T. van Terwisga, E. van Wijngaarden, J. osschers, and G. Kuiper, “Achievements and hallenges in Aviation Research on Ship ropellers,” *Int. Shipbuild. Prog.*, vol. 54, pp. 165–187, 2007.
- [4] V. accese, K. H. Light, and K. A. erube, “ Aviation erosion resistance of various material systems,” *Ships Offshore Struct.*, vol. 1, no. 4, pp. 309–322, 2006.
- [5] A. . Mouritz, E. Gellert, . urchill, and K. hallis, “Review of advanced composite structures for naval ships and submarines,” *Compos. Struct.*, vol. 53, no. 1, pp. 21–42, Jul. 2001.
- [6] Y. Ashkenazi, I. Gol’fman, L. Rezhkov, and N. Sidorov, *Glass-Fiber-Reinforced Plastics Parts in Ship Machinery*. Sudostroyenniye Publishing House, Leningard, 1974.
- [7] . Kane and R. Dow, “Marine propulsors design in fibre reinforced plastics,” *J. Def. Sciense*, no. 4, pp. 301–308, 1994.
- [8] T. Searle and D. Shot, “Are composite propellers the way forward for small boats,” *J. Inst. Mater. 2*, vol. 2, pp. 69–70, 1994.
- [9] J. F. Manwell, J. G. McGowan, and A. L. Rogers, *Wind Energy*. Wiley, Chichester, 2002.
- [10] . rondsted, H. Lilholt, and A. Lystrup, “ omposite materials for wind power turbine blades,” *Annu. Rev. Mater. Res.*, no. 35, pp. 505–538, 2005.

-
- [11] R. Ganguli and I. Chopra, "Aeroelastic Tailoring of Composite Couplings and Blade Geometry of a Helicopter Rotor Using Optimization Methods," *J. Am. Helicopter Soc.*, vol. 42, no. 3, pp. 218–228, 1997.
- [12] J. Lasques, S. Egggreen, and S. Andersen, "Hydro-elastic analysis and optimization of a composite marine propeller," *Mar. Struct.*, vol. 23, no. 1, pp. 22–38, 2010.
- [13] M. R. Motley and Y. L. Young, "Influence of uncertainties on the response and reliability of self-adaptive composite rotors," *Compos. Struct.*, vol. 94, no. 1, pp. 114–120, 2011.
- [14] WIL SE, "Group Research and Technology," 2014. [online]. Available: <http://www.wilo.com/products-competences/drainage-and-sewage/#acc28795>.
- [15] S. Petersson, M. Larson, and L. Jönsson, "Development of a turbulent jet generated by a mixer in weak co-flow and counter-flow," *Int. J. Heat Fluid flow*, no. 21, pp. 1–10, 2000.
- [16] M. Sieg, F. Hüttmann, and A. Leder, "Experimental characterisation of unconfined swirling jets," in *Lasermethoden in der Strömungsmesstechnik*, 2009.
- [17] M. Sieg, "Verdrallter Freistrahler - Ein Ähnlichkeitsansatz zur allgemeinen Beschreibung des Strömungs- und Turbulenzfeldes axialsymmetrischer Freistrahler," PhD. Dissertation, University of Rostock, 2012.
- [18] S. Von Hörsten, M. Sieg, F. Hüttmann, and A. Leder, "Bestimmung von Rührwerksbeiwerten – Vergleich zwischen Geschwindigkeits- und Kraftmessungen," *tm-Technisches Mess.*, vol. 79, pp. 310–317, 2012.
- [19] S. Von Hörsten, J. Wenzlaff, F. Hüttmann, and A. Leder, "Verwendung der Selbstähnlichkeit verdrallter Freistrahler zur BLACK BOX Modellierung von Rührwerken," in *Lasermethoden in der Strömungsmesstechnik*, 2012.
- [20] S. Von Hörsten, "Experimentelle und numerische Untersuchungen an verdrallten Frei- und Prallstrahlern: Untersuchungen zum Ähnlichkeitsverhalten und zur Black Box Modellierung von Propellerrührwerken," PhD. Dissertation, University of Rostock, 2013.

-
- [21] F. Tian, W. Shi, Q. Zhang, D. Zhang, and G. Zhang, "Inner flow characteristics at impeller of submersible mixer with two blades," *J. Jiangsu Univ.*, no. 34, pp. 395–398, 2013.
- [22] X. Weixing, Y. Jianping, and A. . Equations, "Optimization Design of Submersible Mixer based on Simulation Study of Agitated Flow Field," *2011 Third Int. Conf. Meas. Technol. Mechatronics Autom.*, pp. 807–810, Jan. 2011.
- [23] J. Kumar, F. H. Wurm, and H. Sura, "Effect of mixer blade geometry and deformation on jet flow shape and sedimentation in sewage application," in *International Rotating Equipment Conference*, 2012, pp. 518–527.
- [24] J. Kumar and F. H. Wurm, "Bi-directional fluid – structure interaction for large deformation of layered composite propeller blades," *J. Fluids Struct.*, vol. 57, pp. 32–48, 2015.
- [25] J. H. Lee, S. Park, D. H. Kim, S. H. Rhee, and M.- . Kim, "Computational methods for performance analysis of horizontal axis tidal stream turbines," *Appl. Energy*, vol. 98, pp. 512–523, Oct. 2012.
- [26] T. . Lloyd, S. R. Turnock, and V. F. Humphrey, "Assessing the influence of inflow turbulence on noise and performance of a tidal turbine using large eddy simulations," *Renew. Energy*, vol. 71, pp. 742–754, Nov. 2014.
- [27] D. M. Grogan, S. . Leen, . R. Kennedy, and . M. Ó rádaigh, "Design of composite tidal turbine blades," *Renew. Energy*, vol. 57, pp. 151–162, Sep. 2013.
- [28] S. Klinkel, F. Gruttmann, and W. Wagner, "A continuum based three-dimensional shell element for laminated structures," *Comput. Struct.*, vol. 71, no. 1, pp. 43–62, Mar. 1999.
- [29] R. A. S. Moreira, R. J. Alves de Sousa, and R. A. F. Valente, "A solid-shell layerwise finite element for non-linear geometric and material analysis," *Compos. Struct.*, vol. 92, no. 6, pp. 1517–1523, May 2010.
- [30] H. Naceur, S. Shiri, D. outellier, and J. L. atoz, "On the modeling and design of composite multilayered structures using solid-shell finite element model," *Finite Elem. Anal. Des.*, vol. 70–71, pp. 1–14, Aug. 2013.

-
- [31] A. . eireira and A. . de Morais, “Mixed mode I+II interlaminar fracture of carbon/epoxy laminates,” *Compos. Part A Appl. Sci. Manuf.*, vol. 39, no. 2, pp. 322–333, Feb. 2008.
- [32] A. . de Morais, “Mode I cohesive zone model for delamination in composite beams,” *Eng. Fract. Mech.*, vol. 109, pp. 236–245, Sep. 2013.
- [33] M. J. Hinton, A. S. Kaddour, and . D. Soden, “A comparison of the predictive capabilities of current failure theories for composite laminates, judged against experimental evidence,” *Compos. Sci. Technol.*, vol. 62, no. 12–13, pp. 1725–1797, Sep. 2002.
- [34] A. S. Kaddour, M. J. Hinton, and . D. Soden, “A comparison of the predictive capabilities of current failure theories for composite laminates: additional contributions,” *Compos. Sci. Technol.*, vol. 64, no. 3–4, pp. 449–476, Mar. 2004.
- [35] R. G. untze and A. Freund, “The predictive capability of failure mode concept-based strength criteria for multidirectional laminates,” *Compos. Sci. Technol.*, vol. 64, no. 3–4, pp. 343–377, Mar. 2004.
- [36] S. T. inho, . G. Dávila, . . amanho, L. Iannucci, and . Robinson, “Failure Models and Criteria for FRP Under In-Plane or Three-Dimensional Stress States Including Shear Non-Linearity,” 2005.
- [37] S. K. Chakrabarti, *Numerical models in Fluid-Structure Interaction*. 2005.
- [38] J. Kumar and F. H. Wurm, “Methoden zur Modellierung von Fluid-Struktur-Wechselwirkungen,” in *AK Strömungsmaschinen*, 2014.
- [39] . Hübner, E. Walhorn, and D. Dinkler, “A monolithic approach to fluid–structure interaction using space–time finite elements,” *Comput. Methods Appl. Mech. Eng.*, vol. 193, no. 23–26, pp. 2087–2104, Jun. 2004.
- [40] . . Ryzhakov, R. Rossi, S. R. Idelsohn, and E. ña te, “A monolithic Lagrangian approach for fluid–structure interaction problems,” *Comput. Mech.*, vol. 46, no. 6, pp. 883–899, Aug. 2010.
- [41] K. . ark, “artitioned Transient Analysis rocedures for oupled-Field roblems: Stability Analysis,” *J. Appl. Mech.*, vol. 47, no. 2, 1980.

-
- [42] . A. Felippa and T. L. Geers, “Partitioned analysis of coupled mechanical systems,” *Eng. Comput.*, vol. 5, no. 2, pp. 123–133, 1988.
- [43] K. . ark, . Fellipa, and R. ha yon, “Partitioned formulation of internal fluid–structure interaction problems by localized Lagrange multipliers,” *Comput. Methods Appl. Mech. Eng.*, vol. 190, pp. 2989–3007, 2001.
- [44] X. hen, M. Schäfer, and D. othe, “Numerical modeling and investigation of viscoelastic fluid–structure interaction applying an implicit partitioned coupling algorithm,” *J. Fluids Struct.*, vol. 54, pp. 390–421, 2015.
- [45] J. P. Morand and R. Ohayon, *Fluid-Structure Interaction: Applied Numerical Methods*. 1995.
- [46] H. Lin and J. Lin, “Nonlinear hydroelastic behavior of propellers using a finite element method and lifting surface theory,” *J. Mar. Sci. Technol.*, pp. 114–124, 1996.
- [47] H. Lin and J. Lin, “Effect of stacking sequence on the hydroelastic behavior of composite propeller blades,” in *Eleventh International Conference on Composite Materials, Australian Composite Structures Society, Gold Coast, Australia.*, 1997.
- [48] . Le Tallec and J. Mouro, “Fluid structure interaction with large structural displacements,” *Comput. Methods Appl. Mech. Eng.*, vol. 190, no. 24–25, pp. 3039–3067, Mar. 2001.
- [49] P. Le Tallec, J.-F. Gerbeau, . Hauret, and M. Vidrascu, “Fluid structure interaction problems in large deformation,” *Comptes Rendus Mécanique*, vol. 333, no. 12, pp. 910–922, Dec. 2005.
- [50] F. K. enra, “Numerical and experimental investigation on the flow induced oscillations of a single-blade pump impeller,” *J. Fluids Eng.*, vol. 128, no. 4, pp. 783–793, 2005.
- [51] Y. L. Young, “Fluid–structure interaction analysis of flexible composite marine propellers,” *J. Fluids Struct.*, vol. 24, no. 6, pp. 799–818, Aug. 2008.
- [52] R. L. ampbell and E. G. aterson, “Fluid–structure interaction analysis of flexible turbomachinery,” *J. Fluids Struct.*, vol. 27, no. 8, pp. 1376–1391, Nov. 2011.

-
- [53] M.-C. Hsu and Y. Bazilevs, “Fluid–structure interaction modeling of wind turbines: simulating the full machine,” *Comput. Mech.*, vol. 50, no. 6, pp. 821–833, Aug. 2012.
- [54] G. De Nayer and M. Heuer, “Numerical FSI investigation based on LES: Flow past a cylinder with a flexible splitter plate involving large deformations (FSI-PfS-2a),” *Int. J. Heat Fluid Flow*, Sep. 2014.
- [55] F. M. White, *Fluid Mechanics*, 6th revise. McGraw Hill Higher Education, 2006.
- [56] B. Lakshminarayana, *Fluid dynamics and Heat transfer of Turbomachinery*. John Wiley & Sons, Inc, 1996.
- [57] D. C. Wilcox, *Turbulence Modeling for CFD*. Griffin Printing, Glendale California, 1994.
- [58] J. Boussinesq, “Essai sur la théorie des eaux courantes,” *Mém. présentés par Divers savants à l’Acad. Sci.*, no. 23, pp. 1–680, 1877.
- [59] F. R. Menter, “Zonal Two Equation k- ϵ Turbulence Models for Aerodynamic Flows,” *Am. Inst. Aeronaut. Astronaut.*, vol. 93–2906, 1993.
- [60] F. R. Menter, M. Kuntz, and R. Langtry, “Ten Years of Industrial Experience with the SST Turbulence Model,” *Turbul. Heat Mass Transf. 4*, vol. 4, pp. 625–632, 2003.
- [61] F. R. Menter, T. Esch, and S. Kubacki, “Transition Modelling based on Local Variables,” in *5th International Symposium on Turbulence Modeling and Measurements*, 2002.
- [62] R. B. Langtry and F. R. Menter, “Transition Modeling for General CFD Application in Aeronautics,” *AIAA Aerosp. Sci. Meet. Exhib.*, no. January, pp. 1–14, 2005.
- [63] J. N. Reddy, *An introduction to the finite element method*, 3rd ed. McGraw-Hill, 2006.
- [64] D. Xie, M. Garg, D. Huang, and F. Abdi, “Cohesive Zone Model for Surface Cracks Using Finite Element Analysis,” *49th AIAA/ASME/ASCE/AHS/ASC Struct. Struct. Dyn. Mater. Conf.*, pp. 1–16, Apr. 2008.

-
- [65] . D. Soden, M. J. Hinton, and A. S. Kaddour, “A MAR IS N F THE PREDICTIVE CAPABILITIES OF CURRENT FAILURE THEORIES FOR M S ITE LAMINATES,” vol. 58, 1998.
- [66] I. I. Gol'denblat and V. A. Kopnov, “Strength of glass-Reinforced Plastics in the omplex Stress State,” in *Polymer Mechanics*, vol. 1, 1966, p. 54.
- [67] S. W. Tsai and E. M. Wu, “A General Theory of Strength for Anisotropic Materials,” *J. Compos. Mater.*, vol. 5, p. 58, 1971.
- [68] A. uck and H. Schürmann, “Failure analysis of FR laminates by means of physically based phenomenological models,” *Compos. Sci. Technol.*, vol. 62, no. 12–13, pp. 1633–1662, 2002.
- [69] A. uck, J. Kopp, and M. Knops, “Guidelines for the determination of the parameters in uck’s action plane strength criterion,” *Compos. Sci. Technol.*, vol. 62, pp. 371–378, 2002.
- [70] A. Puck and W. Schneider, “ n failure mechanisms and failure criteri of filament-wound glass-fibre/resin composites,” *Plast. Polym.*, pp. 33–34, 1969.
- [71] M. Knops, *Analysis of failure in fiber polymer laminates*. 2008.
- [72] G. J. Dvorak and N. Laws, “Analysis of rog resive matrix cracking in composite laminates II:-Firts ly Failure,” *J. Compos. Mater.*, no. 21, 1987.
- [73] V. W. Rosen, “Mechanics of composite strengthening,” in *Fiber Composite Materials American Society of Metals, Metal Park, Ohio*, 1965, pp. 102–106.
- [74] Ansys, “Ansys help manual.”
- [75] ANSYS FX erlin, “Numerische erechnung von Rührwerkströmungen und Erstellung eines zugehörigen Best- ractice Guide,” 2007.
- [76] R. E. Mayle, “The role of laminar-turbulent transition in gas turbine engines,” *J. Turbomach.*, no. 113, pp. 509–536, 1991.
- [77] J. Jeong and F. Hussain, “ n the identification of a vortex,” *J. Fluid Mech.*, vol. 285, no. -1, p. 69, 1995.
- [78] Schottel GmbH, “Research & development center, Schottel,” 2012.

-
- [79] E. Hau, “etz’s elementary Momentum Theory,” in *Wind turbines*, pp. 81–91.
- [80] MatWeb LL, “omposite material data.” [nline]. Available: www.matweb.com.
- [81] orrelated Solutions, “Vic-3D Technique.” [nline]. Available: <http://www.correlatedsolutions.com/vic-3d/>.
- [82] S. Hallier, “Entwicklung einer passiven itchregelung einer Wassturbine mittels numerischer Simulation unter Berücksichtigung der Fluid-Structure-Interaction,” Master Thesis, University of Rostock, 2012.
- [83] G. Erhard, *Konstruieren mit Kunststoffen*. München: Carls Hanser Verlag, 2008.
- [84] . Förster, W. A. Wall, and E. Ramm, “Artificial added mass instabilities in sequential staggered coupling of nonlinear structures and incompressible viscous flows,” *Comput. Methods Appl. Mech. Eng.*, vol. 196, pp. 1278–1293, 2007.
- [85] H. M. Paynter, *Analysis and Design of Engineering Systems*. M.I.T. Press, Cambridge, 1961.
- [86] D. C. Karnopp, D. L. Margolis, and R. C. Rosenberg, *System Dynamics: A Unified Approach*. John Wiley & Sons Inc, 1975.
- [87] A. J. Blundell, *Bond Graphs for Modelling Engineering Systems*. Ellis Horwood Publishers, 1982.
- [88] J. J. eaman and . . reedveld, “hysical Modeling With Eulerian Frames and ond Graphs,” *J. Dyn. Syst. Control*, vol. 110, no. 2, p. 7, 1988.
- [89] A. Mukerjee and R. Karmakar, “Modelling and simulation of engineering systems through bondgraphs,” *Alpha Sci. Int’l Ltd*, 2000.
- [90] J. Kumar, A. Lass, and F. -H. Wurm, “omprehensive modelling of flexible rotor blade and its power train,” in *Deutscher Luft-Und RaumfahrtKongress*, 2015.
- [91] . E.Lan, “A Quasi-Vortex-Lattice Method in Thin Wing Theory,” *J. Aircr.*, no. 11(9), pp. 518–527, 1974.

- [92] J. E. Kerwin and J. E. Lee, “Prediction of Steady and Unsteady Marine Propeller Performance by Numerical Lifting-Surface Theory,” in *The Society of Naval Architects and marine Engineers* -36, 1978.
- [93] D. A. Greely and J. E. Kerwin, “Numerical methods for propeller design and analysis in steady flow,” in *The Society of Naval Architects and marine Engineers*-90, 1982.
- [94] H. Lei and S. A. Kinnas, “A Vortex-Lattice Method for the prediction of Unsteady performance of Marine Propellers and Current Turbines,” *Int. J. Offshore Polar Eng.*, vol. 23, no. 3, pp. 210–217, 2013.

Appendices

A. Tsai-Wu failure criteria

A.1. Criterion Derivation

Considering all strength tensor of an irregular body, the non-failure criterion could be written as Eq.(67).

$$(f_i \sigma_i)^\alpha + (f_{ij} \sigma_i \sigma_j)^\beta + (f_{ijk} \sigma_i \sigma_j \sigma_k)^\gamma + \dots \leq 1 \quad (67)$$

Here, f_i, f_{ij} and f_{ijk} are the strength tensors, α, β and γ are the material constants and i, j and $k = 1, 2 \dots 6$

Based on the various experiments, Tsai-Wu modified the criterion by neglecting the 3rd order stress tensor terms. Moreover, $\alpha = 1, \beta = 1$ is considered based on the best fit to the experimental data. So, Tsai-Wu criterion for non-failure is given in Eq.(68)

$$f_i \sigma_i + f_{ij} \sigma_i \sigma_j \leq 1 \quad (68)$$

An expended form of the Eq.(68) is written below in form of Eq.(69)

$$\begin{aligned} & f_1 \sigma_1 + f_2 \sigma_2 + f_3 \sigma_3 + f_4 \sigma_4 + f_5 \sigma_5 + f_6 \sigma_6 \\ & + f_{11} \sigma_1^2 + 2f_{12} \sigma_1 \sigma_2 + 2f_{13} \sigma_1 \sigma_3 + 2f_{14} \sigma_1 \sigma_4 + 2f_{15} \sigma_1 \sigma_5 \\ & \quad + 2f_{16} \sigma_1 \sigma_6 \\ & + f_{22} \sigma_2^2 + 2f_{23} \sigma_2 \sigma_3 + 2f_{24} \sigma_2 \sigma_4 + 2f_{25} \sigma_2 \sigma_5 + 2f_{26} \sigma_2 \sigma_6 \\ & + f_{33} \sigma_3^2 + 2f_{34} \sigma_3 \sigma_4 + 2f_{35} \sigma_3 \sigma_5 + 2f_{36} \sigma_3 \sigma_6 \\ & + f_{44} \sigma_4^2 + 2f_{45} \sigma_4 \sigma_5 + 2f_{46} \sigma_4 \sigma_6 \\ & + f_{55} \sigma_5^2 + 2f_{56} \sigma_5 \sigma_6 \\ & + f_{66} \sigma_6^2 \leq 1 \end{aligned} \quad (69)$$

Here, σ_1, σ_2 and σ_3 are normal stress terms and σ_4, σ_5 and σ_6 are shear terms.

Now, for an orthotropic material with three planes of symmetry, which are oriented with the coordinate directions, if we assume that there is no coupling between the normal and shear stress terms (and between the shear terms), the general form of the Tsai–Wu failure criterion can be expressed as Eq. (70)

$$\begin{aligned} f_1\sigma_1 + f_2\sigma_2 + f_3\sigma_3 + f_4\sigma_4 + f_5\sigma_5 + f_6\sigma_6 + 2f_{12}\sigma_1\sigma_2 + 2f_{13}\sigma_1\sigma_3 \\ + 2f_{23}\sigma_2\sigma_3 + f_{11}\sigma_1^2 + f_{22}\sigma_2^2 + f_{33}\sigma_3^2 + f_{44}\sigma_4^2 \\ + f_{55}\sigma_5^2 + f_{66}\sigma_6^2 \leq 1 \end{aligned} \quad (70)$$

Tensile and compressive failure strength in all three directions can be represented as $\sigma_{1t}, \sigma_{2t}, \sigma_{3t}, \sigma_{1c}, \sigma_{2c},$ and σ_{3c} .

Shear failure strengths can be represented as $\tau_{12}, \tau_{13}, \tau_{21}, \tau_{23}, \tau_{31},$ and τ_{32} , where

$$\tau_{12} = \tau_{21}; \tau_{32} = \tau_{23}; \tau_{13} = \tau_{31};$$

Under uniaxial load case, a resulting equation can be written as Eq.(71) and Eq.(72)

$$f_1\sigma_{1t} + f_{11}\sigma_{1t}^2 = 1 \quad (71)$$

$$f_1\sigma_{1c} + f_{11}\sigma_{1c}^2 = 1 \quad (72)$$

The simultaneous solution of above equations lead to value of the coefficients, which are presented in Eq.(73)-Eq.(76)

$$f_1 = \frac{1}{\sigma_{1t}} - \frac{1}{\sigma_{1c}}; f_{11} = \frac{1}{\sigma_{1t}\sigma_{1c}} \quad (73)$$

$$f_2 = \frac{1}{\sigma_{2t}} - \frac{1}{\sigma_{2c}}; f_{22} = \frac{1}{\sigma_{2t}\sigma_{2c}} \quad (74)$$

$$f_3 = \frac{1}{\sigma_{3t}} - \frac{1}{\sigma_{3c}}; f_{33} = \frac{1}{\sigma_{3t}\sigma_{3c}} \quad (75)$$

$$f_4 = f_5 = f_6 = 0 \quad (76)$$

$$f_{44} = \frac{1}{\tau_{23}^2}; f_{55} = \frac{1}{\tau_{31}^2}; f_{66} = \frac{1}{\tau_{12}^2}$$

f_{12}, f_{23} and f_{31} can be obtained by a biaxial load test, which is impractical to perform. So, Tsai-Wu introduced the stability conditions. He stated that all diagonal terms must be positive and off diagonal terms could be negative or positive. The magnitude of interacting terms are constrained by in-equality as shown in Eq.(77)-Eq.(79).

$$f_{ii}f_{jj} - f_{ij}^2 \geq 0 \quad (77)$$

$$2f_{12} = C_{12}\sqrt{f_{11}f_{22}}; 2f_{23} = C_{23}\sqrt{f_{22}f_{33}}; f_{31} = 2C_{31}\sqrt{f_{33}f_{11}} \quad (78)$$

$$2f_{12} = \frac{C_{12}}{\sqrt{\sigma_{1t}\sigma_{1c}\sigma_{2t}\sigma_{2c}}}; 2f_{23} = \frac{C_{23}}{\sqrt{\sigma_{2t}\sigma_{2c}\sigma_{3t}\sigma_{3c}}}; 2f_{31} = \frac{C_{31}}{\sqrt{\sigma_{3t}\sigma_{3c}\sigma_{1t}\sigma_{1c}}} \quad (79)$$

The complete criterion can be written as Eq.(80).

$$\begin{aligned} & \left(\frac{1}{\sigma_{1t}} - \frac{1}{\sigma_{1c}}\right)\sigma_1 + \left(\frac{1}{\sigma_{2t}} - \frac{1}{\sigma_{2c}}\right)\sigma_2 + \left(\frac{1}{\sigma_{3t}} - \frac{1}{\sigma_{3c}}\right)\sigma_3 \\ & + \left(\frac{C_{12}}{\sqrt{\sigma_{1t}\sigma_{1c}\sigma_{2t}\sigma_{2c}}}\right)\sigma_1\sigma_2 + \left(\frac{C_{31}}{\sqrt{\sigma_{3t}\sigma_{3c}\sigma_{1t}\sigma_{1c}}}\right)\sigma_1\sigma_3 \\ & + \left(\frac{C_{23}}{\sqrt{\sigma_{2t}\sigma_{2c}\sigma_{3t}\sigma_{3c}}}\right)\sigma_2\sigma_3 + \left(\frac{1}{\sigma_{1t}\sigma_{1c}}\right)\sigma_1^2 + \left(\frac{1}{\sigma_{2t}\sigma_{2c}}\right)\sigma_2^2 \\ & + \left(\frac{1}{\sigma_{3t}\sigma_{3c}}\right)\sigma_3^2 + \left(\frac{1}{\tau_{23}^2}\right)\sigma_4^2 + \left(\frac{1}{\tau_{31}^2}\right)\sigma_5^2 + \left(\frac{1}{\tau_{12}^2}\right)\sigma_6^2 \\ & \leq 1 \end{aligned} \quad (80)$$

Considering negative sign of the compressive stress and, x,y and z for 1,2 and 3, then criterion could be written as Eq.(81)

$$\begin{aligned}
 & \left(\frac{1}{\sigma_{xt}} + \frac{1}{\sigma_{xc}} \right) \sigma_x + \left(\frac{1}{\sigma_{yt}} + \frac{1}{\sigma_{yc}} \right) \sigma_y + \left(\frac{1}{\sigma_{zt}} + \frac{1}{\sigma_{zc}} \right) \sigma_z \\
 & + \left(\frac{C_{xy}}{\sqrt{\sigma_{xt}\sigma_{xc}\sigma_{yt}\sigma_{yc}}} \right) \sigma_x \sigma_y + \left(\frac{C_{zx}}{\sqrt{\sigma_{zt}\sigma_{zc}\sigma_{xt}\sigma_{xc}}} \right) \sigma_x \sigma_z \\
 & + \left(\frac{C_{yz}}{\sqrt{\sigma_{yt}\sigma_{yc}\sigma_{zt}\sigma_{zc}}} \right) \sigma_y \sigma_z - \left(\frac{1}{\sigma_{xt}\sigma_{xc}} \right) \sigma_x^2 - \left(\frac{1}{\sigma_{yt}\sigma_{yc}} \right) \sigma_y^2 \\
 & - \left(\frac{1}{\sigma_{zt}\sigma_{zc}} \right) \sigma_z^2 + \left(\frac{1}{\tau_{yz}^2} \right) \sigma_{yz}^2 + \left(\frac{1}{\tau_{zx}^2} \right) \sigma_{zx}^2 \\
 & + \left(\frac{1}{\tau_{xy}^2} \right) \sigma_{xy}^2 \leq 1
 \end{aligned} \tag{81}$$

The criterion can be separated into two parts A (Eq.(82)) and B (Eq.(83))

$$\begin{aligned}
 A = & - \left(\frac{1}{\sigma_{xt}\sigma_{xc}} \right) \sigma_x^2 - \left(\frac{1}{\sigma_{yt}\sigma_{yc}} \right) \sigma_y^2 - \left(\frac{1}{\sigma_{zt}\sigma_{zc}} \right) \sigma_z^2 + \left(\frac{1}{\tau_{yz}^2} \right) \sigma_{yz}^2 \\
 & + \left(\frac{1}{\tau_{zx}^2} \right) \sigma_{zx}^2 + \left(\frac{1}{\tau_{xy}^2} \right) \sigma_{xy}^2 + \left(\frac{C_{xy}}{\sqrt{\sigma_{xt}\sigma_{xc}\sigma_{yt}\sigma_{yc}}} \right) \sigma_x \sigma_y \\
 & + \left(\frac{C_{zx}}{\sqrt{\sigma_{zt}\sigma_{zc}\sigma_{xt}\sigma_{xc}}} \right) \sigma_x \sigma_z + \left(\frac{C_{yz}}{\sqrt{\sigma_{yt}\sigma_{yc}\sigma_{zt}\sigma_{zc}}} \right) \sigma_y \sigma_z
 \end{aligned} \tag{82}$$

$$B = \left(\frac{1}{\sigma_{xt}} + \frac{1}{\sigma_{xc}} \right) \sigma_x + \left(\frac{1}{\sigma_{yt}} + \frac{1}{\sigma_{yc}} \right) \sigma_y + \left(\frac{1}{\sigma_{zt}} + \frac{1}{\sigma_{zc}} \right) \sigma_z \tag{83}$$

$$\text{Failure index} = A + B$$

$$\text{Failure Index} \leq 1; \text{ Safe}$$

$$\text{Failure Index} \geq 1; \text{ fracture} \tag{84}$$

B. Puck failure criteria

B.1. Criterion Derivation

Puck introduced fiber failure and inter-fiber failure criterion. Puck postulated σ_{\parallel} is responsible for the fiber failure and $\sigma_{\perp}, \tau_{\perp\parallel}$ and $\tau_{\perp\perp}$ are responsible for the inter-fiber failure based on numerous experiments. A complete description of stressing is shown in Figure 3.5(b).

Longitudinal Loading: Fiber failure

Fiber failure basically caused by the tensile and compressive stressing which acts longitudinal to the direction of the fibers as shown in Figure 3.7. Basic equations for fiber tensile and compressive failure are shown in Eq.(33) and Eq.(34). These equations don't need any derivation explanations.

Transverse loading: Inter fiber failure

For the inter fiber-failure, the normal stress σ_n and the shear stress τ_{n1} and τ_{nt} on the fracture plane (θ_{fp}) are decisive for Inter-fiber failure as shown in figure below. These stresses can be obtained by transformation matrix as shown in Eq.(85)

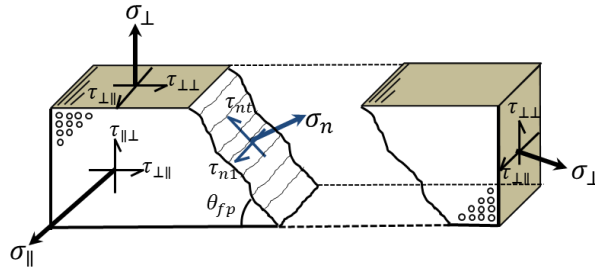


Figure B 1: 3D fracture plane in composites

$$\begin{Bmatrix} \sigma_n(\theta_{fp}) \\ \tau_{nt}(\theta_{fp}) \\ \tau_{n1}(\theta_{fp}) \end{Bmatrix} = \begin{bmatrix} c^2 & s^2 & 2sc & 0 & 0 \\ -sc & sc & (c^2 - s^2) & 0 & 0 \\ 0 & 0 & 0 & s & c \end{bmatrix} \begin{Bmatrix} \sigma_{\perp} \\ \sigma_{\parallel} \\ \tau_{\perp\perp} \\ \tau_{\perp\parallel} \\ \tau_{\parallel\perp} \end{Bmatrix} \quad (85)$$

where, $c = \cos(\theta_{fp})$ and $s = \sin(\theta_{fp})$;

Based on Mohr-Coulomb hypothesis, for the transverse tensile loading, the fracture criterion can be written as Eq.(86). Here R^A is fracture resistance.

$$\left(\frac{\sigma_n}{R^A_{\perp}}\right)^2 + \left(\frac{\tau_{nt}}{R^A_{\perp\perp}}\right)^2 + \left(\frac{\tau_{nl}}{R^A_{\perp\parallel}}\right)^2 = 1 \text{ for } \sigma_n \geq 0 \quad (86)$$

Three modes can be separated in inter-fiber failure, which is explained in section 3.3.2.2 and Figure 3.8.

Mode A:

Based on experimental results, Puck modified the above equation for inter-fiber failure under transverse tensile and shear loading to meet elliptical equation, which is written below in Eq.(87).

$$c \left(\frac{\sigma_n}{R^A_{\perp}}\right) + (1 - c) \left(\frac{\sigma_n}{R^A_{\perp}}\right)^2 + \left(\frac{\tau_{nt}}{R^A_{\perp\perp}}\right)^2 + \left(\frac{\tau_{nl}}{R^A_{\perp\parallel}}\right)^2 = 1 \text{ for } \sigma_n \geq 0 \quad (87)$$

Where, $c = \left(\frac{R^A_{\perp}}{R^A_{\perp\parallel}}\right) P_{\perp\parallel}^+$. For Mode A failure $\theta_{fp} = 0$. So $\sigma_n = \sigma_{\perp}$; $\tau_{nt} = 0$; $\tau_{nl} = \tau_{\perp\parallel}$

The modified equation is written in Eq.(88)

$$c \left(\frac{\sigma_{\perp}}{R^A_{\perp}}\right) + (1 - c) \left(\frac{\sigma_{\perp}}{R^A_{\perp}}\right)^2 + \left(\frac{\tau_{\perp\parallel}}{R^A_{\perp\parallel}}\right)^2 = 1 \text{ for } \sigma_{\perp} \geq 0 \quad (88)$$

We can see linear and quadratic stress term are present in above equation, so fracture function could be written as Eq.(89)

$$c \left(\frac{\sigma_{\perp}}{R^A_{\perp}}\right) + \sqrt{(1 - c) \left(\frac{\sigma_{\perp}}{R^A_{\perp}}\right)^2 + \left(\frac{\tau_{\perp\parallel}}{R^A_{\perp\parallel}}\right)^2} = 1 \text{ for } \sigma_{\perp} \geq 0 \quad (89)$$

where $R^A_{\perp} = Y_{\perp}$; $R^A_{\perp} = Y_c$ for $\sigma_n \leq 0$; $R^A_{\perp\parallel} = S_{\perp\parallel}$ for $\sigma_{\perp} \geq 0$

Y_{\perp} is the Young's modulus in transverse direction and $S_{\perp\parallel}$ is the shear strength in transverse longitudinal direction. Substituting the 'c' in the above equation, Eq.(90) will be the result. For 60% glass fiber resultant equation is shown in Eq.(91).

$$P_{\perp\parallel}^+ \left(\frac{\sigma_{\perp}}{S_{\perp\parallel}} \right) + \sqrt{\left(1 - \left(\frac{Y_{\perp}}{S_{\perp\parallel}} \right) P_{\perp\parallel}^+ \right) \left(\frac{\sigma_{\perp}}{Y_{\perp}} \right)^2 + \left(\frac{\tau_{\perp\parallel}}{S_{\perp\parallel}} \right)^2} = 1 \text{ for } \sigma_{\perp} \geq 0 \quad (90)$$

For 60% glass fiber $P_{\perp\parallel}^+ = 0.3$

$$0.3 \left(\frac{\sigma_{\perp}}{S_{\perp\parallel}} \right) + \sqrt{\left(1 - 0.3 \left(\frac{Y_{\perp}}{S_{\perp\parallel}} \right) \right) \left(\frac{\sigma_{\perp}}{Y_{\perp}} \right)^2 + \left(\frac{\tau_{\perp\parallel}}{S_{\perp\parallel}} \right)^2} = 1 \text{ for } \sigma_{\perp} \geq 0 \quad (91)$$

Mode B:

This mode of failure occurs purely due to $\tau_{\perp\parallel}$ stressing. A compressive σ_n prohibits fracture. τ_{nt} and τ_{nl} have to overcome an extra fracture resistance, which is proportional to $|\sigma_n|$. Based on the experimental experience, increase in the shear stress caused by a superimposed compressive stress σ_n would grow less than linearly with σ_n . Considering the shear terms, Eq. (86) could be modified as Eq.(92)

$$\left(\frac{\tau_{nt}}{R^A_{\perp\perp} - P_{\perp\perp}^- \sigma_n} \right)^2 + \left(\frac{\tau_{nl}}{R^A_{\perp\parallel} - P_{\perp\parallel}^- \sigma_n} \right)^2 = 1 \text{ for } \sigma_{\perp} \leq 0, |\sigma_{\perp}| \leq |0.4Y_{\perp}| \quad (92)$$

For Mode B failure $\theta_{fp} = 0$. So $\sigma_n = \sigma_{\perp}$; $\tau_{nt} = 0$; $\tau_{nl} = \tau_{\perp\parallel}$. After substituting the value of 'c' and some more modification just to meet experimental data set, Eq. (93) can be written [71].

$$2P_{\perp\parallel}^- \left(\frac{\sigma_{\perp}}{R^A_{\perp\parallel}} \right) + \left(\frac{\tau_{\perp\parallel}}{R^A_{\perp\parallel}} \right)^2 = 1 \text{ for } \sigma_{\perp} \leq 0, |\sigma_{\perp}| \leq |0.4Y_{\perp}| \quad (93)$$

The linear and quadratic stress terms are present in above equation, so fracture function could be written as Eq.(94)

$$P_{\perp\parallel}^- \left(\frac{\sigma_{\perp}}{R^A_{\perp\parallel}} \right) + \sqrt{\left(\frac{\tau_{\perp\parallel}}{R^A_{\perp\parallel}} \right)^2 + \left(\frac{P_{\perp\parallel}^- \sigma_{\perp}}{R^A_{\perp\parallel}} \right)^2} = 1 \text{ for } \sigma_{\perp} \leq 0, |\sigma_{\perp}| \leq |0.4Y_{\perp}| \quad (94)$$

It could be written as in term of know input as Eq.(95)

$$P_{\perp\parallel}^- \left(\frac{\sigma_{\perp}}{S_{\perp\parallel}} \right) + \sqrt{\left(\frac{\tau_{\perp\parallel}}{S_{\perp\parallel}} \right)^2 + \left(\frac{P_{\perp\parallel}^- \sigma_{\perp}}{S_{\perp\parallel}} \right)^2} = 1 \text{ for } \sigma_{\perp} \leq 0, |\sigma_{\perp}| \leq |0.4Y_{\perp}| \quad (95)$$

For 60% glass fiber $P_{\perp\parallel}^- = 0.25$

$$0.25 \left(\frac{\sigma_{\perp}}{S_{\perp\parallel}} \right) + \sqrt{\left(\frac{\tau_{\perp\parallel}}{S_{\perp\parallel}} \right)^2 + \left(\frac{0.25\sigma_{\perp}}{S_{\perp\parallel}} \right)^2} = 1 \text{ for } \sigma_{\perp} \leq 0, |\sigma_{\perp}| \leq |0.4Y_{\perp}| \quad (96)$$

Mode C:

For, $|\sigma_{\perp}| \geq |0.4Y_{\perp}|$ mode fracture plane is no more zero degree. It is important to find the fracture angle to calculate σ_n , τ_{nt} , and τ_{nl} . Fracture envelope looks like circular in this zone. It is more difficult to formulate. The formulation for fracture criterion could be seen below in Eq.(97)

$$\left(\frac{\tau_{nt}}{R^A_{\perp\perp} - P_{\perp\perp}^- \sigma_n} \right)^2 + \left(\frac{\tau_{nl}}{R^A_{\perp\parallel} - P_{\perp\parallel}^- \sigma_n} \right)^2 = 1 \text{ for } \sigma_{\perp} \leq 0, |\sigma_{\perp}| \geq |0.4Y_{\perp}| \quad (97)$$

Solving and arranging above equation to meet experimental results, we can reduce equation to Eq.(98)

$$\left[\left(\frac{\tau_{\perp\parallel}}{2(1 + P_{\perp\perp}^-)R^A_{\perp\parallel}} \right)^2 + \left(\frac{\sigma_{\perp}}{R^-_{\perp}} \right)^2 \right] \frac{R^-_{\perp}}{(-\sigma_{\perp})} = 1 \text{ for } \sigma_{\perp} \leq 0, |\sigma_{\perp}| \geq |0.4Y_{\perp}| \quad (98)$$

Furthermore, above equation could be written in known input as Eq.(99)

$$\left[\left(\frac{\tau_{\perp\parallel}}{2(1 + 0.22)S_{\perp\parallel}} \right)^2 + \left(\frac{\sigma_{\perp}}{Y_{\perp}} \right)^2 \right] \frac{Y_{\perp}}{(-\sigma_{\perp})} = 1 \text{ for } \sigma_{\perp} \leq 0, |\sigma_{\perp}| \geq |0.4Y_{\perp}| \quad (99)$$

C. LaRC failure criteria

C.1. Derivation

Fiber tensile failure

Using a basic principle of the fracture in longitudinal direction, the fiber tensile failure criterion could be written as Eq.(38).

Fiber compressive failure

3D kinking plane is shown in figure given below. Kink plane angle could be found out using Eq.(100)

$$\tan(2\psi) = \frac{2\tau_{23}}{\sigma_2 - \sigma_3} \quad (100)$$

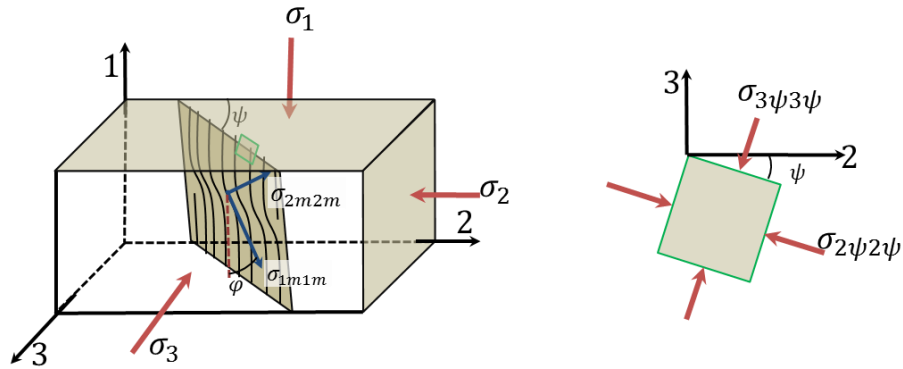


Figure B 2: Schematic diagram of kink plane and associated stresses to this plane

Criterion for the fiber compressive failure is inspired from pucker criteria, which could be written as Eq. (101)

$$\frac{\tau_{1m2m}}{S_1 - \eta_1 \sigma_{2m2m}} \leq 1 \text{ for } \sigma_{2m2m} < 0, \sigma_1 < 0 \quad (101)$$

$$\sigma_{2m2m} = \sigma_1 + \sigma_{2\psi 2\psi} - \sigma_{1m1m} \quad (102)$$

$$\sigma_{2\psi 2\psi} = \frac{\sigma_2 + \sigma_3}{2} + \frac{\sigma_2 - \sigma_3}{2} \cos(2\psi) + \tau_{23} \sin(2\psi) \quad (103)$$

$$\sigma_{1m1m} = \frac{\sigma_1 + \sigma_{2\psi 2\psi}}{2} + \frac{\sigma_1 - \sigma_{2\psi 2\psi}}{2} \cos(2\varphi) + \tau_{1\psi 2\psi} \sin(2\varphi) \quad (104)$$

$$\tau_{1\psi 2\psi} = \tau_{12} \cos(\psi) + \tau_{31} \sin(\psi) \quad (105)$$

$$\tau_{1m2m} = \frac{\sigma_1 - \sigma_2 \psi^2}{2} \sin(2\varphi) + \tau_{1\psi 2\psi} \cos(2\varphi) \quad (106)$$

Criterion for this type of failure can be rewritten for the unidirectional fiber-reinforced composites as Eq.(107)

$$\frac{\tau_{\parallel m \perp m}}{S_{\parallel} - \eta_{\parallel} \sigma_{\perp m \perp m}} \leq 1 \text{ for } \sigma_{2m2m} < 0, \sigma_1 < 0 \quad (107)$$

Matrix tensile failure:

This failure mode occurs when the transverse tensile stress is applied. Generally matrix cracks are expected to initiate from manufacturing defects and can propagate further within planes parallel to the fibre direction and normal to the stacking direction. Energy release rate is nothing but the energy that is released when a crack is formed. Dvorak and Laws [72] determined the components of the energy release rate. The transverse tensile stress is responsible for mode I loading and hence the corresponding energy release rate is denoted by G_I , whereas the in-plane shear and transverse shear stress cause mode II loading. But in this case the failure is mainly by shear hence the energy release rates are combined and it is known as a shear mode G_{SH} . A crack can advance either in longitudinal direction or transverse direction or in both directions. Hahn observed that the fracture strongly depends on the type of loading. He observed that more hackles are observed in the matrix leading to more energy absorption with crack extension.

Mixed mode criteria proposed by Hahn is written in Eq.(108)

$$(1 - g) \sqrt{\frac{G_I}{G_{Ic}}} + g \left(\frac{G_I}{G_{Ic}} \right) + \frac{G_{SH}}{G_{SHc}} = 1 \quad (108)$$

$$g = \frac{G_{Ic}}{G_{SHc}} \quad (109)$$

$$G_I(L) = \frac{G_I(T)}{2} = K_1(\sigma_2)^2 \quad (110)$$

$$G_{Ic}(L) = \frac{G_I(T)}{2} = K_1(Y^T)^2 \quad (111)$$

$$G_{SH}(L) = \frac{G_I(T)}{2} = K_2(\tau_{12})^2 \quad (112)$$

$$G_{SHc}(L) = \frac{G_I(T)}{2} = K_2(S^L)^2 \quad (113)$$

$$(1 - g) \frac{\sigma_{\perp}}{Y_{\perp}} + g \left(\frac{\sigma_{\perp}}{Y_{\perp}} \right)^2 + \left(\frac{\tau_{\parallel\perp}}{S_{\parallel}} \right)^2 \leq 1 \quad (114)$$

Using above equation, we can write failure criterion as

Mixed mode failure:

If $\sigma_{2m2m} > 0$ then even fiber is in compression matrix will fail first. For this condition matrix tensile failure criterion can be used for misalignment plane. So failure criterion can be written as Eq.(115)

$$(1 - g) \frac{\sigma_{\perp m}}{Y_{\perp}} + g \left(\frac{\sigma_{\perp m}}{Y_{\perp}} \right)^2 + \left(\frac{\tau_{\parallel m \perp m}}{S_{\parallel}} \right)^2 \leq 1 \quad (115)$$

Matrix compressive failure:

Similar to buck's failure, matrix compressive failure mode could be written as Eq.(116)

$$\left(\frac{\tau_{nT}}{S^T - \eta_T \sigma_n} \right)^2 + \left(\frac{\tau_{nL}}{S^L - \eta_L \sigma_n} \right)^2 = 1 \text{ for } \sigma_{\perp} \leq 0, |\sigma_{\parallel}| \leq |Y_c| \quad (116)$$

$$\sigma_n = \frac{\sigma_2 + \sigma_3}{2} + \frac{\sigma_2 - \sigma_3}{2} \cos(2\alpha) + \tau_{23} \sin(2\alpha) \quad (117)$$

$$\tau_{nT} = \frac{\sigma_2 - \sigma_3}{2} \sin(2\alpha) + \tau_{23} \cos(2\alpha) \quad (118)$$

$$\tau_{nL} = \tau_{12} \cos(\alpha) + \tau_{31} \sin(\alpha) \quad (119)$$

Matrix failure under biaxial compression:

Under biaxial compression loading matrix fails at some misalignment angle. So above equation can be modified as Eq.(120)

$$\left(\frac{\tau_{nTm}}{S^T - \eta_T \sigma_n^m} \right)^2 + \left(\frac{\tau_{nLm}}{S^L - \eta_L \sigma_n^m} \right)^2 = 1 \text{ for } \sigma_{\perp} \leq 0, |\sigma_{\parallel}| \geq |Y_c| \quad (120)$$

$$\sigma_n^m = \frac{\sigma_{2m2m} + \sigma_{3\psi3\psi}}{2} + \frac{\sigma_{2m2m} - \sigma_{3\psi3\psi}}{2} \cos(2\alpha) + \tau_{2m3\psi} \sin(2\alpha) \quad (121)$$

$$\tau_{nTm} = \frac{\sigma_{2m2m} - \sigma_{3\psi3\psi}}{2} \sin(2\alpha) + \tau_{2m3\psi} \cos(2\alpha) \quad (122)$$

$$\tau_{nLm} = \tau_{1m2m} \cos(\alpha) + \tau_{3\psi1m} \sin(\alpha) \quad (123)$$

D. Grid before and after mesh deformation and re-meshing

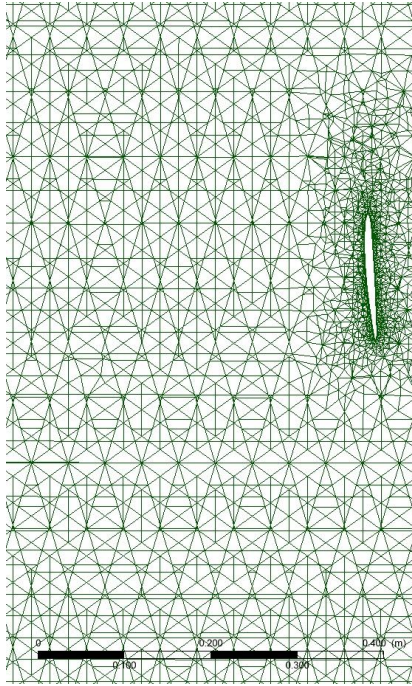


Figure E 1: Mesh topology at $t = 0$ sec @0.9R

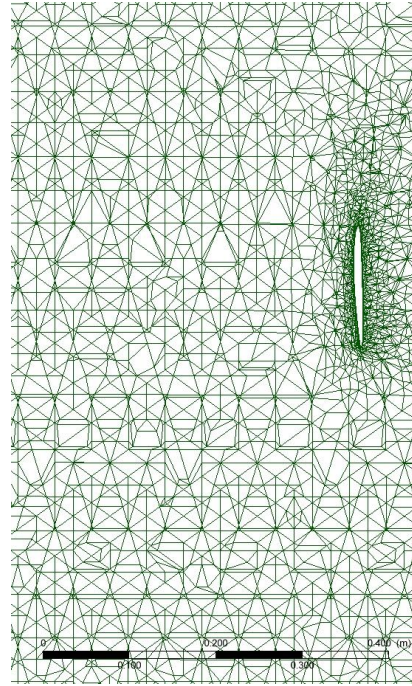


Figure E 2: Mesh topology at $t = 0.02$ sec @0.9R

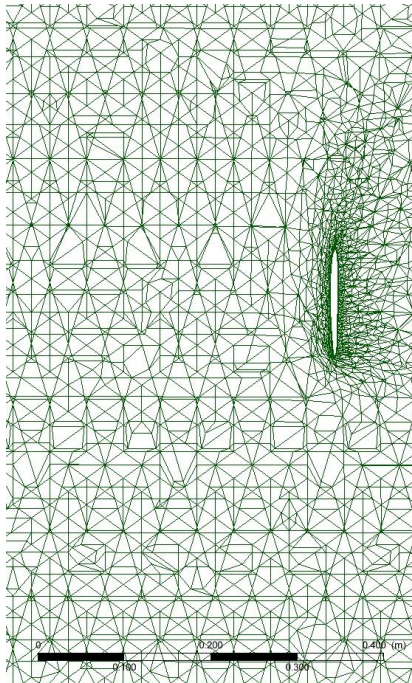


Figure E 3: Mesh topology at $t = 0.05$ sec @0.9R

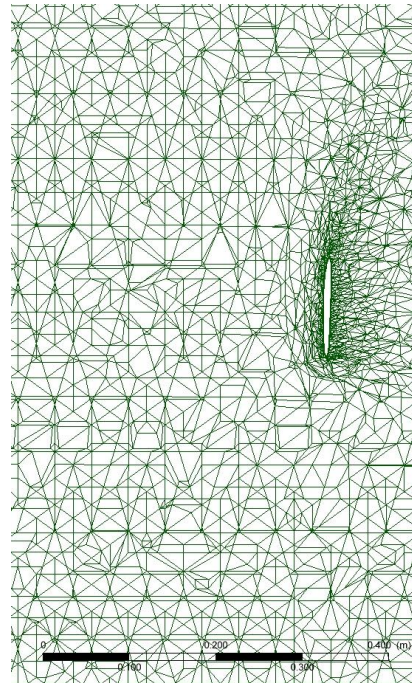


Figure E 4: Mesh topology at $t = 0.08$ sec @0.9R

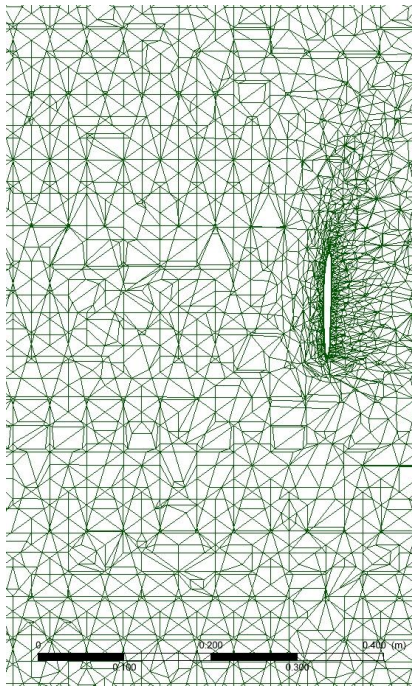


Figure E 5: Mesh topology at $t = 0.11 \text{ sec @}0.9R$

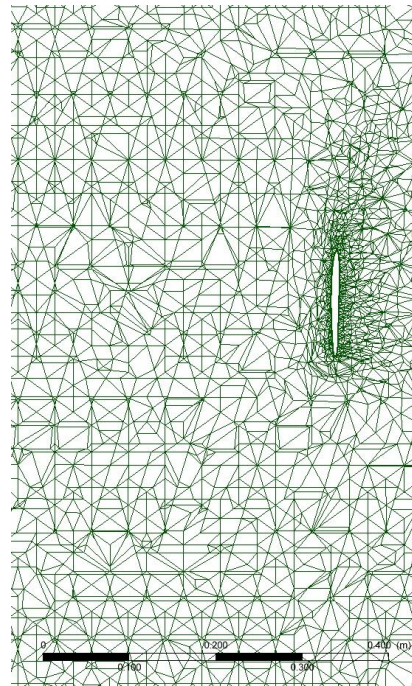


Figure E 6: Mesh topology at $t = 0.14 @0.9R$

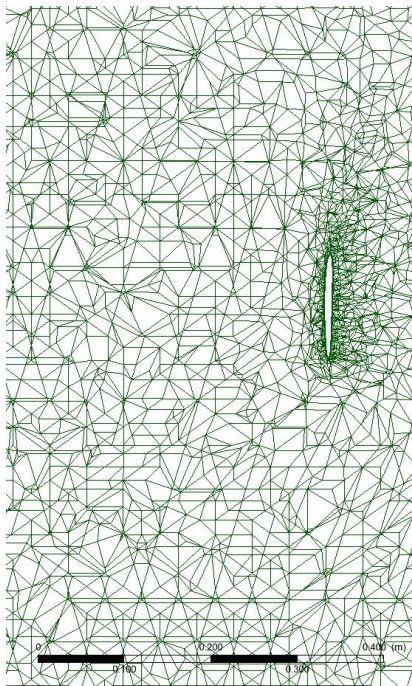


Figure E 7: Mesh topology at $t = 0.20 @0.9R$

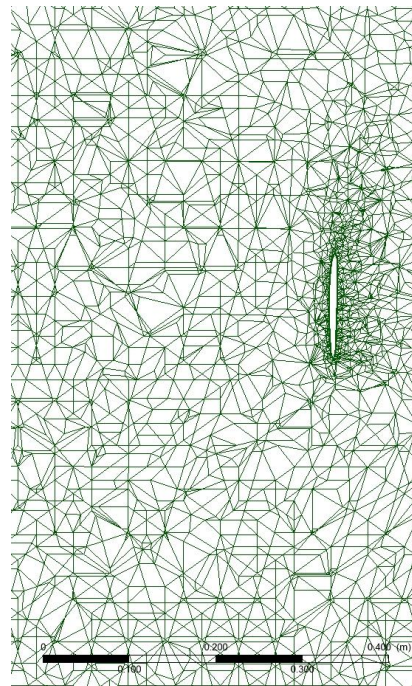


Figure E 8: Mesh topology at $t = 0.26 @0.9R$

Declaration in lieu of oath

I hereby declare that this submission is my own work and that, to the best of my knowledge and belief, it contains no material previously published or written by another person nor material which to a substantial extent has been accepted for the award of any other degree or diploma of the university or other institute of higher learning, except where due acknowledgment has been made in the text.

Rostock, 03, February 2016

Jitendra Kumar